INAUGURAL-DISSERTATION
zur
Erlangung der Doktorwürde

der
Naturwissenschaftlich-Mathematischen
Gesamtfakultät

der
Ruprecht-Karls-Universität
Heidelberg

vorgelegt von
Dipl. Phys. Michael Lange
aus Hanau

Tag der mündlichen Prüfung: 27. Juni 2001

Konkurrenz zwischen Reaktionskanälen bei Elektronenstößen mit dem Wasserstoff-Molekülion HD^+

Gutachter: Prof. Dr. Andreas Wolf
Prof. Dr. Frank Arnold

Dissertation
submitted to the
Combined Faculties for the Natural Sciences and Mathematics
of the Rupertus Carola University of
Heidelberg, Germany
for the degree of
Doctor of Natural Sciences

Competition between Reaction Channels in Electron Collisions of the Hydrogen Molecular Ion HD$^+$

presented by
Diplom-Physicist Michael Lange
born in Hanau

Heidelberg, June 27th, 2001
Referees: Prof. Dr. Andreas Wolf
Prof. Dr. Frank Arnold

Kurzfassung

Konkurrenz zwischen Reaktionskanälen bei Elektronenstößen mit dem Wasserstoff-Molekülion HD^+

Die chemische Zusammensetzung kalter Plasmen wird maßgeblich durch die Chemie und Physik von Molekülionen bestimmt. Von besonderer Bedeutung für ihre Verfügbarkeit in dieser Umgebung sind Stöße mit langsamen Elektronen, die häufig zur Fragmentation der Ionen führen. Die wichtigsten Prozesse dabei sind die dissoziative Rekombination und die dissoziative Anregung der Ionen, welche auch interessante Einblicke in die Dynamik des Elektroneneinfangs und der Dissoziation von Molekülionen versprechen. Daher wurde eine Präzisionsmessung des absoluten, energiedifferentiellen Wirkungsquerschnitts der dissoziativen Rekombination von HD^+-Molekülionen vorgenommen, die am Schwerionenspeicherring TSR des Max-Planck-Instituts für Kernphysik durchgeführt wurde. Dabei konnten bisher unbekannte Strukturen im Wirkungsquerschnitt nachgewiesen werden, die im Zusammenhang mit der Öffnung zusätzlicher Dissoziationskanäle bei steigender Elektronenenergie stehen, und die durch eine veränderliche Wahrscheinlichkeit für einen konkurrierenden Prozeß erklärt wurden. In einem weiteren Experiment wurde erstmalig in einem Speicherring eine Vibrationsanregung der gespeicherten Molekülionen nachgewiesen. Als Ursache wurden Stöße mit langsamen Elektronen aus dem Strahl des Elektronenkühlers oder seltener mit den Molekülen des Restgases im Speicherring festgestellt.

Abstract

Competition between Reaction Channels in Electron Collisions of the Hydrogren Molecular Ion HD^+

The chemical composition of cold plasma is strongly influenced by reactions of molecular ions with other particles. Of special interest are collisions with slow electrons, which often lead to the destruction of molecular ions and thus affect their abundances. The most important reactions in this context are the dissociative recombination and the dissociative excitation of ions, which both are of great interest also to the understanding of electron capture and the dynamics of molecular dissociation. Therefore, the energy-differential cross-section of dissociative recombination of HD^+ molecular ions was measured with high precision and on an absolute scale, at the heavy-ion storage ring TSR located at the Max-Planck-Institut für Kernphysik. A previously unknown structure in the measured cross section was found to be related to the opening of additional dissociation channels with increasing electron energy, which was explained by variations in the strength of a competing mechanism. In another experiment, first evidence was observed for the vibrational excitation of molecular ions stored in a ring. This excitation was attributed to collisions between the ions and slow electrons from the TSR electron cooling device, as well as with molecules from the residual gas in the vacuum system.

Contents

1. Introduction

Most observations of the interstellar medium make use of spectroscopic methods, by measuring the wavelength and width of atomic and molecular lines in emission as well as in absorption. If these lines can be assigned to atomic or molecular species for which the Einstein coefficients are known, the number of particles contained in the field of view can be deduced. Thus, it has been found that free atoms and molecules are not evenly distributed over our galaxy, but are confined to interstellar clouds having a typical size of several parsecs. In addition, it has been discovered that not only neutral particles are present in such clouds, but that also atomic or molecular ions make up a large part of the population. For example, CH^+, CO^+, HCO^+ and H_3O^+ [1] have been identified in observations.

But because of the large timescales involved in the evolution of astronomical objects, these spectroscopic data mainly provides information about the *present* state and composition of such clouds. It does not, however, provide much information about the reactions in which the observed molecules are created or destroyed, or about the influence of external parameters (such as cosmic radiation or light from nearby stars) on the equilibrium number densities of molecular species.

The most prominent among these is the H_2 molecule, which is supposed to account for $\approx 80\%$ of the total number of molecules in clouds (typical number densities being $10^5 - 10^{10}$ m^{-3} [2]), and also (though less abundant) its corresponding positive ion H_2^+. Both of them are important to the synthesis of polyatomic species, which mainly proceeds by collisions between one neutral and one positively charged atom or molecule. Therefore, theoretical models describing the evolution and the chemical composition of molecular clouds need additional input about the different ways of creation or destruction of molecules and molecular ions, mainly in the form of rate coefficients for chemical reactions or for the interaction with other particles. One important mechanism for the removal of positively charged molecular ions is dissociative recombination (DR), where the ion captures a free electron, producing a neutral molecule which quickly (10 fs) dissociates into atoms or smaller molecules. This complex reaction involves a lot of molecular dynamics, which makes it interesting even without the astrophysical background.

For a long time, dissociative recombination has been difficult to investigate experimentally, which was in part due to the very low relative energy between ion and electron (typically some 10^{-2} eV) needed to reproduce the conditions in astrophysical plasma. Another problem in measurements of reaction rates was detecting neutral fragments, which also have very low kinetic energies. This situation has improved greatly since heavy-ion storage rings have first been applied to molecular physics some ten years ago. In a typical storage ring experiment, a fast ($v/c \approx 0.01 - 0.1$) beam of molecular ions is stored for several seconds, while being collinearly merged with an intense electron beam of approximately the same velocity. This opens the opportunity to conduct experiments with vibrationally cold molecular ions, by storing infrared-active species and then waiting long enough to allow excited vibrational states to relax by spontaneous emission of radiation. In addition, the high velocity allows for a simple detection of the dissociation fragments, while the intense electron beam provides high reaction rates, from which the relative change of the DR rate coefficient with electron energy is obtained.

Within this work, this method was applied in an experiment on the DR of the deuterated hydrogen ion HD^+, and extended by also measuring the ion current stored in the ring, which yielded the DR rate coefficent in absolute units. Also, the statistic sample and the energy resolution have been improved greatly, allowing the first precise investigation of the very low rate coefficient at electron energies of $1-4$ eV [3, 4].

However, dissociative recombination is not the only process taking place in collisions between molecular ions and electrons: Aside from elastic scattering, there is also the possibility of the molecular ion being excited by the electron, either electronically, or to a different vibrational level of the initial state. Since these processes may also involve the formation of an intermediate neutral molecule, DR and excitation are competing reactions under most conditions. Therefore, Chapter 2 gives a general introduction to collisions between molecular ions and electrons. Chapter 3 then focuses on the methods and devices needed for the creation and storage of molecular ions, as well as for providing the electron beam. After describing the mentioned DR measurement in Chapter 4, another experiment will be discussed in Chapter 5, which was designed to measure the branching ratios for production of hydrogen fragments in the fine structure states $2s$ and $2p$, in the DR of HD^+. Although this goal could not be achieved, the measurement provided important insights to a process counteracting the radiative relaxation of infrared-active ions in the storage ring, namely the excitation of vibrational states of the ion in collisions with slow electrons, or with molecules from the residual gas in the TSR vaccum system. Only recently, the inverse process of superelastic collisions (SEC), in which the ion is de-excited to a lower vibrational state by the electron, has been discovered [5, 6] and applied in stimulated vibrational relaxation of H_2^+ ions [7]. The obtained results are discussed in detail along with each experiment, and are compiled briefly in Chapter 6, where also some concluding remarks and suggestions for further experiments are made.

2. Reactive Scattering of Molecular Ions and Electrons

For many fundamental theoretical and experimental investigations of the interaction between molecular ions and electrons, HD^+ has the status of a "benchmark ion", which is mainly due to its simple structure, its availability and to the fact that (in contrast to H_2^+) it exhibits a fast radiative cooling of excited vibrational states. Therefore, all measurements presented in this work were carried out on HD^+, also involving the corresponding neutral molecule HD as recombination product. To provide the necessary background for the later discussion of the experimental results, this chapter starts with a brief introduction to the quantum mechanics of a diatomic molecule or ion, especially to the concept of potential energy curves and to radiationless transitions between them. Focusing on the application to HD^+, various scattering mechanisms between molecular ions and electrons will be introduced next, in order of increasing complexity. Because of its importance to the interpretation of experimental data in Chapter 5, an introduction to the photodissociation of molecular ions will also be given before moving on to the description of experimental equipment in the next chapter.

2.1 Molecular States and Potential Energy Curves

For the calculation of many properties of diatomic molecules[1] its potential energy curves have to be known. In the Born-Oppenheimer-Approximation (BO), it is assumed that because of the great difference in mass and velocity, the state of the electrons adjusts immediately to a change of the nuclear position, thus depending on it only as a parameter [8]. Under this assumption, the molecular state can be expressed as the product of an electronic state $|n\rangle$ and a nuclear rovibrational state $|vj\rangle$ [9, 10].

The time-independent Schrödinger equation of the molecule is

$$[\mathbf{T}_{el} + \mathbf{T}_N + \mathbf{V}(r, R)] \, |n\rangle \, |vj\rangle = E_{tot}(n, v, j) \, |n\rangle \, |vj\rangle \,, \tag{2.1}$$

---

[1] all considerations in this chapter are also valid for molecular ions.

where $\mathbf{T}_{el}$ denotes the kinetic energy operator of the electrons and $\mathbf{T}_N = \mathbf{T}_{vib} + \mathbf{T}_{rot}$ the one of nuclear vibration and rotation, while $\mathbf{V}(r, R)$ is the potential energy operator which depends on the electronic and nuclear coordinates r and R. In analogy to the separation of nuclear and electronic motion in the state vector, the total energy eigenvalues are expressed as the sum of electronic, vibrational and rotational energy:

$$E_{tot}(n, v, j) = E_{el}(n) + E_{vib}(v) + E_{rot}(j) \tag{2.2}$$

where each one of n, v and j represents the set of quantum numbers describing these motions. Assuming the effect of $\mathbf{T}_N$ on $|n\rangle$ to be small, the Schrödinger equation (2.1) reduces to an electronic part

$$[\mathbf{T}_{el} + \mathbf{V}(r, R)] \, |n\rangle = V_n(R) \, |n\rangle \tag{2.3}$$

and the eigenvalue problem

$$[\mathbf{T}_{vib} + \mathbf{T}_{rot} + V_n(R) - E_{el}(n)] \, |vj\rangle = [E_{vib}(v) + E_{rot}(j)] \, |vj\rangle \, , \tag{2.4}$$

of the nuclei moving in the Born-Oppenheimer potential energy curve [9]

$$V_n(R) = \langle n| \, \mathbf{T}_{el} + \mathbf{V}(r, R) \, |n\rangle \, . \tag{2.5}$$

In a nuclear continuum state ($E_{tot} > \lim_{R\to\infty} V_n(R)$), the molecule dissociates quickly, and v is replaced by the molecules total energy, which is commonly indicated by the notation $|E_{tot}\rangle$ for such states. Also, the nuclear wavefunction is normalized to the total energy.

For each two electronic states having the same symmetry of the total electronic wavefunction, the Born-Oppenheimer potential energy curves obey the von-Neumann-Wigner noncrossing rule: If two curves come close at some internuclear distance $R = X$, they bend away from each other (instead of actually crossing), and exchange their single-electron configurations and hence their asymptotic behaviour for $R \to \infty$. For example, in Fig. 2.1 the single-electron configuration of the $2^1\Sigma_g^+$ state of HD changes from $1s\sigma_g 2s\sigma_g$ at $R < 3a_0$ to $(2p\sigma_u)^2$ for greater R, because of the avoided crossing with the lowest state of the antibonding Q1 series of HD, which is also of $^1\Sigma_g^+$ type and has a $(2p\sigma_u)^2$ configuration at small R.

Several *avoided crossings* may occur to the same state, sometimes leading to multiple minima in the potential energy curve. In addition, at each of these avoided crossings there is a chance for a radiationless transition to the other state, which is known as a *nonadiabatic* or *Landau-Zener transition* [11, 12, 13].

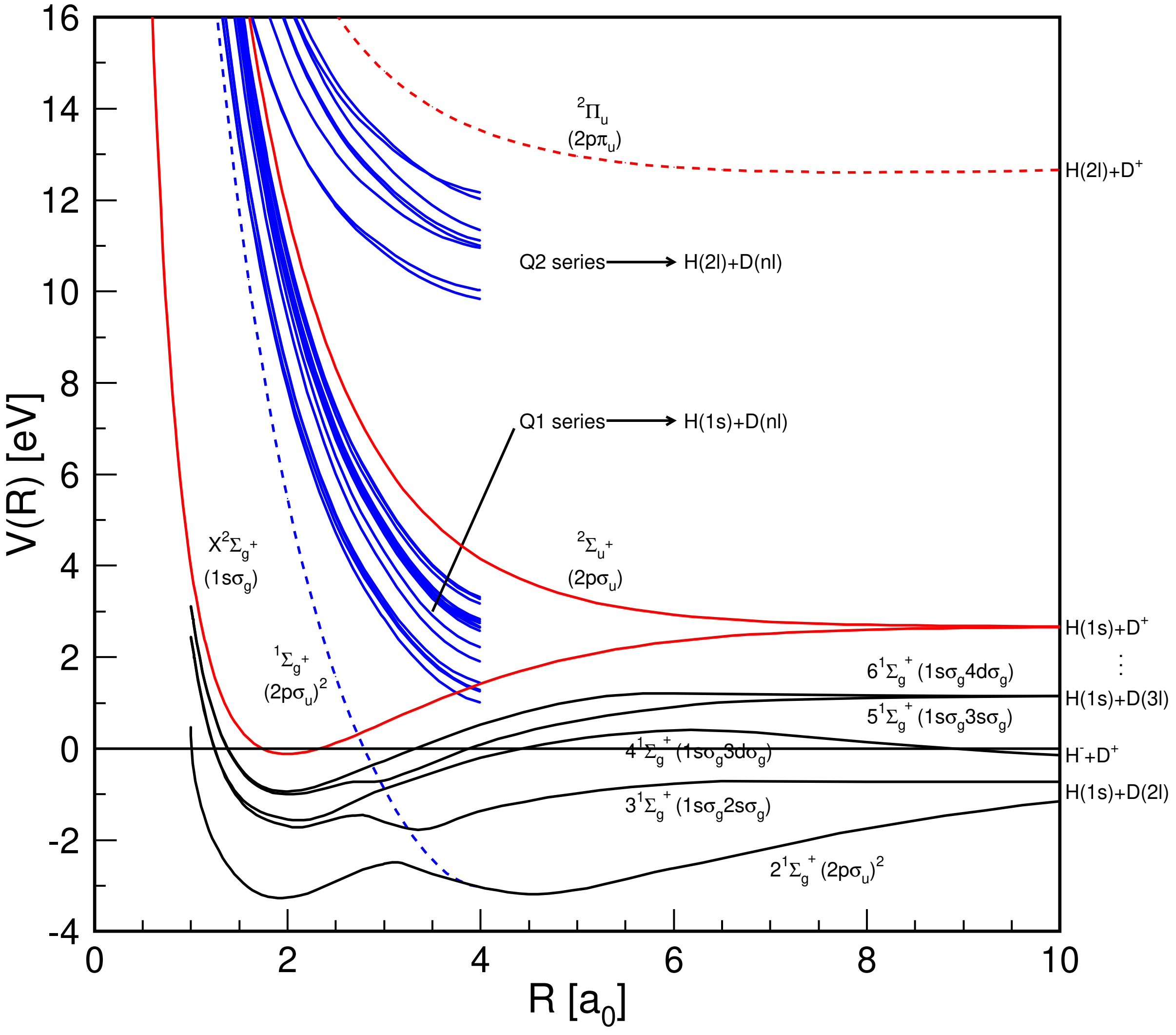

Fig. 2.1: *Potential energy curves of HD$^+$ and HD. Solid red lines: adiabatic curves of the two lowest states of HD$^+$ [18]. Dashed red line: Born-Oppenheimer curve of the second excited state of the ion, calculated for H_2^+ in [19]. Black lines: adiabatic curves of the lowest excited bound states of HD [20], showing avoided crossings with the lowest Q1 curve (dashed blue line), which has been estimated diabatically from [21] and [22]. Solid blue lines: states from the antibonding Q1 and Q2 series, calculated for H_2^+ in [21]. To the right, the atomic states in dissociation limit are noted.*

Although in many cases the pure Born-Oppenheimer approximation is precise enough for calculating the rovibronic structure of molecular spectra as well as molecular dynamics, two modifications are commonly used [9]:

- **The Adiabatic Approximation**:
  In (2.3), it was assumed that $\mathbf{T}_N$ does not act on $|n\rangle$. But since $|n\rangle$ depends on R as a parameter, this approximation is now given up, and by treating $\mathbf{T}_N$ as a small

perturbation the adiabatic potential energy curve is obtained:

$$V_n^{ad}(R) = V_n(R) + \langle n| \mathbf{T}_N |n\rangle \,. \tag{2.6}$$

The contribution from nuclear kinetic energy is usually small, so that the results from the adiabatic approximation are only slightly different from the Born-Oppenheimer ones. Because the adiabatic approximation still takes into account the spin-orbit coupling and the electrostatic interaction between the electrons, the potential curves also follow the von-Neumann-Wigner noncrossing rule.

- **The Diabatic (crossing) Approximation**:
  Here, an additional approximation is made in (2.1) by not only neglecting nuclear kinetic energy, but also the spin-orbit coupling and the electrostatic interaction between the electrons [9]. Where two potential curves in the BO or the adiabatic approximation would exhibit an avoided crossing, the diabatic ones do actually cross. Thus the diabatic states retain their single-electron configuration at all R.

  This approximation is especially useful for treating nonadiabatic transitions between molecular states, by making it easier to determine candidate states for transitions, and to calculate the coupling strength between them.

Nonadiabatic crossings do not necessarily occur between only two states at a time, but often the crossing of three or more states can be separated into several two-by-two crossings [14, 15]. To see how in principle the transition matrix element between two states $|n\rangle$ and $|m\rangle$ is obtained, it is useful to look at the example of the semiclassical scattering between two nuclei, following the argumentation in [14, 15, 16, 17]. The nuclei may move in either one of the corresponding potentials $V_m(R)$ or $V_n(R)$, which in diabatic approximation exhibit a crossing at $R{=}X$. Initially, the system is assumed to be in a linear combination

$$|i\rangle = a_n |n\rangle + a_m |m\rangle = \begin{pmatrix} a_m \\ a_n \end{pmatrix} \tag{2.7}$$

of these states, with the coefficients a_m and a_n. Then the two nuclei approach until reaching the crossing point X. The development of the system's state during this movement is described by a propagation matrix $\mathbf{P}_{X\infty}$, which (by its diagonal elements) may change the phase and amplitude of a_m and a_n separately, but can only have vanishing off-diagonal elements. At the crossing point, the two states get mixed by the off-diagonal elements of the coupling matrix $\mathbf{I}$. Then, the nuclei move on until they reach the inner classical turning point R_1 and start moving back towards X, which is described by the propagating matrix $\mathbf{P}_{XR_1X}$. On the second passage of the crossing point the two states are mixed again, this time by the transposed coupling matrix $\mathbf{I}^T$, and the effects of the following movement towards infinite separation are given by the propagating matrix $\mathbf{P}_{\infty X}$. The coefficients a'_m and a'_n of the final state are thus linked to the initial state by the scattering matrix $\mathbf{S}$:

$$|f\rangle = \begin{pmatrix} a'_m \\ a'_n \end{pmatrix} = \mathbf{P}_{\infty X}\mathbf{I}^T\mathbf{P}_{XR_1X}\mathbf{I}\mathbf{P}_{X\infty}\begin{pmatrix} a_m \\ a_n \end{pmatrix} = \mathbf{S}\begin{pmatrix} a_m \\ a_n \end{pmatrix} \tag{2.8}$$

For sufficiently high kinetic energy of the nuclei, the propagating matrices are easily obtained from the adiabatic potential energy curves by the WKB method, while the calculation of the coupling matrix I is usually done in the diabatic approximation, but under certain conditions may also be done adiabatically [16].

A selection of potential energy curves of HD$^+$ and HD is shown in Fig. 2.1. For the small HD molecule, many of the excited states can be approximated as Rydberg states. This means that one of the electrons is in an ionic core state close to the nuclei, having a wave function similar to HD$^+$, while the other ("Rydberg") electron has a large average distance from this core and is therefore in a state which closely resembles atomic hydrogen. The diabatic potential energy curves of such states, which retain their electronic configuration over the whole range of R, belong to a *Rydberg series*, having a spacing given by the terms of atomic hydrogen and a shape determined by the molecular ion core state. In Fig. 2.1, this can be seen for the Q1 and Q2 series of states, which consist of Rydberg states to the $2p\sigma_u$ and $2p\pi_u$ ionic core, respectively. Only the lowest curve of the Q1 series (the ${}^2\Sigma_u^+(2p\sigma_u)^2$ state) deviates strongly from this scheme, because both electrons have the same configuration, so that the assumption of a large average separation between them is not fulfilled. The bound states of HD also belong to a Rydberg series ($1s\sigma_g$ core), but because of coupling and exchange of configuration with the mentioned Q1 state, their adiabatic potential curves have rather different shapes, especially for low principal quantum numbers of the Rydberg electron.

2.2 Electron-Ion Collisions

In the following, a compilation of cross sections and reaction mechanisms for a variety of scattering processes between electrons and molecular ions is given, excluding the fully elastic channel. All considerations in this chapter assume that initially the molecular ion and the electron are at an infinite distance, and that the ion is in a vibrational level (quantum number v and wavefunction $\zeta_v(R)$) of its electronic ground state $|n\rangle$, while the electron has the kinetic energy E. As the electron moves towards the ion, a Franck-Condon transition to another state $|n^*\rangle$ takes place (at the nuclear coordinate R_{trans}), which can be either an excited ionic or a neutral state, depending on whether the electron is captured or remains free.

Molecular rotation, as well as the angular momentum of the electron is completely neglected in the discussion, and the presented models were chosen for simplicity rather than for precision. All energies are measured from the ionic ground state ($v=0$), by setting $E_{el}(n) + E_{vib}(0)=0$, so that the total energy in (2.2) is always $E_{tot}=E + E_{vib}(v)$. The equations in this chapter are denoted in the MKSA system except for the energy, for which the electron volt (eV) is used as a convenient unit.

2.2.1 Dissociative Excitation

Dissociative excitation (DE) is a scattering process in which a molecular ion is excited by a passing electron into a repulsive state with quantum number n^*, which subsequently dissociates into one neutral and one charged atomic fragment[2]:

$$AB_v^+ + e \longrightarrow AB^{*+} + e \longrightarrow A^+ + B + e \tag{2.9}$$

Although this process follows the Franck-Condon principle, it is not restricted to a single value of R_{trans} (Fig. 2.2): Because the electron may retain some of its kinetic energy after the scattering, the transition may occur at any internuclear separation at which E exceeds the excitation energy $E_{trans} = V_*(R_{trans}) - E_{vib}(v)$ to the upper state. Depending on the asymptotic behaviour of this state for $R \to \infty$, each of the atomic fragments may again carry away a fraction of E_{trans} in form of internal excitation, the rest is transferred into kinetic energy of the fragments.

For HD$^+$ and at the electron energies used in the experiments, the dissociating state may be either $2p\sigma_u$ or $2p\pi_u$. The Franck-Condon principle predicts a vanishing DE cross section σ_{DE} for E much smaller than the energy difference between the $2p\sigma_u$ and the ground state, at the outer classical turning point R_{c2} (which is $\approx$8.9 eV for $v=0$). Due to the tails of the initial nuclear wave function $\zeta(R)$ in the nonclassical regions, the cross section shows a slow onset at this Franck-Condon threshold, and then exhibits a structure corresponding very roughly (because of the degree of freedom in R_{trans}) to the nodes of the nuclear wave function and, at still higher energies, to the onset of DE via the energetically higher $2p\pi_u$ state [23], with an overall drop [24] towards increasing E.

However, even far below the Franck-Condon threshold, a DE rate is observed in experiments, since there is another mechanism which contributes to this process: the capture of the electron by the ion, in which a neutral excited molecule is formed, which can subsequently autoionize and dissociate [23, 25, 26]:

$$AB_v^+ + e \longrightarrow AB^{**} \longrightarrow AB^{*+} + e \longrightarrow A^+ + B + e \tag{2.10}$$

---

[2] All reaction schemes remain true if the atomic fragments A and B are swapped

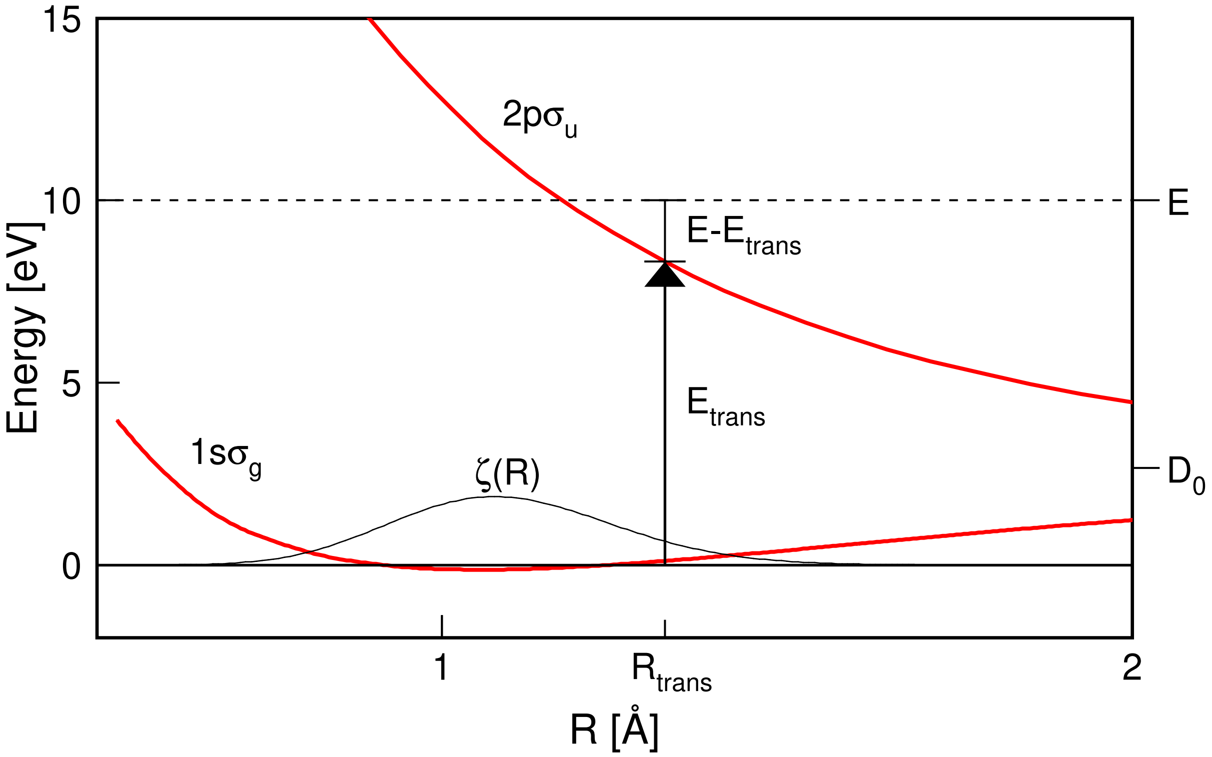

Fig. 2.2: *Direct dissociative excitation of ground-state* $HD^+_{v=0}$ *at* $E \approx 10$ *eV: The ion is excited to the antibonding* $2p\sigma_u$ *state (at the internuclear separation* R_{trans}*) by a passing electron and dissociates into two atomic fragments of kinetic energy* E_{trans}*, leaving the electron with* $E - E_{trans}$*. Red lines: potential energy curves; dashed black line: initial electron energy* E*. Also shown is the nuclear wavefunction* $\zeta(R)$ *for* $v=0$ *(solid black line).*

This capture mechanism is very efficient, because the kinetic energy of the incoming electron is transferred into internal excitation of the ion, thus requiring only interaction between electrons and not with the nuclei. Similar to dielectronic recombination of atomic ions, the molecule is thereby produced in a doubly-excited state ($(2p\sigma_u)^2$ for HD$^+$). This state has a much stronger Franck-Condon overlap with the ionic ground state for low excitation energies E_{trans}, so that the reaction is possible as soon as E exceeds the dissociation energy $D_0 = 2.6677$ eV [27] of HD$^+$. The cross section for this indirect DE process can approximately be written as the product of a capture cross section $\sigma_{cap,v}(E)$ from the vibrational level v into the intermediate neutral state, and its probability P_{AD} to autoionize and dissociate thereafter [28, 29]:

$$\sigma^{indirect}_{DE,v}(E) = \sigma_{cap,v}(E) \cdot P_{AD}(E) \tag{2.11}$$

with the capture cross section

$$\sigma_{cap,v}(E) = \frac{\pi^2\hbar^2}{2m_eE}\left(\frac{g_*}{g_v}\right)\Gamma_{cap} \cdot |\zeta_v(R_{trans})|^2 \cdot \left|\frac{dV_*}{dR}\right|^{-1}_{R_{trans}} \tag{2.12}$$

which depends on the capture width $\Gamma_{cap}(R_{trans})$, the probability of the initial ion having an internuclear separation of R_{trans} (given by the square of its nuclear wave function $\zeta(R_{trans})$ at this point), and also on the slope of the final potential energy curve.
Exact calculations of $\sigma_{DE,v}^{indirect}$ in this low energy regime have only been carried out recently [31], yielding reasonable agreement with experimental data, while there are several earlier works covering energies above 10 eV [24, 32, 33, 34].

2.2.2 Vibrationally Superelastic and Inelastic Collisions

These two mechanisms (SEC or IC, respectively) are related to DE. The important difference is that after electron collision, the ion does not dissociate but is left in a different vibrational state with a quantum number $v' < v$ for SEC and $v' > v$ for IC. SEC has only recently been discovered experimentally, in storage ring experiments on the dissociative recombination of H_2^+ [5, 6, 7]. IC has been known for a longer time, but evidence of its role as a vibrational heating process in storage rings was detected in the measurement described in Chapter 5. The reaction scheme for the SEC and IC processes is

$$AB_v^+ + e \longrightarrow AB_{v'}^+ + e \tag{2.13}$$

This desires a direct vibrational excitation or de-excitation where the electron leaves immediately. But because the Franck-Condon overlap between two vibrational states of the same n is usually small, and the measured SEC rate coefficients were much higher than calculations for this direct mechanism [35], it is suspected [7] that both collision types may also propagate by an indirect process similar to the capture mechanism already discussed with respect to DE, again involving the same intermediate neutral state:

$$AB_v^+ + e \longrightarrow AB^* \longrightarrow AB_{v'}^+ + e \tag{2.14}$$

This is called the indirect SEC or IC mechanism. Accordingly, it is possible to write the cross section for indirect SEC or IC in a similar fashion as for the DE case

$$\sigma_{vv'}^{indirect}(E) = \sigma_{cap,v}(E) \cdot P_A(E, v') \tag{2.15}$$

with the capture cross section (2.12), and with the probability $P_A(v')$ for autoionization to the initial electronic state, but to a different vibrational quantum number v' and without dissociation.

2.2.3 Dissociative Recombination

In the indirect mechanism for dissociative excitation and also in SEC/IC, the intermediate neutral state is doubly-excited (and usually of antibonding type). In consequence, dissociation into atomic fragments is an important competition to autoionization, i.e. to the indirect channels of DE, SEC and IC. At low energies, where autoionization is energetically forbidden, dissociation is the only efficient way for the molecule to stabilize, since the transition to a lower state by emission of a photon is by far slower (the typical dissociative lifetime being of the order of $10 - 100$ fs, compared to several ns for light emission).

This combination of electron capture and dissociation into atomic (for polyatomic ions also smaller molecular) fragments is called dissociative recombination (DR). It was first discovered in [39], and is probably both the most complex (and meanwhile also the best studied) collision process between molecular ions and electrons, which is mainly due to the many different reaction mechanisms and channels which may contribute or compete in the reaction, even for small molecular ions like HD^+.

There are two basic modes of dissociative recombination, the so-called "crossing mode" and the "tunneling mode", which reflect how the electron capture proceeds. The tunneling mode was predicted by Guberman [36], and a short time ago also discovered experimentally for HeH^+ [37] and LiH^+ [38], but it is not discussed in detail since it is of no importance to HD^+. In the other mode, the potential curve of the capture state at some R exhibits a crossing with the initial ionic state (see Fig. 2.1). This means that from the classically allowed region ($R_{c1} < R < R_{c2}$) of the initial state, a vertical transition to the capture state is possible. Depending on whether the capture state is of the bonding or antibonding type, two mechanisms are distinguished which (in a somewhat different sense as regarding DE, SEC and IC) are called direct and indirect DR.

Direct DR

In direct dissociative recombination, an electron of energy E is captured by the molecular ion in the vibrational state v into an antibonding state of the neutral molecule, which then dissociates into (possibly excited) atomic fragments with quantum numbers nl and $n'l'$:

$$AB_v^+ + e \longrightarrow AB^* \longrightarrow A(nl) + B(n'l') \tag{2.16}$$

In contrast to the direct DE, SEC and IC, the electron is absorbed and cannot carry away excess energy. Hence, in good approximation, a transition can only occur at an internuclear distance R_{trans} where the condition

$$V_{n^*}(R_{trans}) - V_n(R_{trans}) = E + E_{vib}(v) \tag{2.17}$$

is fulfilled. The transition between ionic and neutral state is thus restrained to a single value of R_{trans} for any given set of E and v, which yields a capture cross section according to (2.12), and the cross section for direct DR via a given capture state can be expressed in the product form [28, 29]:

$$\sigma_{DR,v}^{direct}(E) = \sigma_{cap,v}(E) \cdot P_D(E) \tag{2.18}$$

where $\sigma_{cap,v}$ is the capture cross section (2.12) and $P_D(E)$ is the probability of the capture state to dissociate without autoionizing, which is often called the survival factor. In [30], this probability was estimated by assuming a classical trajectory $R(t)$ for the dissociating nuclei, as well as a local autoionization width $\Gamma(R)$, such that $\Gamma(R)/\hbar$ is the autoionization probability per unit time at an internuclear separation R:

$$P_D(E) = \exp\left(-\int \frac{\Gamma(R(t))}{\hbar} dt\right) \tag{2.19}$$

Expression (2.19) is valid only for low energies, where the autoionization can only lead to the vibrational ground state of the ion, because the integral is usually evaluated between $t=0$ (capture) to the time when the internuclear separaration reaches the *stabilization point* R_s, at which the potential energy curve of the capture state goes below the one of the ionic state, making further autoionization impossible [30].

With the definitions from (2.11) and (2.15), it is obvious that for any E the relation

$$P_D(E) + P_{AD}(E) + \sum_{v'} P_A(E, v') = 1 \tag{2.20}$$

must be satisfied.

Although this simple model is helpful for a general understanding the of DR, it is not well suited for precise calculations of the cross section. For this purpose, several more precise methods have been developed, for example the Multichannel Quantum Defect Theory (MQDT [40]), which allows a consistent treatment of the effects from the indirect DR mechanism, which involves many rovibrational levels of bound molecular states and is described in more detail in Chapter 4.4.

The following dissociation step is dominated by the interaction between many states of the neutral molecule only. For example, in the DR of HD^+, at electron energies up to a few eV (and only such are of interest here) the electron is mainly captured into the doubly excited $(2p\sigma_u)^2$ state. During dissociation, the diabatic potential curve crosses the bound Rydberg series to the $1s\sigma_g$ core, of which many states are of ${}^1\Sigma_g^+$ type, thus having the same symmetry as the capture state (Fig. 2.1). As described in Chapter 2.1, at each of these crossings a radiationless transition between the involved states is possible, so that the dissociation will propagate through a manifold of channels. In an ensemble of DR reactions, this leads to the population of fragment states of the type $\mathrm{H}(1s)+\mathrm{D}(nl)$ or $\mathrm{H}(nl)+\mathrm{D}(1s)$, with branching ratios b_n and $n \geq 2$. For $\mathrm{HD}^+_{v=0}$, these have been experimentally observed [22] as a function of electron energy, by measuring the relative velocity of the fragments (and thus the kinetic energy release of the reaction) with a three-dimensional imaging technique [41]. It was found that all final states are populated almost evenly, as soon as they become energetically accessible (Fig. 2.3). This behaviour has been well reproduced by a semiclassical multistate curve crossing (MSCC) calculation [22, 42], which modelled the redistribution of probability flux from the $(2p\sigma_u)^2$ capture state to the states of the Rydberg series during dissociation. At each avoided crossing, a matrix I like in (2.8) was established based on the Landau-Zener probability [43] for a transition between the potential curves $V_i(R)$ and $V_j(R)$

$$p_{ij} = \exp\left(-\frac{2\pi V_{ij}^2}{\left(\frac{\partial V_j}{\partial R} - \frac{\partial V_i}{\partial R}\right) v_X}\right) \tag{2.21}$$

where V_{ij} denotes the coupling matrix element between these states, and v_X is the velocity of the nuclei at the crossing point $R = X$. Phase shifts to the nuclear wavefunction were neglected in this calculation, as was the reflection of probability flux at the avoided crossings or by the potential walls of closed reaction channels (states with a dissociation limit higher than E_{tot}). Although this simple model works remarkably well for explaining the branching ratios, the experiment discussed in Chapter 4 revealed that the reflection of probability flux by closed reaction channels also influences the total cross section for dissociative recombination. This required some adjustments to the MSCC model of the dissociation step, which are discussed along with the experimental evidence in Chapter 4.4 and in [3].

Also the phase of the nuclear wave function at an avoided crossing with another state can be of importance: For example, this is the case for the two lowest potential curves of ${}^1\Sigma_g^+$ type shown in Fig. 2.1, which are both connected to the $n = 2$ final state of HD in the dissociation limit. The $2s$ and $2p$ sublevels of this final state are populated with different amplitudes, depending on which molecular curve the dissociation proceeds by [42, 44]. These curves exhibit two crossings, at $R \approx 3$ $\mathrm{a_0}$, and again around $R \approx 13$ $\mathrm{a_0}$. Hence, during the dissociation process, both states are populated coherently at the first crossing, then acquire different phase shifts in the intermediate region (depending on the state by which the dissociation propagates), and are coherently superpositioned at the second crossing. Interference is therefore expected between the amplitudes of dissociation into the $2s$ and the $2p$ final state. This is visible in Fig. 2.4, which shows the calculated population ratio b_{2s}/b_{2p} to be oscillating with increasing electron energy, at a period of about 1 eV [42].

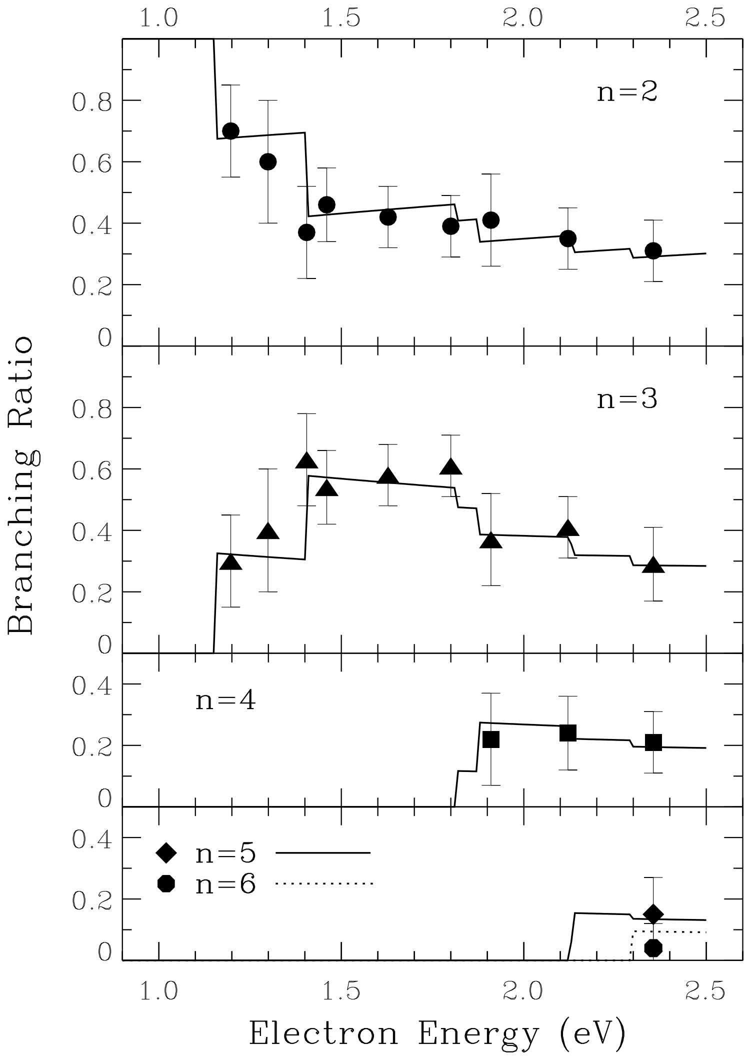

Fig. 2.3: *Comparison between measured (symbols with error bars) and calculated (solid lines) branching ratios for the final states of the DR of* $HD^+_{v=0}$. *Both measurement and theory distinguished between the primary quantum numbers* $n = 2 - 6$ *of the final states* $H(1s) + D(nl)$ *or* $H(nl) + D(1s)$.

Indirect DR

Another type of interference may arise in the total DR cross section, from the coherent superposition of the direct DR amplitude with that of a second process denoted indirect DR, which is of great importance to the DR of HD^+ at low energy. In the indirect reaction, the capture of the electron does not involve the excitation of an inner electron of the ion. Instead, its kinetic energy is transferred into nuclear excitation, so that the neutral molecule is produced in a vibrational level v' of a singly excited bound state, and is then predissociated by an antibonding

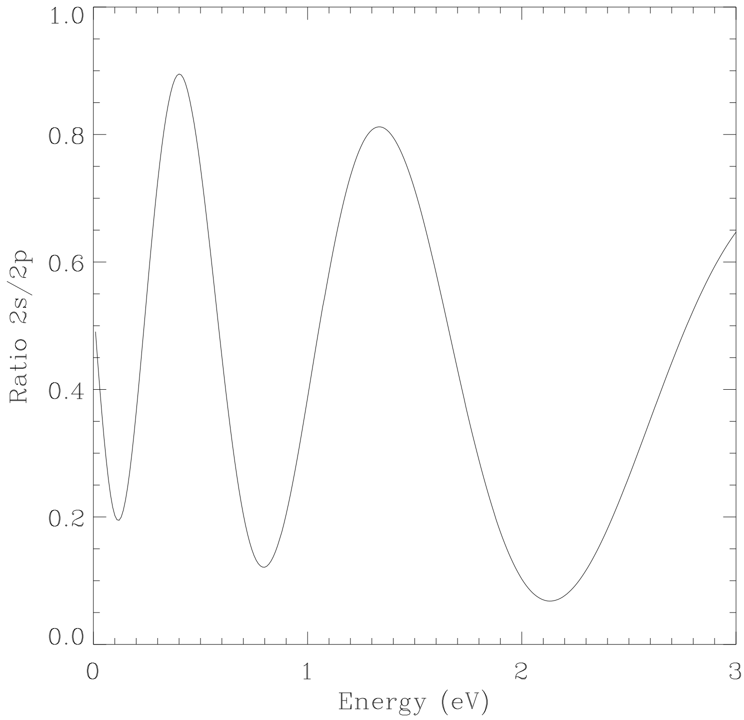

Fig. 2.4: *Interference in the relative population of the $2s$ and $2p$ fragment states of HD.*

state (which for HD is identical to the capture state of the direct mechanism):

$$AB_v^+ + e \longrightarrow AB_{v'} \longrightarrow AB^* \longrightarrow A(nl) + B(n'l') \tag{2.22}$$

The cross section for this process (disregarding the interference with the direct DR, and also interference between neighboring capture states) would be [28, 29]:

$$\sigma_{DR,v}^{indirect}(E) = \sum_{v'} \frac{\pi\hbar^2}{4m_eE} \left(\frac{g_{v'}}{g_v}\right) \frac{\Gamma_{A,v'}\Gamma_{D,v'}}{(E + E_v - E_{v'})^2 + \frac{1}{4}\Gamma_{v'}^2} \tag{2.23}$$

For a sufficiently long-lived capture state, the total decay width $\Gamma_{v'}$ of the vibrational level v' is the sum of the widths for decay by autoionization and by dissociation:

$$\Gamma_{v'} = \Gamma_{A,v'} + \Gamma_{D,v'} \tag{2.24}$$

Expression (2.23) is of course only an approximation, because it does not include interactions between molecular states which may take place after the predissociation, and is only valid for capture states which do not interfere with each other. For a manifold of capture states, e.g. the

$1s\sigma_g$ Rydberg series in the case of HD, interference between different capture states leading to the same final state has to be considered also, as well as interference with the direct channel. In particular, the interference between direct and indirect DR leads to the so-called window resonances, which for HD show up mainly as narrow dips in the total cross section, which is otherwise dominated by the direct mechanism. In this context, the rotational sublevels of the molecule also cannot be ignored any more, since they lead to similar structures in the cross section [45]. Much effort has been directed towards predicting the total DR cross section at low energies, which is strongly influenced by the interference between the direct and the indirect DR mechanism. An example of such a calculation is shown in Fig. 4.8.

2.3 Photodissociation

For molecules, as well as for molecular ions, there is also a dissociating process induced by the interaction with (UV-) light. By absorption of a single photon of energy E_γ, a molecule or ion is excited from the initial state $|n\rangle\,|v\rangle$ to a continuum state $|n^*\rangle\,|E_{tot}\rangle$. In contrast to direct DR, this dissociating state is only singly excited in most cases. There also exsits an indirect mechanism which proceeds by an electronically excited bonding state, but for the photodissociation of HD$^+$, only the direct one is of importance:

$$AB_v^+ + \gamma \longrightarrow AB^{+*} \longrightarrow A(nl) + B(n'l') + E_{kin} \tag{2.25}$$

The cross section for photodissociation is obtained in semiclassical approximation from the initial nuclear wavefunction ζ_v, the potential energy curve V_* of the excited state (its slope being important for the Franck-Condon projection of the initial wavefunction) and the transition radius R_{trans} [46]:

$$\sigma_{PD,v}(E_\gamma) = \frac{\pi E_\gamma}{3\hbar}\sqrt{\frac{\mu_0}{\epsilon_0}}\left(\frac{d}{g_v}\right)\mu_{el}^2(R_{trans})\cdot|\zeta_v(R_{trans})|^2\cdot\left|\frac{dV_*}{dR}\right|_{R_{trans}}^{-1} \tag{2.26}$$

where g_v is the statistical weight of the lower state and $d=1$ for transitions between two Σ states and $d=2$ otherwise. The analogy to the electron capture cross section (2.12) is close, the main difference being the phase space factor which is now proportional to the energy of the incident particle, while the dipole matrix element for the transition between the two electronic states [10]

$$\mu_{el}(R) = e\,\langle n^*|\sum_i Z_i R_i - \sum_j r_j\,|n\rangle \tag{2.27}$$

takes the role of the capture width. The survival factor, which played an important role in DR is not needed here, because the excited state cannot autoionize, as no previous electron capture is involved. Since the probability for radiative stabilization during the very fast dissociation step is very small, the total photodissociation cross section is directly given by the absorption cross section.

In the experiment described in Chapter 5.2, photons of the constant energy $E_\gamma \approx 3.63$ eV were used to photodissociate HD$^+$ ions from various vibrational levels of the electronic ground state, over the $2p\sigma_u$ excited state. Threfore, calculations were done for σ_{PD} at a fixed energy but as a function of v, by applying eq. (2.26) to the tabulated potential energy curves and transition dipole moments from [18], along with vibrational wave functions obtained from [47]. The results are displayed in Fig. 2.5 for $v = 0 - 19$, which shows that the photodissociation cross section of HD$^+$ for $v > 4$ varies by approximately two orders of magnitude (at an average of $\bar{\sigma} = 9 \cdot 10^{-19}$ cm^2). The strong dips at $v = 7$ and $v = 10$ are due to the Franck-Condon transition taking place at nodes of the initial nuclear wavefunction, thus the value of $\sigma_{PD,v}$ is very sensitive to the exact photon energy.

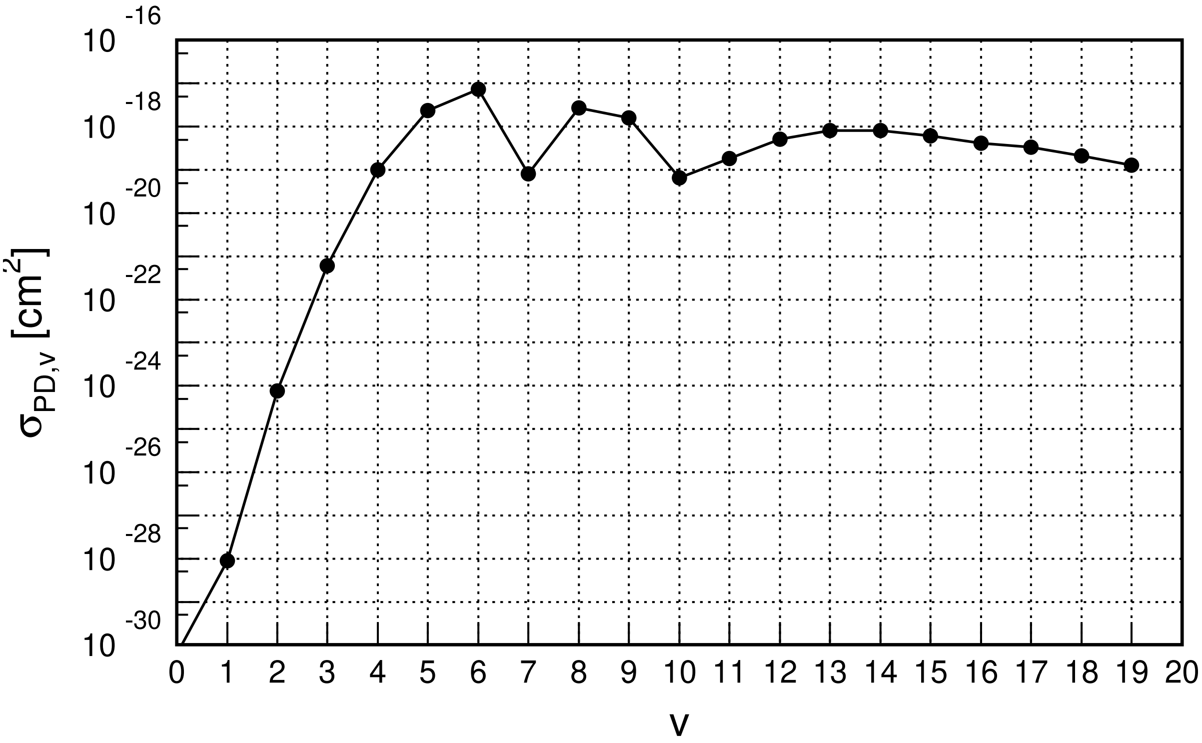

Fig. 2.5: *Photodissociation cross section σ_{PD} of HD$^+$ for the channel $1s\sigma_g \rightarrow 2p\sigma_u$, for vibrational quantum numbers $v = 0 - 19$ and at the fixed photon energy of $E_\gamma = 3.63$ eV.*

3. The MPI Heavy-Ion Storage Facility

We have seen that molecular structure and dynamics often depend strongly on the nuclear wavefunction, especially on its vibrational part. In contemporary experiments on molecular physics, a lot of effort is therefore being put into control or at least in measuring the initial state of the molecule being investigated. For infrared-active molecular ions, a common way to exert control over the initial state is to capture them in a trap, and to store them long enough to allow relaxation of the excited states by spontaneous emission of radiation. This can be well achieved by using RF multipole traps, which allow the examination of molecular ions in their rest frame.

But for certain experiments, like for the study of interactions between molecular ions and electrons, one also has to provide the electrons. This is most often done by generating an electron cloud in front of a heated cathode, which is at a potential difference against a grounded anode. The electrons are accelerated and directed at the resting molecules, but there are three problems arising with this method: first, the accelerating potential has to be high enough to extract a significant current from the cloud (in space-charge limited emission, $I \propto U^{3/2}$). This means that measurements at zero electron energy are not possible, but only from eU upwards. Last, the kinetic energy distribution of the electrons is given by the temperature of the cathode (modified by the acceleration process, see below), which limits the energy resolution of the experiment. To overcome these limitations, such measurements are often done using heavy-ion storage rings, where ions and electrons can be made to move parallel at great velocity, while still having a vanishing *relative* velocity. Also, at storage rings there often is an electron cooler device, which aside from phase-space cooling of the stored ion beam can also be used as an electron target of adjustable energy and high resolution, along with a high electron density.

The TSR at the Max-Planck-Institut für Kernphysik in Heidelberg is one of the three storage rings worldwide which are suited for molecular physics, the others being ASTRID in Aarhus, Denmark, and CRYRING in Stockholm, Sweden (TARN II in Tokyo being recently shut down). In the following chapter, the relevant experimental equipment at the TSR will be explained, including a short introduction to electron cooling.

3.1 Ion Sources and Accelerators

Prior to storage in the TSR, molecular ions have to be produced and accelerated. At the heavy-ion accelerator and storage facility of the Max-Planck-Institut für Kernphysik, there are three independent accelerators available for producing fast beams of positively charged ions: A single-ended Van-De-Graaff accelerator (ISSI) with an acceleration voltage of up to 2 MV, with a Penning ion source to create positively charged ions, and a Tandem Van-de-Graaf, fed by a cesium sputter source or a duoplasmatron source for producing negative molecular ions, which are stripped into positive ones during acceleration, thus using the acceleration voltage of up to 12 MV twice. Recently, these have been supplemented by the high current injector HSI [48, 49, 50], a combination of two radio-frequency quadrupole accelerators (RFQs) and two optional 7-gap RF-resonators, having a maximum output energy of 2.5 MeV per elementary charge, for positive ions produced in a CHORDIS source. There is also a Linac-postaccelerator for further increasing the ion beam energy with up to 10 RF-resonators. Table 3.1 gives an overview of the ion sources, accelerators and ion energies which have been used.

In the ionization of molecules in the source, either by electron or atom impact, many of the rovibronic states of the ion are excited. As was shown in [51], for HD^+ the measured population of vibrational states can approximately be reproduced by applying the Franck-Condon principle to the ionization process in a penning source, which uses electron impact ionization.

3.2 The Test Storage Ring (TSR)

The TSR (Fig. 3.1) is made up of eight 45° deflection dipole magnets, which keep the stored ions in an evacuated peam-pipe ($5 \cdot 10^{-11}$ Torr), on a closed orbit of nearly octagonal geometry with a circumference of 55.40 ± 0.05 m. Five quadrupole and three sextupole magnets make up each one of the four groups (or periods) necessary for strong focusing of the stored ion beam.

Measurement	Ion Source	Accelerator	Post-Acc.	$E^{\dagger}_{ion}$/MeV
DR & DE of HD^+	Penning	ISSI	-	2.014
	Penning	ISSI	-	2.024
IC of HD^+	CHORDIS	HSI	+	15.876

Tab. 3.1: *Compilation of the used ion sources, accelerators and ion energies. †: deduced from the electron cooling parameters (table 3.2).*

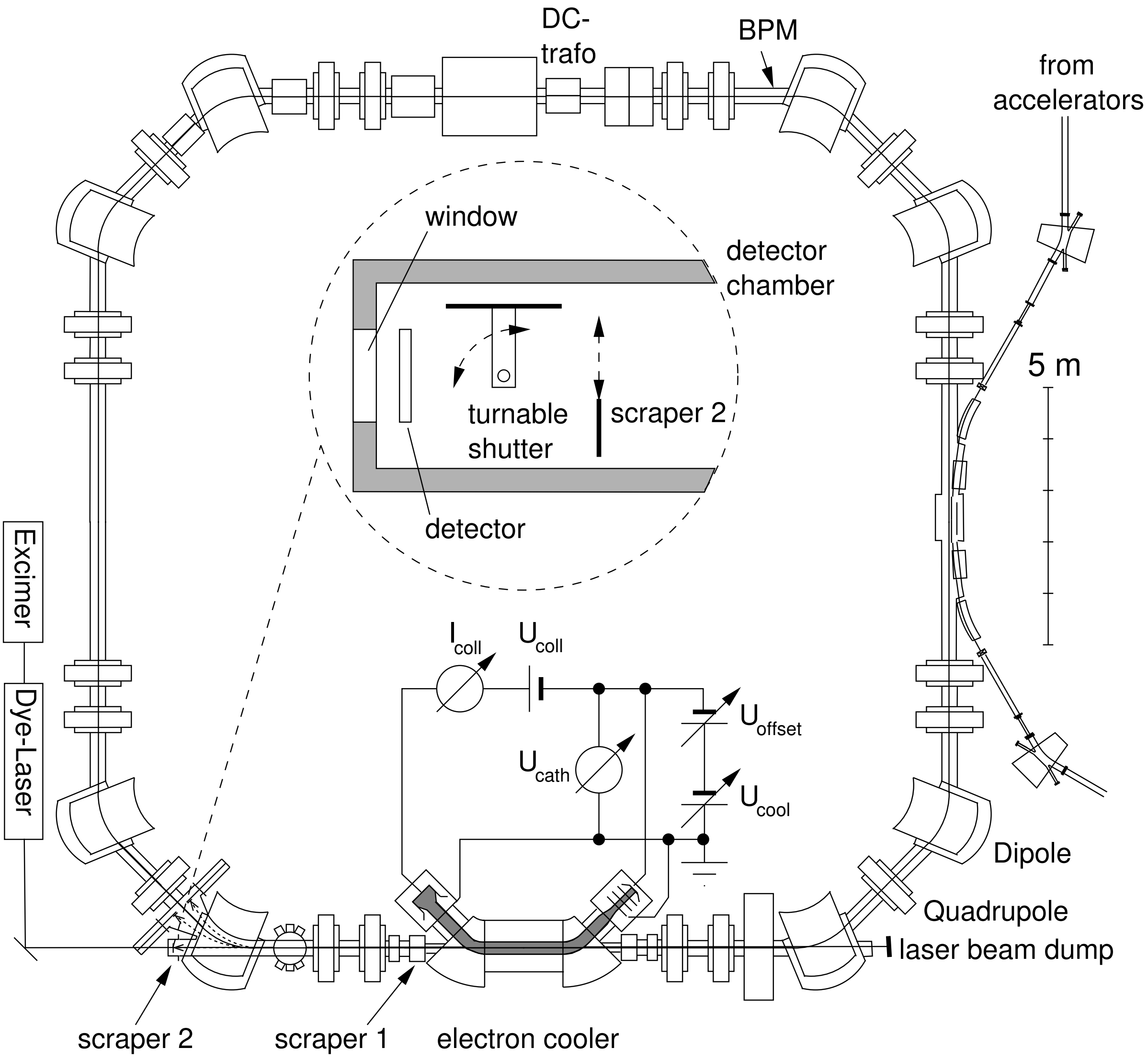

Fig. 3.1: *TSR with electron cooler and detector chamber (enlarged).*

Between two such groups, there is always a straight section where experimental setups, beam diagnostics, the electron cooler, and the injection beamline are mounted.

After acceleration, the ions are injected into the TSR either in a multiturn injection or by the electron cooler stacking method. In the multiturn injection scheme, the closed orbit in the TSR is shifted during injection, so that the beam from the accelerator is scanned over the whole phase space available to the ions, increasing the stored ion current by a factor of ≈ 40, compared to single-turn injection. Even higher ion currents can be accumulated by cooling the stored ion beam to reduce the occupied volume in phase-space, which is repeatedly filled up by additional multiturn-injections.

Typical currents for molecular ions stored in the TSR are 100 nA for multiturn-injection and up to 100 μA in electron cooler stacking mode. Currents in excess of ≈ 5 μA are sufficient for being measured with a DC-current transformer located in one of the straight sections.

The (approximately gaussian) density profile of the stored beam can be measured using the beam profile monitor (BPM), which consists of two micro-channel-plate detectors with position sensitive anodes, one each for the horizontal (x) and the vertical (y) coordinate. Molecules from the residual gas are ionized in collisions with stored particles, and accelerated towards one of the detectors. There, either the x- or the y-coordinate of the collision point is determined by measuring the position of the hit on the detector, and the beam profile in the corresponding direction is obtained as the probability distribution after integrating over many collisions.

3.3 The Electron Cooler

Cooling of the stored ion beam is achieved by merging it collinearly with the intense (10^7 cm^{-3}) beam of the TSR electron cooler device. The electrons are generated in an electron gun by space-charge limited emission from a heated cathode of 3/16" radius [52] at negative potential U_{cath}, and are accelerated by a grounded, ring-shaped anode. The electron gun is mounted inside a strong longitudinal magnetic field B_1 (≈ 1 T), which guides the electrons and decouples their longitudinal and transverse degrees of freedom. After acceleration, the electrons are guided into a region where the magnetic field is adiabatically lowered to $B_2 \approx 20 - 70$ mT, increasing the radius of the electron beam by the *expansion factor* $\beta = B_1/B_2$, which can be set to values of $1 - 30$ by adjusting B_1. The guiding field is bent by 45° two times, with a radius of curvature of $R_{bend} = 800$ mm. In these bending regions (also called toroids because of the shape of the magnets), the electron beam is merged and demerged with the stored ions; in between both beams overlap and move collinearly for 1.5 m.

Through the acceleration and the adiabatic beam expansion, the temperatures $T_{\|}$ and $T_{\perp}$, describing the longitudinal and transverse velocity distribution of the electrons, are lowered from T_{cath} (usually 1100 K) to [53]

$$\begin{aligned} T_{\perp} &= \tfrac{1}{\beta} T_{cath} \\ T_{\|} &= \tfrac{T_{cath}}{2E_{lab}} + C \tfrac{e^2 n^{1/3}}{4\pi\epsilon_0 k_B} \end{aligned} \qquad (3.1)$$

where k_B is the Boltzmann constant, and E_{lab} and n are the average electron energy (in the laboratory frame) and the electron number density, respectively, while the constant C (which is of the order of 1) depends on the acceleration process [54].

Because the electron beam moves in the grounded beam pipe and the beam center is partially shielded from the acceleration voltage U_{cath} by the outer parts of the beam, the kinetic energy

Measurement	β	U_{cath}/V	I_{coll}/mA	E_{cool}/eV
DR & DE of HD$^+$	28.55	393.63	9.45	365.64
	4.00	412.91	10.08	367.45
IC of HD$^+$	9.61	3132.29	183.40	2882.50

Tab. 3.2: *Cathode voltages, collector currents and laboratory-frame energies in the electron cooling mode, for the different experiments, along with the used electron beam expansion factor β.*

E_{lab} of an electron in the laboratory frame is not equal to eU_{cath}. Instead, at a distance r from the electron beam axis it is given by

$$E_{lab} = eU_{cath} - \frac{I_{coll}}{4\pi\epsilon_0 \langle v_{lab} \rangle} \left(1 - \left(\frac{r}{R} \right)^2 + 2 \ln \frac{r_{pipe}}{R} \right) \tag{3.2}$$

where I_{coll} is the electron current between cathode and collector (Fig. 3.1) and $\langle v_{lab} \rangle$ the average velocity of electrons at the radius r, which must be smaller than the radii R and r_{pipe} of the electron beam and the beam pipe. Since $\langle v_{lab} \rangle$ itself depends on E_{lab}, eq. (3.2) is solved by first assuming $\langle v_{lab} \rangle = \sqrt{eU_{cath}/2m_e}$ and then iteratively determining E_{lab} and $\langle v_{lab} \rangle$, until relative changes to $\langle v_{lab} \rangle$ between two steps become smaller than 10^{-5}. An overview of several values of the lab frame energy is given in table 3.2, along with the acceleration voltage and the collector current.

An ion moving with the velocity v in the center of an electron beam experiences the net friction force

$$\langle F \rangle \propto \langle v_{lab} \rangle - v_{ion} \tag{3.3}$$

if $v_{rel} = \langle v_{lab} \rangle - v_{ion}$ is smaller than the velocity spread of the electron beam in longitudinal direction. Since the stored ions pass through the electron cooler more than 10^5 times per second and the electron beam is constantly renewed, the velocity distribution of the ions is narrowed if both beams move at an average relative velocity $\langle v_{rel} \rangle$ of zero, which is called electron cooling.

For average relative velocities different from zero, the cooling force quickly vanishes, but the electron cooler can be employed as an electron target of adjustable relative energy E, which in nonrelativistic approximation (since the ions have velocities $\langle v_{ion} \rangle / c \leq 0.1$) is given by

$$E = \frac{1}{2} m_e \langle v_{rel} \rangle^2 = \left(\sqrt{E_{cool}} - \sqrt{E_{lab}} \right)^2 \tag{3.4}$$

where $E_{cool} = (m_e/m_{ion}) E_{ion}$ is the laboratory energy of the electrons in cooling mode. As Fig. 3.1 shows, the acceleration voltage for the electrons is generated by combining two power supplies, one of them delivering the voltage U_{cool} needed for the cooling mode, and another one which is used to create an offset voltage to U_{cool}, so that $U_{cath} = U_{cool} + U_{offset}$. By using a fast power supply for U_{offset}, it is possible to quickly (few ms) switch between cooling and measurement mode, without affecting the stability of U_{cool}, a process which is called *wobbling.* This adjustment is controlled by a digital-to-analog converter (DAC) converting a number $N = 0 \ldots 4095$ into an output voltage of $-10 \ldots 10$ V, which is then fed into an amplifier generating voltages of $U_{offset} = -1 \ldots 1$ kV.

For each experiment, U_{cath} and I_{coll} have to be calibrated against N. This is done by measuring U_{cath} with a voltage divider of $1:(6050.40 \pm 0.05)$ [59], while I_{coll} is simultaneously measured by the voltage drop over a 1 Ω resistor [59], for about 20 values of N. Analytical expressions for all N are then obtained by fitting the parameters a, b, c, d in the relations $U_{cath} = aN + b$ and $I_{coll} = c(U_{cath} - d)^{3/2}$, so that the electron energy can be calculated for all possible DAC settings from eqs. (3.2) and (3.4).

However, expression (3.4) holds only for parallel beams. In the bending regions of the electron cooler, one has to consider the fact that because of its large radius, the electron beam is overlapping with the ions for some length on both sides of the collinear section (see Fig. 3.1), so that the electrons move at an angle

$$\alpha = \arctan \frac{x}{R_{bend}} \tag{3.5}$$

with respect to the ions, which depends on the distance x from the respective end of the collinear section and also on the radius of curvature of the electron beam ($R_{bend} = 800$ mm). For this alignment of the beams, the relative energy E is (again in the nonrelativistic approximation)

$$E = E_{cool} + E_{lab} - \sqrt{4 E_{cool} E_{lab}} \cos \alpha \tag{3.6}$$

which reduces to (3.4) for $\alpha = 0$. Also, it must be taken into account that the electrons interacting with the ions are not at the center of the electron beam but at a radius

$$r = \sqrt{R_{bend}^2 + x^2} - R_{bend} \tag{3.7}$$

which has to be inserted in (3.2) when calculating the electron energy in the laboratory frame, to account for the different shielding of the acceleration voltage by space-charge. The maximum energy shift caused by this effect occurs at the effective length l_{eff} of the bending regions, which is equal to the position where the surface of the electron beam crosses the ion trajectory ($r = R$):

$$l_{eff} = \sqrt{2R^2 + R R_{bend}} \tag{3.8}$$

In measured rate-coefficient spectra, this effect causes a background which has to be subtracted in the data analysis. This is done by convolving the measured rate coefficient with the known energy and velocity distributions[1] in the electron cooler, which yields a first-order approximation of the toroidal background (also as a function of relative energy). This estimated background spectrum is subtracted from the measurement, yielding the background subtracted rate coefficient, also in first order of approximation. The process is then iterated (usually 10-20 times) to obtain a higher precision in the background subtracted spectrum, which with increasing order of approximation converges to the rate coefficient expected without any influence from the toroid sections [56, 57, 58]. This procedure is applied in Chapters 4.3 and 5.3.

The background can be significantly suppressed (at some expense on energy resolution) by choosing a small expansion factor β for the electron beam. This simultaneously reduces the effective length l_{eff} of the bending regions and also the maximum energy shift, which is reached at their respective ends. This method was applied with good success in one of the measurements on the DR and DE cross section, lowering the background almost by a factor of 4 in the interesting energy regions, compared to full possible beam expansion.

3.4 Detectors

The fragment atoms coming from the interaction region of the electron cooler are detected in a chamber located $\approx$6 m downstream, behind the next TSR dipole magnet which deflects all charged fragments so that only neutral particles may reach the detectors.

The chamber is connected to the TSR by a valve (which is not shown on Fig. 3.1), and has to be pumped to ring pressure before opening. This seriously limits the choice of materials for detectors and other equipment to be mounted in the chamber. Currently, the following detectors are available: a semiconductor of 60×40 mm size which is sensitive to the kinetic energy of the particles (used for particle counting in the DR/DE measurements in Chapter 4.2), for rates up to $\approx$5000 s^{-1}; a micro channel plate (MCP) of 75 mm diameter, attached to a phosphorous screen for measuring fragment distances with a ccd-camera/framegrabber imaging system through the chamber window; and (for particle counting at rates up to 10^6 s^{-1}) a micro sphere plate (MSP) with a metal anode, of 65 mm diameter, with an aluminum foil of 1.5 μm thickness in front and a centered horizontal slit of 40×6 mm [55], which was used in the IC measurement (Chapter 5.2). The MCP can be mounted on a flange at the end of the chamber (instead of the window), and can be used in conjunction with any one of the two other detectors, which

---

[1] Instead of eqs. (3.5) and (3.7), measured values [60] for the angle α and the distance r as a function of x are used in the calculation.

hang down from a manipulator into the chamber and may be moved in or out vertically.

In addition, there is a shutter mounted in the chamber, which is operated from the outside with compressed air and can be triggered remotely by an electric valve. It is used to protect the MCP or semiconductor detector from the very high fragment rates occuring during injections into the ring, or when the TSR has to be adjusted. Last, there is a horizontal manipulator arm available, holding a scraper for testing the fragment beam position.

3.5 Laser System and Beam Transfer Optics

In addition to the equipment mounted on the ring itself, there is also a laser system [55] available which has been used in the measurement of the cross section of vibrational excitation of HD^+ in inelastic collisions with electrons. The Laser system consists of a pulsed XeCl-Excimer (Lumonics EXC 610) emitting at 308 nm, and a dye-laser (Lambda-Physik FL2002), which is pumped by the excimer laser. The amplifying medium for the oscillator and the preamplifier of the dye-laser is contained in the same cuvette, where 10% and 20% of the light from the excimer laser are directed at different positions by two beamsplitters, the rest being coupled into the main amplifier cuvette. The laser was operated with QUI, a dye with a tunable range of $368 - 402$ nm, and a peak quantum efficiency of 11 % at a wavelength of 390 nm, which was solved in dioxane ($C_4H_4O_2$) at a concentration of 0.20 g/l for the oscillator/preamplifier, and at 0.067 g/l for the main amplifier. Tuning of the laser wavelength is accomplished by tilting an optical grid making up one of the cavity mirrors of the dye laser; the output wavelength was fixed at 380 nm throughout the experiment. At a repetition rate of 200 Hz, the excimer laser provided pulses of about 150 mJ, resulting in pulses of $\approx$10 mJ from the dye laser, at a pulse length of $10 - 15$ ns.

The beam from the dye laser was directed through a Gallileian telescope to allow manipulation of its cross section and divergence, and then coupled into the TSR by a beam transfer line of 6 mirrors with dielectric coating of $\geq$99.5% reflectivity, and an entry window mounted at the end of the detector chamber. Because the beam had to pass through the slit in the MSP detector and have an almost constant width thereafter, the telescope was adjusted such that the beam had a cross section of 5×2 mm^2 at the entry window, and was focused a few meters beyond the exit window at the beam dump in figure 3.1. The total pulse energy was reduced by $50 - 70$ % by absorption in the entry window and also by the air in the transfer line, amounting to $3 - 5$ mJ inside the interaction region of the electron cooler.

By shifting and tilting the two mirrors closest to the ring, the position and angle of the laser beam could be adjusted independently for the horizontal and vertical directions, with accurracies of 0.1 mm and 0.1 mrad. In order to achieve a good overlap with the ion beam in the interaction region of the electron cooler, the position of the neutral fragment beam was determined with two scrapers (Fig. 3.1 and 5.2): one close to the MSP detector, and one at the end of the interaction region (blocking only the fragments but not the stored ion beam, see Fig. 5.2). Then only one of the scrapers was inserted at a time, at the measured position of the ion beam, and the laser beam was adjusted so that it would be half blocked, with the first scraper being used to set the laser beam position at the entry window and the MSP detector, and the other one for setting the beam angle.

3.6 The TSR Data Acquisition System

The experiments described in this work have been carried out using the TSR data acquisition system for control and read-out of the respective electronic setups. The system has been used at the TSR for several years, and also the two measurements of the DR and DE cross section described in Chapter 4.2 have been done with it. However, the computer hardware controlling the measurements had to be renewed recently, making it necessary to port the software to contemporary operating systems. The opportunity was used for replacing or altering some of the system's software components, leading to a new program suite called CyrilNG. Since the measurement on the inelastic collisions in Chapter 5.2 was the first experiment to make use of the new software it is briefly explained below, although a manual is also available in electronic form[61, 62].

A typical experiment as shown in Fig. 3.2 employs an electronics setup consisting of NIM and CAMAC modules and two computers interconnected by a network. The CAMAC modules are read out by a VME-bus computer (lynxonline) with a Power-PC 601 CPU on a CETIA VMTR2 card, operating under LynxOS 2.3.1, where a Kinetic Systems KS2917 card is used as an interface between the VME and the CAMAC bus. After readout, data are transmitted by ethernet to an industry-standard PC (pconline) operating under Linux (kernel version 2.4.1), where they are written to disk.

Measurements are done in an event-based way, which means that input signals are processed by the CAMAC modules until a certain condition arises, e.g. an injection into the TSR which triggers a LAM in one of the modules, or the user pressing a key, which generates a software exception. Both are detected by the `expt` program running on lynxonline, which is configured by a table containing possible *events* and corresponding instructions. This table is split into two configuration files: the setup-file and `user_functions.c`. The setup-file contains a list of the accessed CAMAC modules and their respective crate/node numbers, as well as several lists of CAMAC functions, where each list corresponds to one possible event.

While the setup-file is read each time `expt` is started, the `user_functions.c` file is actually a

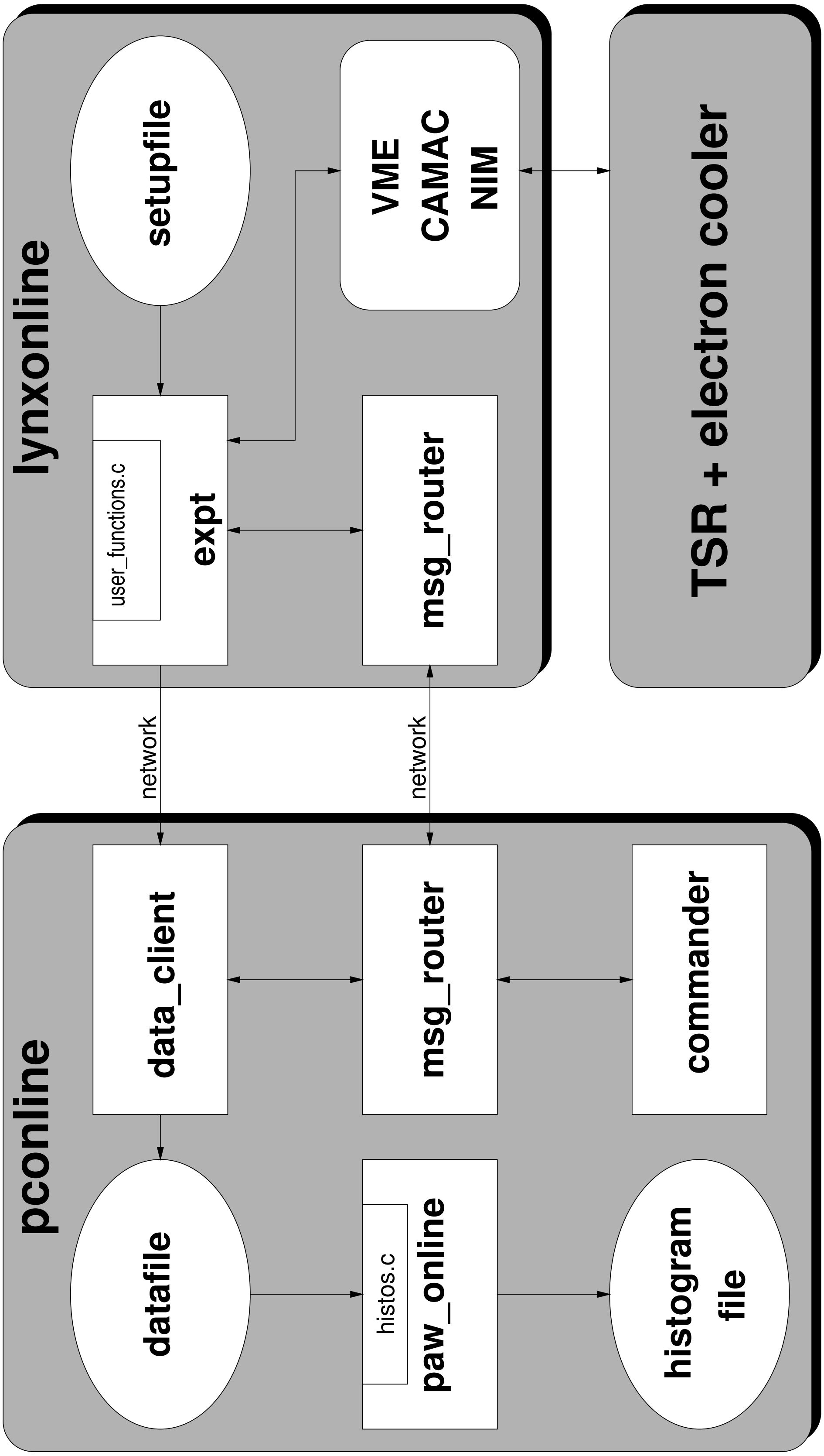

Fig. 3.2: *Components of the TSR data acquisition system. Programs are depicted as rectangular boxes, nonexecutable files as ellipses and hardware as rounded boxes. Arrows indicate the direction of data or control information flow.*

part of the program. Thus, it must be compiled and linked against a skeleton version of `expt` each time it is to be changed. This procedure allows to define more complex conditions and actions for each event: for example the "wobbling" and stepping of the electron acceleration voltage described in Chapter 4.2 was accomplished this way. For ease of configuration, the setup-file contains an optional block of parameter settings, as well as up to 20 additional CAMAC function lists which can be used in `user_functions.c`.

All data obtained by `expt` are accumulated and buffered in binary integer format until either the buffer memory is full or an especially marked event occurs. Then the buffer content is transferred over ethernet to the `data_client` program running on pconline, which checks the data for transmission errors and translates them into numbers in ASCII format, before storing to disk. Transmission errors between lynxonline and pconline occur rarely with an intact network, therefore they are only reported and invalid data is not retransmitted.

Finally, all data have to be displayed and analyzed while the measurement is proceeding (online analysis). This may be done in either of two ways:

1. By using the data display and experiment control tool `cyrildesktop`[62], which comes with the program suite and runs as an independent task on pconline. Each time `data_client` appends the datafile, `cyrildesktop` will read the newly appended part and perform a set of predefined operations on the incoming data, which is then sorted into vectors and displayed in several ways. Similar to `expt`, this flexibility is achieved by splitting the `cyrildesktop` into a skeleton program and a source file `user_display.c`.

2. In conjunction with the program `paw_online`, which sorts raw data into user-defined histograms, which are stored to disk in the `hbook` file format used by `paw/pawX11`. Also needing an additional source file (`histos.c`) containing the histogram definitions and filling prescriptions, this program allows for the same operations with data as `cyrildesktop`, except that the pre-processed data is saved to disk instead of being displayed. The advantage is that data may be analyzed and displayed interactively with `paw`, thus allowing to do least-square-fits or further numerical operations as the need arises.

Control over the experiment is achieved by the definition of special events in `expt`, which correspond to the initialization of CAMAC hardware and to the starting, stopping and continuing of a measurement run. Also for these events, a CAMAC list and a C function can be defined either in the setupfile or in `user_functions.c`.

Such events can either be generated by `cyrildesktop`, or by an additional program called `commander`, which has to be used in combination with `paw_online` and provides a text-only interface to experiment control. In both cases, the user selects the appropriate event from a menu on the screen, and the program sends a message to `expt`. Messages (which are routed by the `msg_router` programs running on both computers) always consists of a text string containing the name of the target program and of the event, and a path for the setup-file or the data file if needed. This message forwarding method is also used for transmission of control information between `expt` and `data_client`, but not for data transmission.

4. Dissociative Recombination and Excitation of HD^+ with Electrons

This chapter describes the absolute measurement of the rate coefficients for DR and DE of HD^+ ions with electrons, as a function of the relative energy in the range of 1 meV to 30 eV. After introducing the principle of the measurement and the electronics setup, the evaluation of the obtained data will be presented. The last section will then focus on the interpretation of the measured rate coefficient spectra and the comparison with present theory.

4.1 Measurement of Absolute Rate Coefficients

In the experiment, ions of ≈ 2 MeV kinetic energy were stored in the TSR and merged with the beam from the electron cooler along its collinear section, which has a length of $L_{EC} = 1.49 \pm 0.01$ m (Chapter 3.3). Electrons moving close to the axis of the beam may thus react with the ions, eventually undergoing dissociative recombination or excitation. As explained in Chapter 2.2.3, atomic fragments are produced by both reactions, the DR mainly yielding pairs of neutral H and D fragments, while one neutral and one charged atom are produced by DE. The rate of neutral fragments from either reaction is measured with the semiconducting solid-state detector mounted in the vacuum chamber 6.5 m downstream from the electron cooler, while charged fragments are deflected by a TSR dipole magnet between electron cooler and detector.[1]

The time resolution of this detector is too limited to separately count H and D fragments from the same dissociative recombination event, which arrive with a typical time difference of $1 - 10$ ns. But since it provides an energy resolution (which maps to a mass resolution for particles of the same velocity), it is still possible to distinguish whether the detected fragments originate from DR or DE: In the first case, the full ion mass is measured since both fragments reach the

---

[1] The fragments are deflected so strongly that it is also impossible to measure them with the TSR ionization detector, which is mounted behind the dipole and close to the trajectory of the stored ions. A new detector system, currently under construction, will provide this feature.

detector, while in DE only a fraction $\frac{m_H}{m_{HD}}$ or $\frac{m_D}{m_{HD}}$ of the ion mass is measured, depending on which fragment is produced in the neutral state.[2] Thus, by discriminating the detector signals within three mass windows, the rates R_{H+D^+}, R_{H^++D} and R_{H+D} for the different fragment combinations are measured by detecting only the neutral ones ($R_{H+D^+} = R_H$ and $R_{H^++D} = R_D$). These rates are given by the cross section for either process and the number N_{ion} of ions stored in the TSR:

$$R_{H+D}(E) = \frac{L_{EC}}{L_{TSR}} N_{ion} \sigma_{DR}(E) v_{rel} n_e \tag{4.1}$$

$$R_H(E) + R_D(E) = \frac{L_{EC}}{L_{TSR}} N_{ion} \sigma_{DE}(E) v_{rel} n_e \tag{4.2}$$

where the number density n_e of electrons in the beam has to be known as a function of the adjusted relative energy $E = \frac{1}{2} m_e v_{rel}^2$ (v_{rel} being the mean relative velocity between ions and electrons). The length ratio $L_{EC}/L_{TSR} = 0.0269 \pm 0.0002$ between the electron cooler and the circumference of the ion orbit reflects the idealization that both beams are assumed to overlap only in the 1.5 m long collinear section of the electron cooler. The additional overlap between ions and electrons in the bending regions adjacent to the colinear section is neglected in the formula, and thus causes a background in the measurement which has to be subtracted in the data analysis.

It is often useful to introduce rate coefficients $\alpha_{DR,DE}$ instead of $\sigma_{DR,DE}$, which for astrophysical plasma usually refers to the product of the cross section and the relative velocity of the electrons, averaged over a thermal velocity distribution. But since the velocity spread in the electron beam is very small, it is accounted for by an experimental energy resolution ΔE, and the approximation $\alpha_{DR,DE}(E) = \sigma_{DR,DE}(E) v_{rel}(E)$ is used for the measured rate coefficents.

These are obtained from the rate of neutral fragments, measured as a function of energy and normalized to the momentarily stored number of ions and to the number density of electrons. Since the number of stored ions cannot be measured directly, it is deduced from the electric current I_{ion} created by the moving ions, which was measured by the DC transformer mounted at the TSR (Chapter 3.2)

$$N_{ion} = \frac{I_{ion}}{qef_{TSR}} \tag{4.3}$$

with the electric charge qe of a single ion and the orbital frequency $f_{TSR} = v_{ion}/L_{TSR}$, so that the rate coefficients become

$$\alpha_{DR}(E) = \frac{qef_{TSR}}{n_e} \cdot \frac{L_{TSR}}{L_{EC}} \cdot \frac{R_{H+D}(E)}{I_{ion}} \tag{4.4}$$

---

[2] The small mass difference between the stored ions and two neutral fragments, which is caused by the captured electron, is far below the detector resolution.

$$\alpha_{DE}(E) = \frac{qef_{TSR}}{n_e} \cdot \frac{L_{TSR}}{L_{EC}} \cdot \frac{R_H(E) + R_D(E)}{I_{ion}} \tag{4.5}$$

for dissociative recombination and dissociative excitation, respectively.

4.2 Setup and Data Acquisition

Two measurements of $\alpha_{DR}(E)$ have been carried out during two TSR beamtimes, each of one week duration. The first one was done with a strongly expanded electron beam to achieve the maximum possible energy resolution at low relative energies, while the second used a much reduced expansion to increase the electron density and in consequence also the DR fragment rate, for a dedicated measurement at relative energies of $1-4$ eV where the DR rate coefficient is very small. The smaller expansion also shortened the beam overlap in the bending regions of the electron cooler, which is also very important at $1-4$ eV. Table 4.1 contains a compilation of the relevant experimental parameters for both measurements.

Both measurements were carried out with almost the same setup, which is shown in Fig. 4.1 for the experiment with the wide electron beam. In a combination of two amplifiers, the output charge from the solid state detector was first integrated and then differentiated with a different time constant, to yield a voltage signal which was converted into a digital number between 0 and 511 by an ADC of 9 bit resolution. This number was fed to a multiscaler-memory module, which was used to accumulate and store three different amplitude histograms of the detector signals, with a resolution of 512 bins each (the purpose of the router module between ADC and memory is explained further down). At the same time, the stored ion current was measured by converting the output voltage of the DC transformer into pulses of proportional frequency which were counted by a scaler. In addition, the trigger signals of the beam profile monitor (BPM, whose rate is proportional to the stored current, if the TSR vacuum remained constant)

R [mm]	n_e [cm^{-3}]	E_{cool} [eV]	ΔE_{0eV} [meV]	ΔE_{1eV} [meV]	l_{eff} [mm]	E_{max} [eV]
25.4	$2.6 \cdot 10^6$	365.64	6	31	203	22.1
9.5	$1.9 \cdot 10^7$	367.45	40	72	124	8.8

Tab. 4.1: *Parameters for the rate coefficient measurements. R: electron beam radius, E_{cool}: electron energy (laboratory frame, at $E=0$ eV), n_e: electron density (at $E=0$ eV), l_{eff}: effective length of beam overlap in each toroid section, E_{max}: maximum shift of relative energy in toroid sections (at $E=0$ eV), ΔE: FWHM energy resolution at the indicated relative energy, derived from the longitudinal and transverse temperatures of the electron beam.*

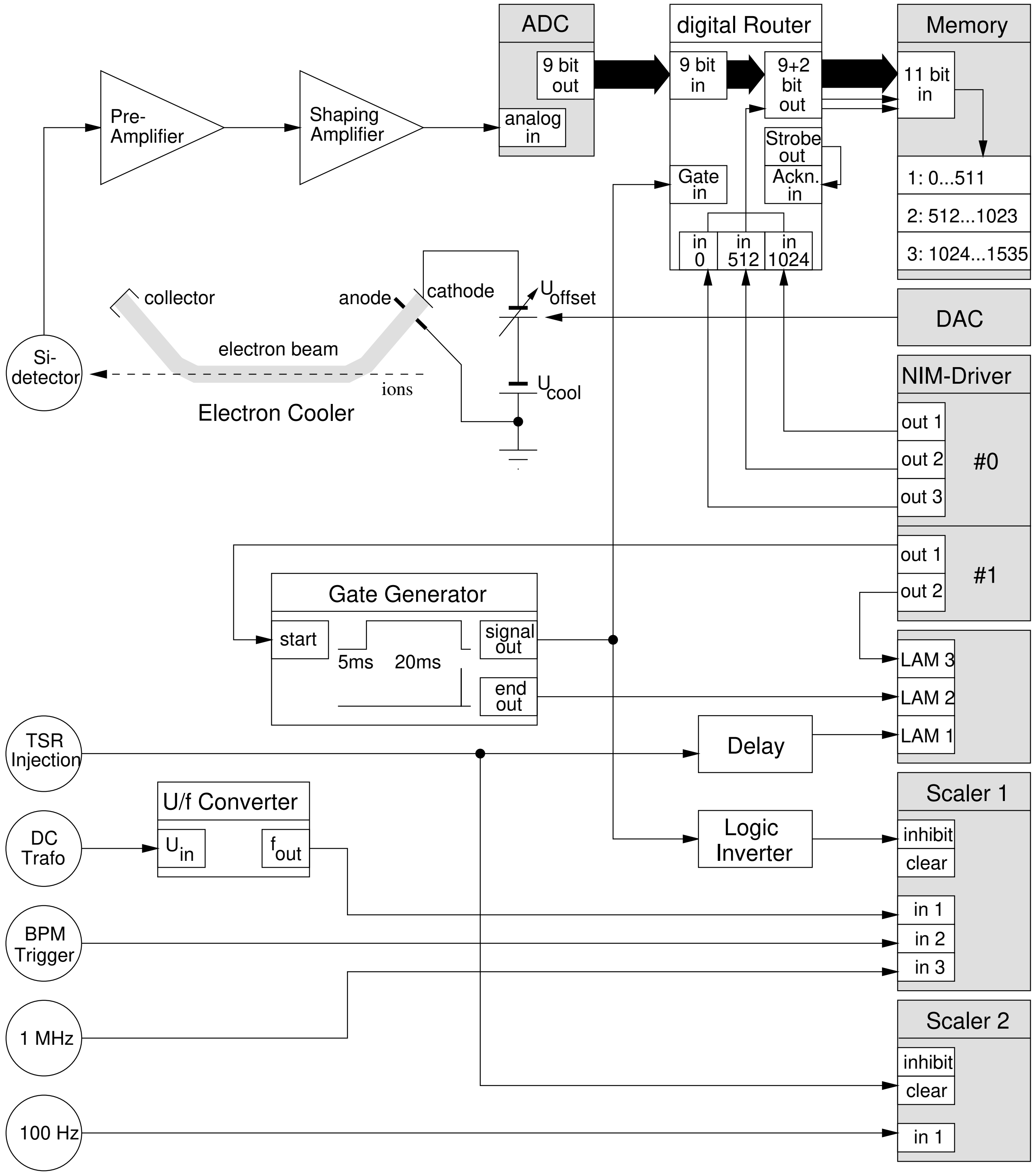

Fig. 4.1: *Setup for the measurement of the DR and DE rate coefficients of HD$^+$. Grey boxes: CAMAC modules; white boxes: NIM or standalone modules; white circles: input signals.*

and a 1MHz clock signal as a time reference were also fed to the scaler. The setup for the narrow electron beam differed only by omitting the measurement of the DC transformer output and the BPM trigger rate.

After each injection into the TSR (every $15 - 30$ s), the offset voltage to the cathode of the electron cooler was set to 0 V, leaving the cathode on the voltage U_{cool} for electron cooling of the stored ion beam. After a pre-cooling phase of several seconds (determined by a digital delay generator), a CAMAC interrupt (LAM 1) was generated, which started the data acquisition. During the measurement, the relative energy of the electrons was rapidly cycled between three settings (a process which is also called “wobbling”): The first step was always done at the selected measurement energy E, which was changed with each injection to obtain an energy scan; the second one corresponded to electron cooling mode, to maintain a sharp distribution of the ion velocity, while the third step was a reference setting E_{ref} which was kept constant throughout the experiment. This reference step was of particular importance to the measurement with the wide electron beam: there it was set to a relative energy of ≈ 37 eV, where the DR rate coefficient is vanishingly small and neutral fragment pairs are only produced in collisions between stored ions and residual gas molecules in the TSR vacuum system. The rate R_{H+D} measured during this step is therefore used for a subtraction of residual gas-induced background to the DR rate coefficient. In addition, the reference step serves to prevent systematical errors from the wobbling precedure at very low measurement energies (several meV): If the electron energy is switched from cooling to measurement mode under these conditions, the electron velocity increases slowly enough that the ions adiabatically follow by the cooling force (Chapter 3.3), resulting in an acceleration of the ions which shifts the relative energy towards zero. Therefore, the reference step with its rapid change in relative velocity was placed between the cooling and the measurement steps, so that the relative energy is always adjusted *down* towards the measurement value. Since the experiment with the narrow electron beam aimed at much higher energies ($1 - 4$ eV), this precaution was not needed, and E_{ref} was set to zero for improved electron cooling.

At the beginning of each wobbling step, the ADC and the scaler measuring the ion current were disabled for 5 ms, by switching off a gate signal to the router module between ADC and memory module, and by raising an “inhibit” signal to the scaler. This gave the power supplies of the electron cooler some time for adjustment to the new cathode voltage; after that the ADC and the scaler were activated for 20 ms. Also, corresponding to the current wobbling step (reference, measurement, or cooling mode), either one of the three outputs of the upper NIM-driver (a programmable I/O register) was set, which decided whether the digital router let the ADC output pass to the memory module unchanged (reference step), or if 512 (measurement) or 1024 (cooling) was to be added in between. This way, a separate histogram was kept in the memory module for each of the three wobbling states. After 20 ms of data taking, the ADC and the scaler were again disabled and a LAM 2 was generated. Upon this the measurement software first read out both scaler contents, then cleared the one used for the ion current measurement, switched the electron cooler energy to the next wobble state and finally started the next sequence of 5 ms delay and 20 ms of data taking with the second NIM-driver. Because the transfer of data from the memory module to the measurement computer system takes a few ms to complete, the histrograms in the memory module were accumulated until a another interrupt (LAM 3) was received, which was generated by the software instead of LAM 2 after a certain number of wobble steps (at intervals of ≈ 1 s). The storage time was also read out at these occurences, using a combination of a 100 Hz clock signal and the second scaler, which was only cleared by the injection signal.

4.3 Analysis

In the example ADC histogram shown in Fig. 4.2, the peaks corresponding to the mass of single H or D and coincident H+D fragments are clearly visible. Because the peak corresponding to H fragments cannot be separated from the electronic noise (visible to the left in the ADC histogram), only the fragment numbers N_D^i and N_{H+D}^i were integrated for each readout of the three ADC histograms, with $i \in \{\mathrm{ref}, \mathrm{meas}, \mathrm{cool}\}$ denoting the corresponding wobble steps. These count numbers were converted into the rates R_D^i and R_{H+D}^i by normalizing to the length of the ADC gate signal τ_{gate}^i, which was measured with scaler 1. But before these rates could be averaged over all measurements done at a particular energy and wobbling step, and be inserted in (4.4) and (4.5), several cuts had to be applied to the measured data. Since these are different for the two rate coefficients, and also depend on the experimental conditions, each measurement is discussed in a separate section below.

Also, the effects of the finite time resolution of the shaping amplifiers (and thus imperfect distinction between correlated and uncorrelated particles in the ADC histograms) had to be compensated prior to any further data evaluation: If fragments from different DR or DE events arrive at the detector with a time difference shorter than the integration constant of the shaping amplifier, they will appear as a single particle having the total mass of the fragments. This is visible as an additional peak at twice the mass of a D particle, in the magnified region of Fig. 4.2, which is caused by coincidences of deuterium fragments from two DE events, and also at higher masses from coincidences involving fragment pairs from DR. It is therefore expected that the peak corresponding to the mass of a DR fragment pair also contains a contribution of coincident H and D particles from two DE events.

Hence, a procedure was developed to eliminate these coincidences in R_{H+D}, which is described

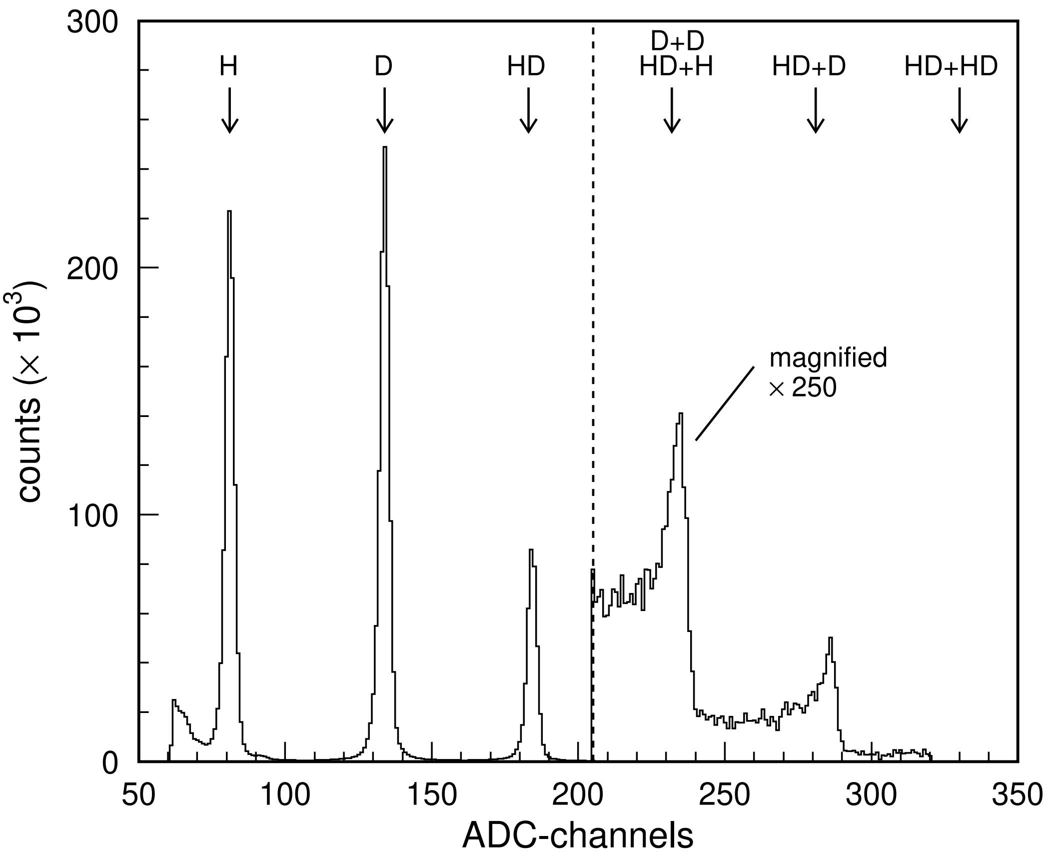

Fig. 4.2: *Mass spectrum of fragments from DR and DE, obtained by digitizing the signals from the solid-state detector at reference energy. The magnified zone on the right shows the additional peaks arising from signal pileup, at masses corresponding to the coincident hit of uncorrelated particles. Pileup between DR events (HD+HD) is not seen because the corresponding signal amplitude exceeds the dynamic range of the shaping amplifier, which cuts off the spectrum at* 320 *ADC-channels.*

for both measurements in appendix A, and is from hereon assumed to be already applied to the data.

DR of HD$^+$ with the wide electron beam

Before obtaining the DR rate coefficient from the measured particle rates by (4.4), I_{ion} has to be known at all times during the experiment. But since the minimum current of several μA needed for a reliable measurement with the DC transformer and the voltage-to-frequency converter (VFC) is so high that the resulting fragment rate would destroy the solid state detector, $\alpha_{DR}(E)$ in (4.4) was normalized to R_D^{ref} instead of I_{ion}. This rate is measured along with R_{H+D}^{meas} at all times and is proportional to I_{ion} because of the constant reference energy:

$$I_{ion} = \zeta R_D^{ref} \tag{4.6}$$

The constant ζ was determined in several steps. First, to bridge the gap to the ion current neccessary for the DC transformer to work, R_D^{ref} was related to the trigger rate of the beam profile monitor (which is also proportional to the stored ion current) by determining

$$\lambda = \frac{dR_{BPM}}{dR_D^{ref}} \tag{4.7}$$

for each measurement run. Aside from influences on the BPM signal by changes of the residual gas pressure, the results in Fig. 4.3(a) show a dependence on the storage time: an average value of $\lambda = 3.81 \cdot 10^{-3} \pm 1\%$ is obtained for runs with a measurement window of $t = 5 - 12$ s after injection, whereas $t = 15 - 22$ s yields $\lambda = 3.43 \cdot 10^{-3} \pm 0.5\%$. The difference is probably caused by a dependence of the BPM efficiency on the diameter of the ion beam, which changes with storage time because of electron cooling. Since this experiment focuses on the rate coefficient at low electron energies, which must be measured at long storage times (see below), only the second value is applied; the dependence of λ on the storage time is accounted for by enlarging the experimental error by the difference between both values:

$$\lambda = 3.43 \cdot 10^{-3} \pm 12\% \tag{4.8}$$

Then the BPM rate was related to the rate of the voltage-to-frequency converter (VFC) measuring the output of the DC transformer. Three dedicated measurement runs were done, during which the detector chamber was closed so that ion currents of $5 - 20$ μA could be accumulated by the electron cooler stacking method, without endangering the solid-state detector. From the measured rates of the VFC and the beam profile monitor shown in Fig. 4.3(b)-(d), the calibration factor

$$\eta = \frac{dR_{VFC}}{dR_{BPM}} \tag{4.9}$$

was determined, yielding the values $\eta_1 = 0.1361(4)$, $\eta_2 = 0.1295(12)$ and $\eta_3 = 0.1219(7)$. By fitting these with a constant, a weighed average was determined; its experimental error was set to the standard deviation between the three measurements because of their large differences:

$$\eta = 0.132 \pm 6\% \tag{4.10}$$

Next, the calibration $\iota = dU_{in}/df_{out}$ of the VFC itself was determined by measuring its output frequency at several defined voltages (Fig. 4.4):

$$\iota = \frac{dU_{VFC}}{dR_{VFC}} = 20.6\ \mu\mathrm{V/s}^{-1} \pm 1\% \tag{4.11}$$

while the stored ion current is obtained from the voltage fed to the VFC by the known calibration of the DC transformer

$$\kappa = \frac{I_{ion}}{U_{VFC}} = 1\ \mu\mathrm{A/mV} \tag{4.12}$$

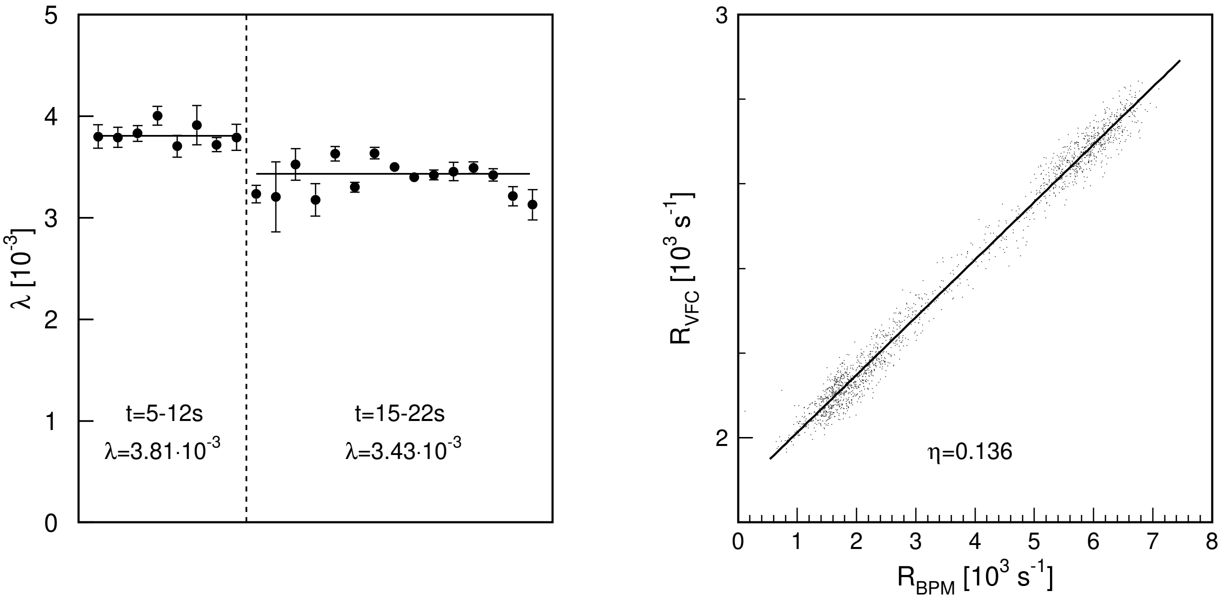

(a) Relation between R_D^{ref} and R_{BPM} for all measurement runs (Dots) and average values for each storage time window (solid lines).

(b) -(d) Results from the three runs with high ion current (Calibration of R_{BPM} to R_{VFC}).

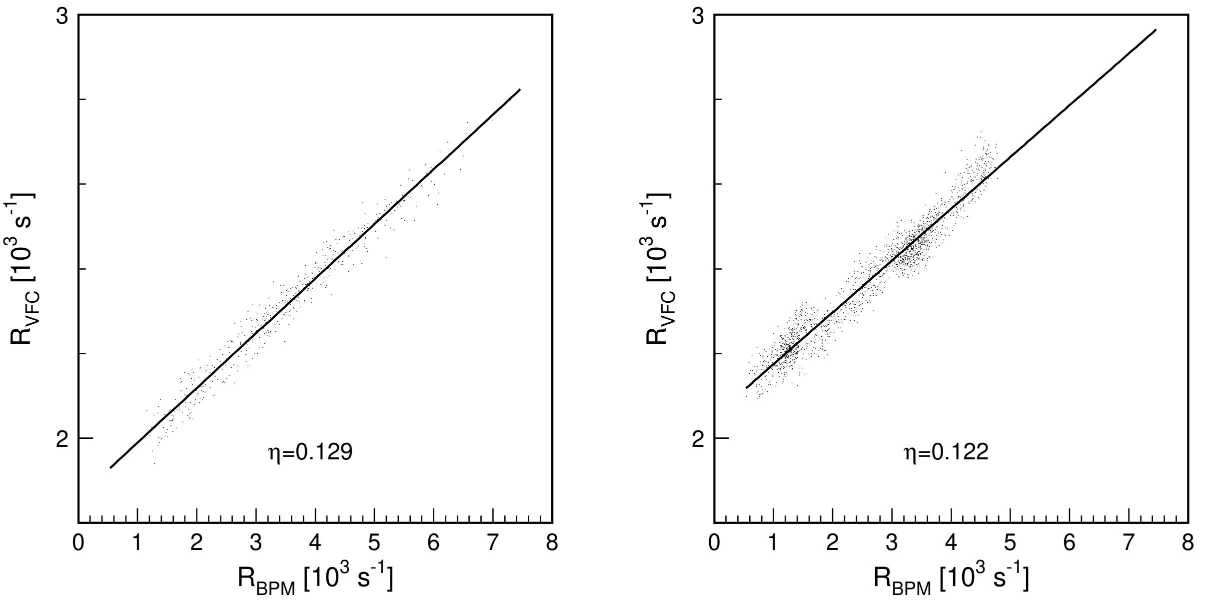

Fig. 4.3: *Calibration of* R_D^{ref} *to the output of the VFC measuring the stored ion current. Conversion of* R_{VFC} *to* I_{ion} *is done with the internal calibration of the VFC and the DC transformer.*

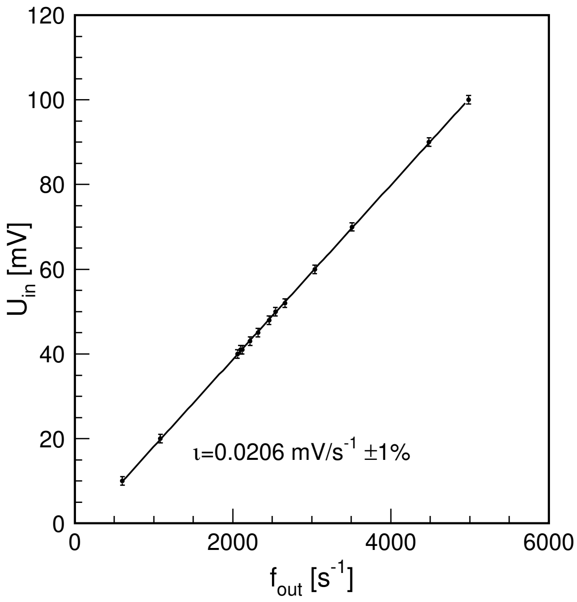

Fig. 4.4: *Calibration of the voltage-to-frequency converter slope ($\iota = dU_{VFC}/dR_{VFC}$)*

This way, the stored ion current is known also during the measurement of the rate coefficient, by applying the total calibration factor

$$\zeta = \lambda\eta\iota\kappa = 9.3\ \mathrm{pA/s^{-1}} \pm 19\% \tag{4.13}$$

to (4.6). The relative error in ζ was obtained from the linear sum of the respective relative errors from the four calibration steps (instead of their gaussian sum), to obtain an estimation of the maximum error in the calibration.

However, the (very small) background of H+D fragment pairs from collisions between ions and residual gas molecules still has to be eliminated. This background subtraction makes use of the fact that at very high electron energies such as E_{ref} the DR rate coefficient is mainly determined by the Franck-Condon overlap between the HD$^+$ ground state and the rydberg states of the Q2 series of HD, which becomes very small. The substitution $R_{H+D} \mapsto R^{meas}_{H+D} - R^{ref}_{H+D}$ is therefore made in (4.4), so that the measured absolute rate coefficient for dissociative recombination becomes

$$\alpha_{DR}(E) = \frac{qef_{TSR}}{\zeta n_e} \cdot \frac{L_{TSR}}{L_{EC}} \cdot \frac{\left\langle R^{meas}_{H+D}(E) - R^{ref}_{H+D}(E)\right\rangle}{\left\langle R^{ref}_{D}(E)\right\rangle} \tag{4.14}$$

where $\langle\quad\rangle$ indicates the averaging over all measurements done at a particular energy.

Because σ_{DR} diverges for $E \to 0$ eV, the measured rate coefficient is strongly influenced by the distribution of v_{rel}, which again depends on the duration of the electron cooling applied to the stored ions before the measurement. It was found that even after prolonging the precooling

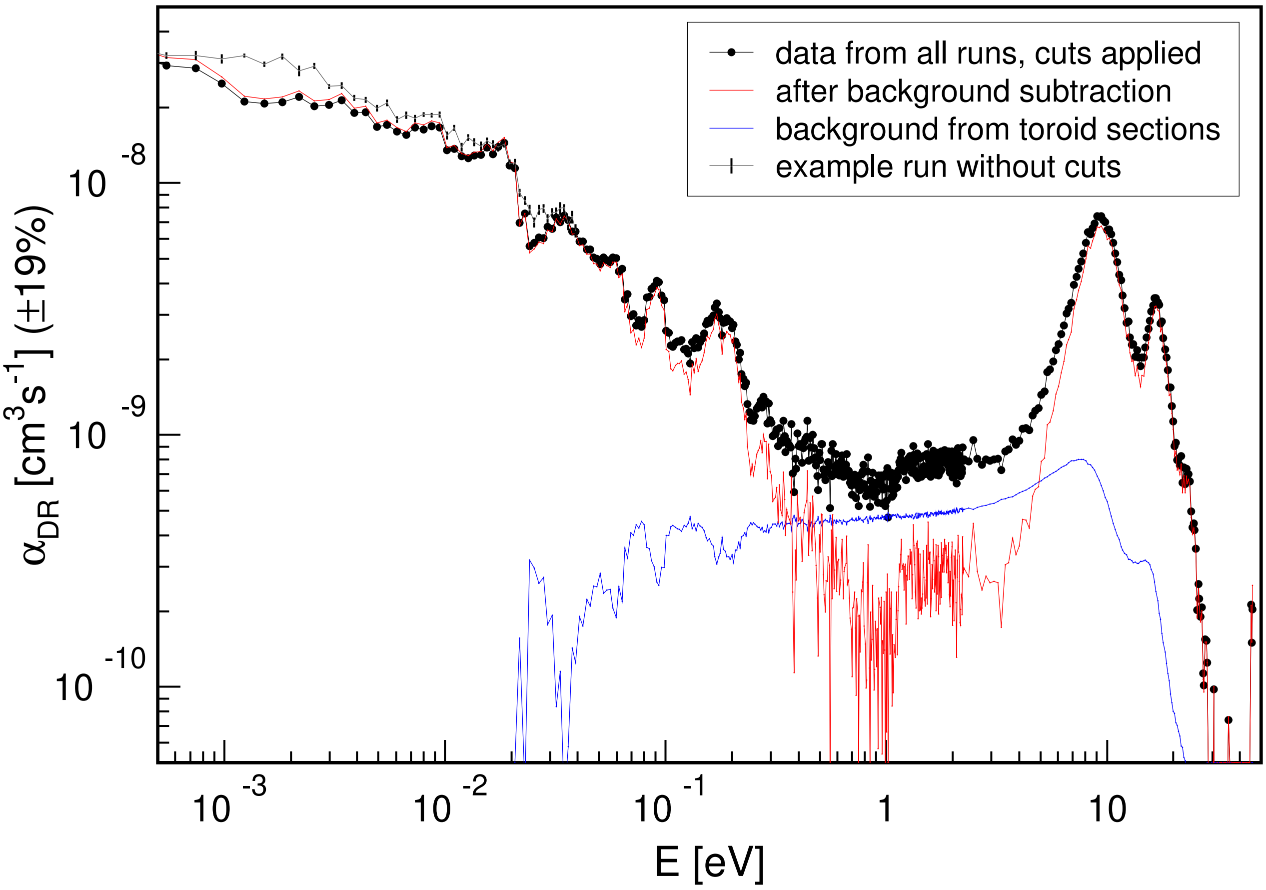

Fig. 4.5: *Measured rate coefficient for dissociative recombination with the wide electron beam, after applying the cuts from table 4.2 (black) or without them (grey). Also plotted is the contribution from the energy shift in the toroid regions of the electron cooler (blue), which has been subtracted from the measured spectrum to obtain the background-subtracted rate coefficient (red).*

Energy range	0 – 6 meV	6 – 40 meV	> 40 meV
minimum required time for precooling	8 s	1 s	1 s
minimum required storage time	14.5 s	14.5 s	4.5 s

Tab. 4.2: *Definitions of cuts applied to the measured data. For a given energy, a minimum duration of the precooling phase is required. In addition, data is only accepted after a minimum total time of storage (precooling plus wobbling). New injections into the TSR have been done after a total storage time of either 14 s or 24 s; in measurements with the shorter storage time, the precooling phase always lasted 1 s, while either 1 s or 8 s were applied with the longer injection interval.*

phase from 1 s to 8 s by changing the controlling delay in the electronic setup, α_{DR} was still smeared out at energies larger than the resolution ΔE of the electron beam. Therefore the cooling steps in the wobbling scheme were used to further prolong the precooling time with decreasing relative energy, by applying the set of cuts listed in table 4.2 before averaging over all measurements in eq. (4.14).

The importance of a sharp distribution of v_{rel} can be seen in Fig. 4.5: the black line shows the measured rate coefficient obtained from the cut data only, while the grey line represents the result of one measurement done with short precooling time, without the cuts being applied. The statistical errors from the measurement of R^{meas}_{H+D}, R^{ref}_{H+D} and R^{ref}_{D} are not plotted, since they are very small except between $0.2-4$ eV, where they are reflected by the scattering of the data points. In contrast, the error of ±19% from the calibration of R^{ref}_{D} to I_{ion} applies only to the global scale of the spectrum, but has no effect on the difference of α_{DR} between two data points; it is therefore indicated on the rate coefficient axis.

However, the black curve still contains a background of events originating from the toroid sections of the electron cooler, where the beams are merged and demerged (blue curve). This contribution to the measured rate coefficient was calculated by the method described in /mbox-Chapter 3.3, and has been subtracted from the data to obtain a background-free spectrum of the rate coefficent (red curve). At low energies, α_{DR} is increased by the background subtraction, because of a very slight energy detuning already inside the interaction region which is only important for the steep slope of α_{DR} around $E=0$ eV.

Although the influence of statistical errors of measured data on the calculated background is very small, systematical errors arise from the calculation of the energy distribution in the toroid sections. These errors are not exactly known, but were estimated by comparison with the measurement using the narrow beam, to at least 10% of the calculated background. At $1-4$ eV, this leads to an additional systematical error of ±17% in the background subtracted rate coefficient.

DR of HD$^+$ with the narrow electron beam

Because of the small statistical sample arising from the very low rate coefficient of $\approx 2\cdot 10^{-10}$ cm^{3}s^{-1}, a dedicated measurement has been caried out for the energy region $1-4$ eV [3]. Reaction rates were increased by almost one order of magnitude by reducing the expansion of the electron beam from 28.55 to 4, leading to a typical electron number density of $2\cdot 10^{7}$ cm^{-3} at a beam radius of 9.5 mm. To protect the detector from damage by high fragment rates, the shutter in front of it (Fig. 3.2) was automatically closed before each injection, and was opened only after the precooling phase.

The narrow profile of the electron beam also reduced significantly the magnitude of the toroid background, because the effective length of each bending region was shortened from 203 mm to 124 mm by the altered beam geometry. In addition, the maximum energy shift in the bending regions reduced from 23.6 eV to 9.6 eV, which because of the nonlinear dependence of energy shift on position yielded a total reduction of the toroidal background by a factor of 3.6 at $E = 1$ eV. As the only drawback of the weaker expansion, the transverse temperature (3.1) of the electron beam went up to ≈ 30 meV, but the total resolution ΔE decreased only by a factor of ≈ 2 at the interesting energies, because it also depends on the longitudinal temperature which is determined by the cathode voltage.

The data acquisition and analysis were almost identical to the measurement with the wider electron beam: the measurement of the stored ion current and the BPM rate was omitted, and the reference energy in the wobbling scheme was replaced by an additional cooling step in most measurement runs. Therefore R_D^{ref} was not available as a normalization signal, so that the rate of coincident H+D fragments measured in the cooling steps was used, which is also proportional to the ion current after sufficiently long electron cooling.

$$I_{ion} = \zeta' R_{H+D}^{cool} \tag{4.15}$$

In addition, because of the higher transverse electron temperature, the H+D rate at cooling is less susceptible to the velocity spread of the ions than in the measurement with the wide beam. At the high electron density, the applied precooling phase of 5 s was found to be sufficient by examining the measured rate coefficient as a function of storage time, so that no cuts on the electron energy had to be defined. However, the sometimes slow operation of the protecting shutter caused a loss of fragments especially at high relative energies, where the kinetic energy release and thus the fragment distance is large. This required a weak cut on the data by ignoring all particle counts accumulated in the first two seconds after the precooling phase, and also in the last two seconds before each new injection.

The calibration constant ζ' was determined by matching the obtained rate coefficient to the one from the wide-beam measurement at energies of $8 - 25$ eV, where differences in the energy resolution and the subtraction of the toroid background are least important. The measured rate coefficient was then determined by

$$\alpha_{DR}(E) = \frac{qef_{TSR}}{\zeta' n_e} \cdot \frac{L_{TSR}}{L_{EC}} \cdot \frac{\left\langle R_{H+D}^{meas}(E) \right\rangle}{\left\langle R_{H+D}^{cool}(E) \right\rangle} \tag{4.16}$$

where no subtraction of background from residual gas was needed as with the wide electron beam, because the higher electron density directly improved the ratio of DR to residual gas-induced reactions along the electron cooler, by approximately one order of magnitude. Fig-

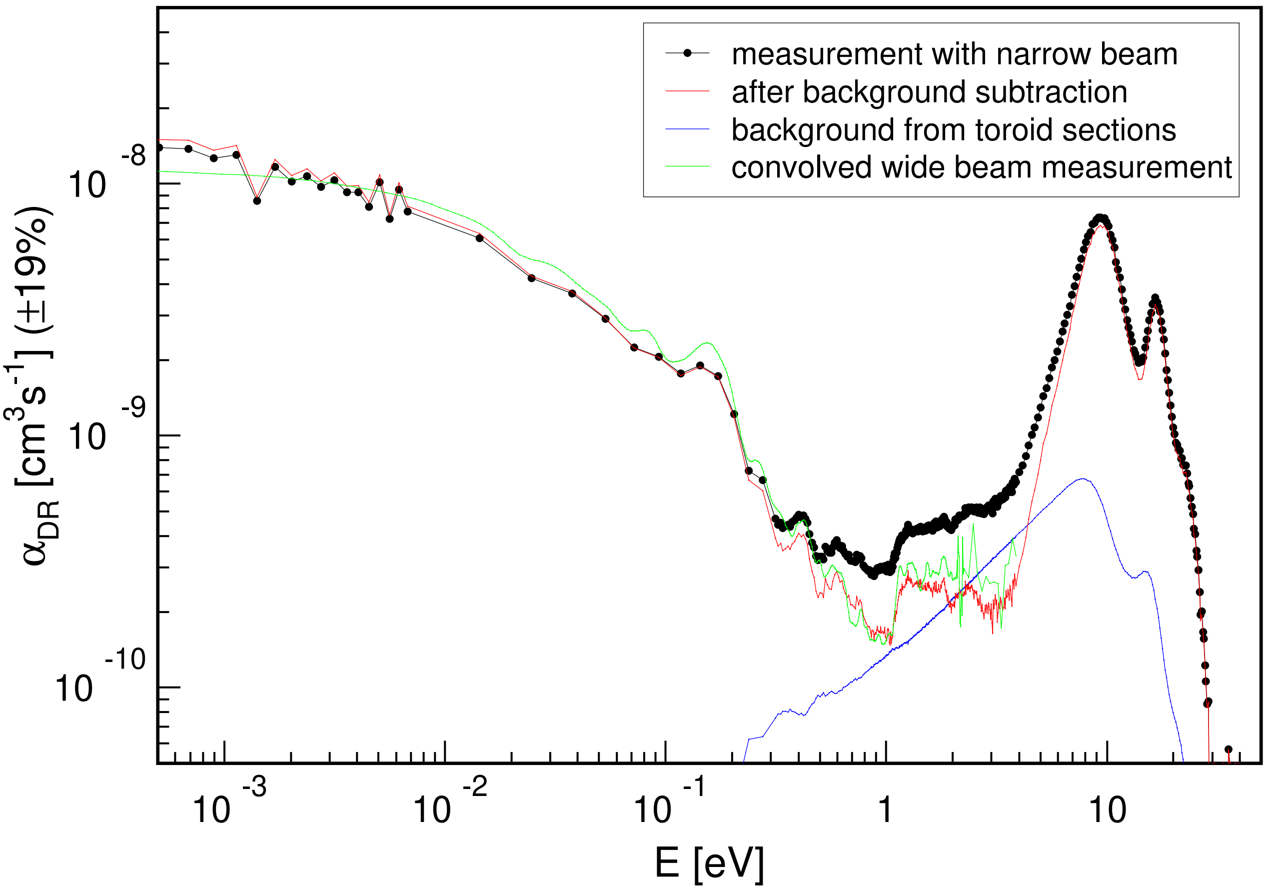

Fig. 4.6: *Rate coefficient for dissociative recombination of HD$^+$, measured with a narrow electron beam. Black: measured data; blue: calculated background from the toroid sections; red: background subtracted data; green: background subtracted data from the measurement with the wide electron beam, convoluted with the expected electron velocity distribution in the narrow beam.*

ure 4.6 shows the measured rate coefficient over the whole energy range (black), together with the background from the toroid sections (blue) and the background subtracted rate coefficient (red). For comparison, the green curve shows the background subtracted results from the measurement with the wider electron beam, which have been convoluted with the electron velocity distribution calculated for the narrow beam [63] for $E < 2$ eV. The difference of approximately $5 \cdot 10^{-11}$ cm^{3}s^{-1} between both (background subtacted) measurements at $1-4$ eV is interpreted as the systematical error in the calculation of the magnitude of the toroid background in the wide-beam measurement ($5 \cdot 10^{-10}$ cm^{3}s^{-1}), which is equal to a relative error of $\approx 10\%$. In the background subtracted rate coefficent, this translates to the already mentioned error of $5 \cdot 10^{-11}$ cm^{3}s^{-1} or 17% in case of the wide beam, and $2 \cdot 10^{-11}$ cm^{3}s^{-1} or 8% for the narrow beam.

Apart from these deviations, both measurements are in good agreement over the whole energy scale. Small deviations at low energies probably arise from systematic errors in the convolution of the wide-beam measurement to the different electron temperatures in the narrow beam. Since the energy resolution and the statistical sample at $E > 0.3$ eV favour the wide-beam measurement, but the narrow beam yields more precise results for higher energies, both measurements are combined in the next chapter, to a single spectrum of α_{DR} (Fig. 4.8) obtained by taking the wide-beam data for energies below and the narrow beam data above this threshold.

DE of HD$^+$

The rate coefficient for dissociative excitation of HD$^+$ is obtained as a by-product in the discussed measurements on DR. Since in both cases the rate of neutral H fragments could not be measured (because of electronic noise in the ADC spectrum, see Fig. 4.2), only the dissociation channel into a neutral D and an H$^+$ fragment is considered. The total DE rate coefficient is approximately twice the value for the D channel, since both neutral species are produced with about the same ratio over the whole energy range.

For both measurements, the rate coefficient is again obtained with different modes of normalization to the stored ion current, as explained in the last section. The resulting DE rate coefficients

$$\alpha_{DE}(E) = \frac{qef_{TSR}}{n_e} \cdot \frac{L_{TSR}}{L_{EC}} \cdot \frac{\langle R_D^{meas}(E) \rangle}{\langle I_{ion} \rangle} \tag{4.17}$$

from the measurements with the wide and the narrow electron beam (before background subtraction) are shown black in Fig. 4.7.

Compared to DR, the subtraction of the background from residual gas collisions (which is orders of magnitude stronger than for H+D pairs) has to be done differently, since the DE rate coefficient vanishes for $E < 2.67$ eV (the dissociation threshold of HD$^+$). Correspondingly, R_D^{cool} consists mostly of residual gas induced events, but is also affected by the energy shift in the toroid sections. Therefore, the toroid-background R_{toro}^0 at $E = 0$ eV must be subtracted from R_D^{cool} in order to obtain the contribution from residual gas collisions alone, but its magnitude is not known a priori. Because of this coupling between the backgrounds, both were determined simultaneously in a fit procedure, where R_{toro}^0 was varied as an independent parameter to minimize the χ^2 between the measured rate coefficient (after subtraction of both backgrounds) and its expected value of zero for $E = 0 - 2$ eV. The resulting, decoupled backgrounds from collisions with residual gas

$$\alpha_{res.gas}(E) = \frac{qef_{TSR}}{n_e} \cdot \frac{L_{TSR}}{L_{EC}} \cdot \frac{\left\langle R_D^{cool}(E) - R_{toro}^0 \right\rangle}{\langle I_{ion} \rangle} \tag{4.18}$$

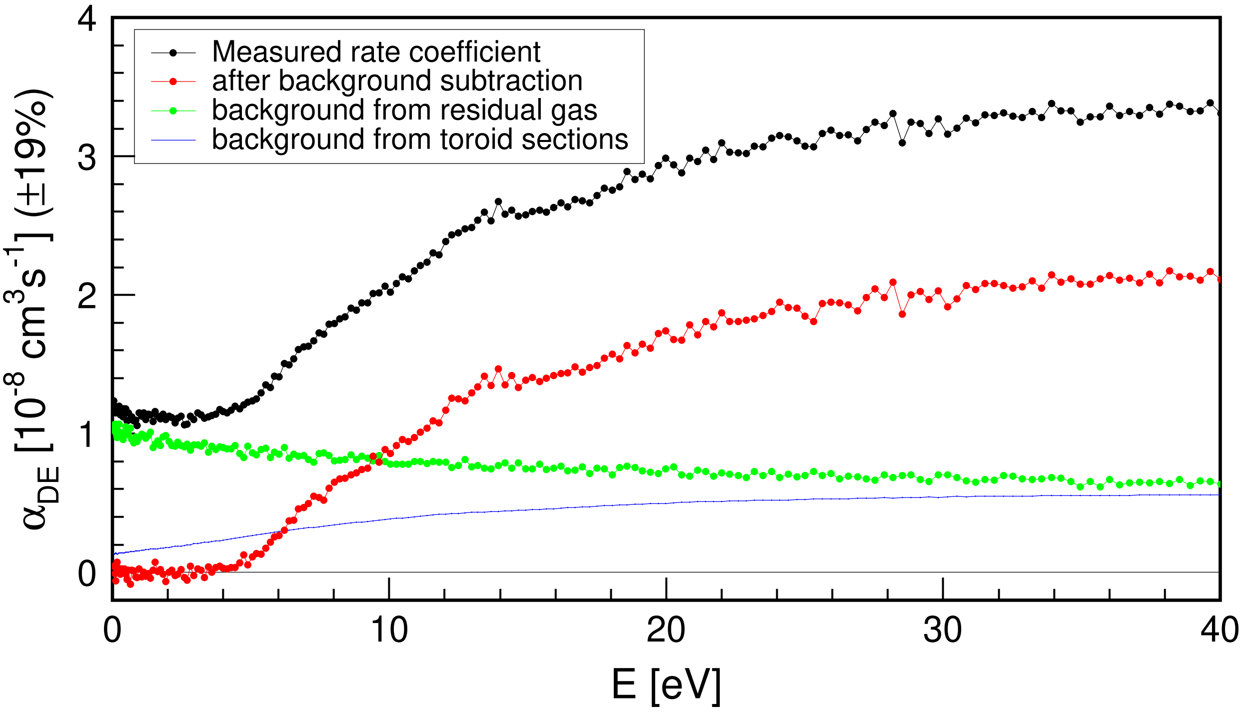

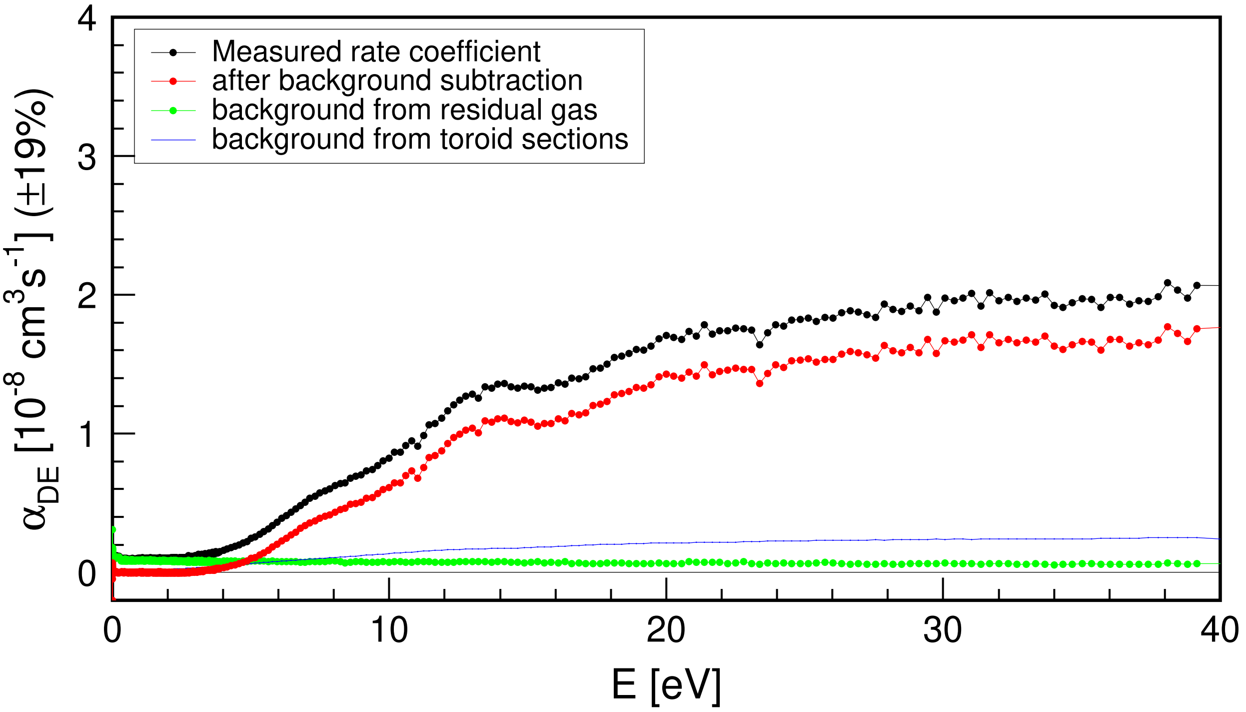

Fig. 4.7: *DE rate coefficients for the* $H^+ + D$*-channel. Measurement before background subtraction (black), contributions from residual gas collisions (green) and toroid sections (blue), background subtracted rate coefficient (red).* **Top:** *wide electron beam;* **Bottom:** *narrow electron beam.*

and from the toroid sections are shown as the green and blue curves, respectively, in Fig. 4.7, as well as α_{DE} after subtraction of both backgrounds (red).

The background subtracted rate coefficient obtained with the wide electron beam is larger than with the narrow beam by $\approx$20%, with only a weak dependence on energy. This is attributed to problems in calculating the background from the toroid sections: Already at $E=12$ eV in the colinear part of the electron cooler, the shift in the toroid sections exceeds the high end of the measured energy scale so that the background had to be estimated by assuming α_{DE} to stay constant for higher E, which seems to lead to an underestimation of the toroid background by roughly 35%.

Because these two measurements do not provide new insights into dissociative excitation, only the most important features in the rate coefficient spectra in Fig. 4.7 shall be explained briefly, following the interpretation in [23]: At energies around $2.5-3$ eV, the background subtracted DE rate coefficent of both measurements shows the slow onset which is typical for the indirect mechanism involving the $(2p\sigma_u)^2$ state of neutral HD$^+$ (best seen in the narrow beam measurment, because of the larger statistical sample). Above ≈ 8 eV, the direct DE via the ionic $2p\sigma_u$ state becomes important, causing the broad peak visible at $E \approx 13$ eV, while at still higher energy the excitation of the $2p\pi_u$ ionic state is dominant. As discussed before, the deviations between both measurements are attributed to a systematical error in the calculation and subtraction of the toroidal background.

4.4 Measured Rate Coefficient

Figure 4.8 shows the rate coefficient for dissociative recombination of HD$^+$ (black dots), from combining the two background subtracted measurements discussed in the last chapter at $E=300$ meV. It is to be compared with the red curve, which represents a recent calculation of σ_{DR} [64], which has been convolved with the velocity distribution in the electron beam to yield a rate coefficient.

At energies below 3 eV, the calculation used an MQDT approach, in which the interaction between the ionic (initial state and DE final states) and atomic continuum states (DR final states) was treated by a perturbation method, allowing either direct transitions between two ionic states (first order) or indirect ones involving an intermediate atomic state (second order). The difference to most former treatments is the inclusion of rotational states, not only by assuming an initial rotational distribution (according to 300 K) in the ion beam, but also by taking them into account as possible capture states for the indirect DR mechanism. First-order calculations including rotational states have been done in [45], and an iterative method was presented in [65], while the presented calculation relies on second-order perturbation theory to reduce the computational effort. At energies above 4 eV, only the direct recombination into states belonging to the Q1 series of HD has been taken into account; in particular, electron capture into states of the Q2 series has been neglected, which explains the sharp drop of the calculated α_{DR} at $E > 13$ eV.

In the rate coefficient at very low energies (< 1 eV), the effect of indirect recombination is visible in the so-called "window-resonances" at energies below the dissociation threshold of HD$^+$, which mostly appear as narrow dips in the spectrum. The overall agreement with the absolute scale of the measured rate coefficient is good for energies below 200 meV. For some window resonances (20 and 100 meV), even the depth is reproduced remarkably well. However, at $1 - 4$ eV the theoretical rate coefficient is larger than the measured one by a factor of 2.5. Especially the start of the plateau in the theoretical rate coefficient beginning at around 0.8 eV is in disagreement with the experiment, and gives rise for a closer look at intermediate energies.

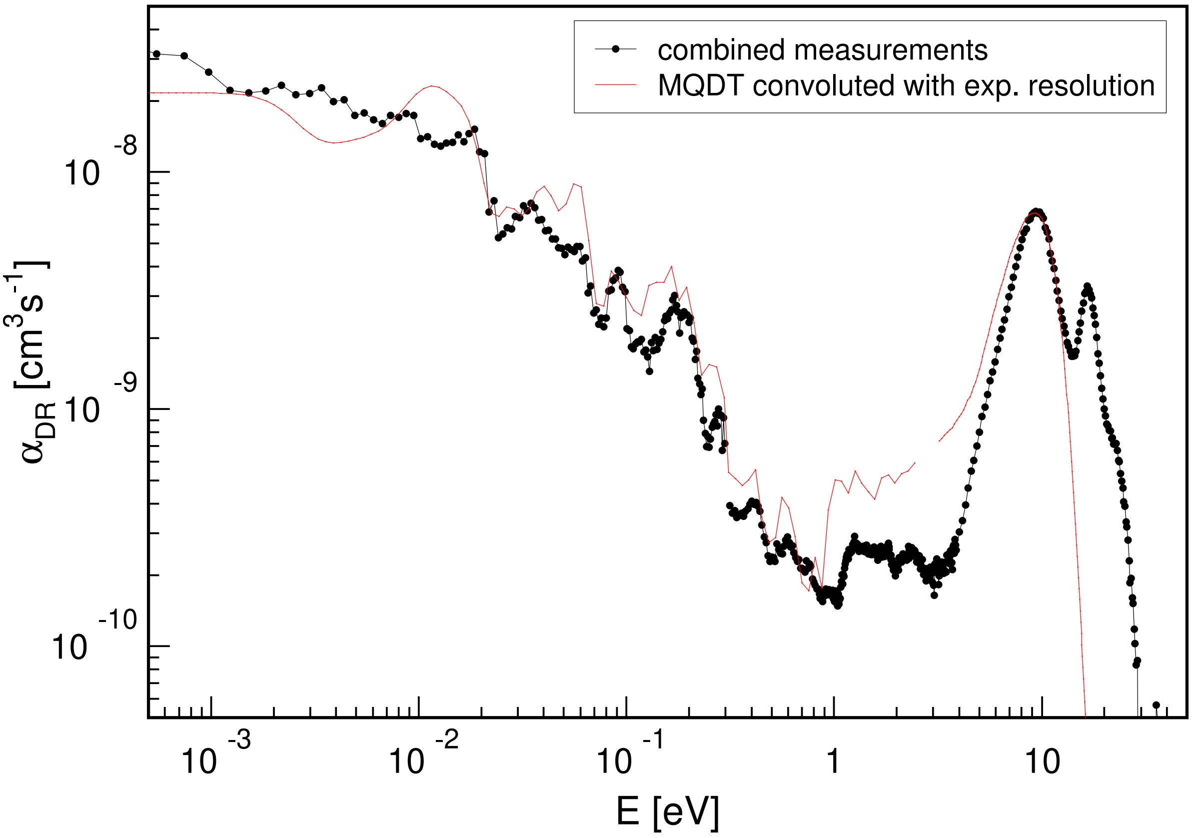

Fig. 4.8: *Rate coefficient for dissociative recombination. Black: merged spectrum from the background subtracted measurements with the wide and the narrow electron beam. Red: Calculation from [64], convolved with the experimental electron velocity distribution.*

There, it is more interesting to compare the measured rate coefficient above 1 eV to the energies corresponding to the opening of new final states in the dissociation step, rather than with the position of capture states for the indirect mechanism. This is done in Fig. 4.9, which shows a magnification of the measured and theoretical rate coefficient, along with the threshold energies at which the fragment states H(1s) + D(nl) with principal quantum numbers of $n \geq 3$ become available. Also plotted is the threshold energy for dissociative recombination into ion pairs ($H^+ + D^-$), which was observed in [66]. At the opening of each of the final states with $n = 3 - 6$, the measured rate coefficient shows a steep rise, whereas a drop is visible in coincidence with the opening of the ion pair channel.

Since the population of final states in dissociative recombination at these energies is determined only after the electron capture, by redistribution of quantum-mechanical flux at the avoided crossings between states of the neutral molecule [22], it is not possible to understand these steps

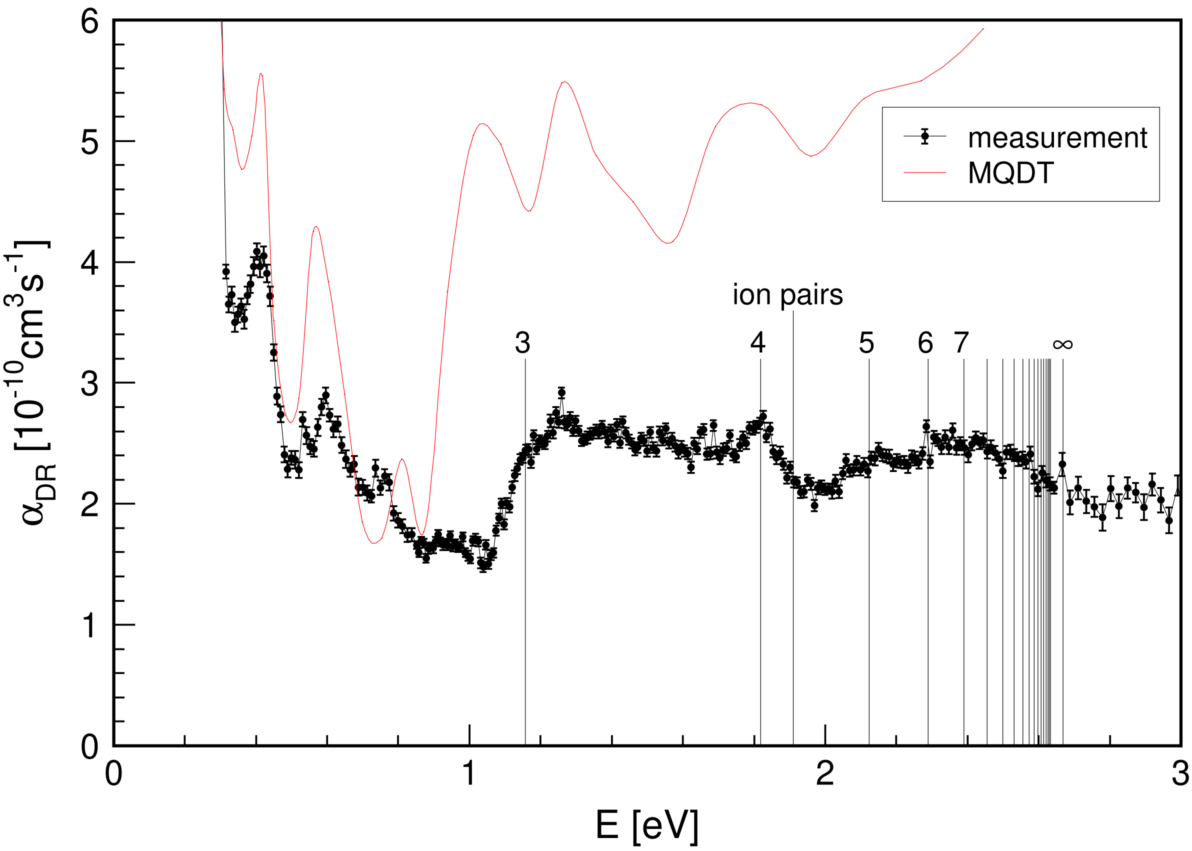

Fig. 4.9: *Coincidences between steps in the DR rate coefficient and the opening of new final states. The lines and numbers represent the threshold electron energy needed for the production of the fragment states H(1s) + D(nl) with principal quantum numbers of $n \geq 3$. Also shown is the threshold energy for the production of ion pairs, which could not be detected.*

as an increase in the electron capture rate at the opening of new reaction channels. Instead, the observed threshold behaviour is attributed to the survival factor in eq. (2.18), by taking into account the effects of closed dissociation channels: For example, at an electron energy below the $n=3$ threshold, the fragment state with $n=2$ is the only one populated, but this does not mean that there are no transitions at avoided crossing with the dissociating states to higher quantum numbers: within the semiclassical picture presented in Chapter 2.1, such transitions are possible as soon as the electron energy exceeds the potential *minimum* of the other state. In this case, all probability flux transmitted into the closed state is reflected by its outer potential walls, so that the direction of the nuclear motion is inverted towards smaller R for a fraction of events given by the Landau-Zener transition probability into the closed state. Thus, the internuclear separation may once again go below the stabilization point R_s, where autoionization is important as a stabilization mechanism competing with dissociation, which significantly decreases the DR rate coefficient. On the contrary, if energy is raised above the threshold for $n=3$, an additional state becomes available for dissociation, and much less flux is reflected back towards small internuclear separations, and less autoionization processes can take place, effectively increasing the probability for dissociation.

This interpretation is backed up by the multistate curve-crossing (MSCC) calculation [42, 3] from Chapter 2.2.3, which was improved to obtain the survival factor as the branching ratio into an additional autoionization channel. In contrast to the case of branching ratios of the dissociative states, which are almost unaffected by energetically forbidden states and which were obtained in a single-pass calculation within the explained semiclassical framework, such closed channels are taken into account by assuming that all flux diverted into them is reflected at the outer potential walls. Additionally, the distribution algorithm is iterated until all flux has left the system either by one of the dissociation channels, which correspond to fragment states with quantum numbers up to $n=6$, or by autoionization below R_s. The ion pair production is considered as a loss channel, because the corresponding fragments could not be detected in the experiment. Since this calculation does not aim on the absolute scale of the rate coefficient, the resulting survival factor is multiplied with a $1/E$ capture cross section in analogy to (2.18), folded with the relative velocity distribution, and then scaled to match the measured rate coefficient at energies of $0.5 - 2.4$ eV (the upper limit representing the threshold for channels with $n>7$, which were not taken into account).

The results are compared to the experimental data in Fig. 4.10, which shows an excellent agreement not only with the present rate coefficient data, but also with the previous experimental and theoretical results for the branching ratios into the neutral fragment states (Fig. 2.3). Especially the reproduction of the structure in the rate coefficient at around 1.9 eV is interesting, since there the $n=4$ final state is competing with the ion pair channel: First, at 1.8 eV, the dissociation into neutral fragments H(1s) + D(4l) becomes possible, leading to an increase in α_{DR}. For little higher energy (1.9 eV) the ion pair channel opens, which is shown as loss channel at negative rate coefficients in Fig. 4.10, because the fragments were not detected. At this point, the MSCC model predicts that the measured rate coefficient for DR into *neutral* fragments actually drops, because the increasing survival factor does not compensate for the relatively large branching ratio into ion pairs, which is in complete agreement with observation. Also the overall drop beginning at around 2.5 eV, slightly below the series limit, is qualitatively explained by effective loss channels: Here, the quantum number of the excited fragment can be high enough for the fragment to be ionized by the motional electric field in the TSR dipole magnets, leading to a misinterpretation of the remaining ground state fragment as coming from DE (which is not visible as a backgroud in the DE rate coefficient only because α_{DR} is too low at this energy).

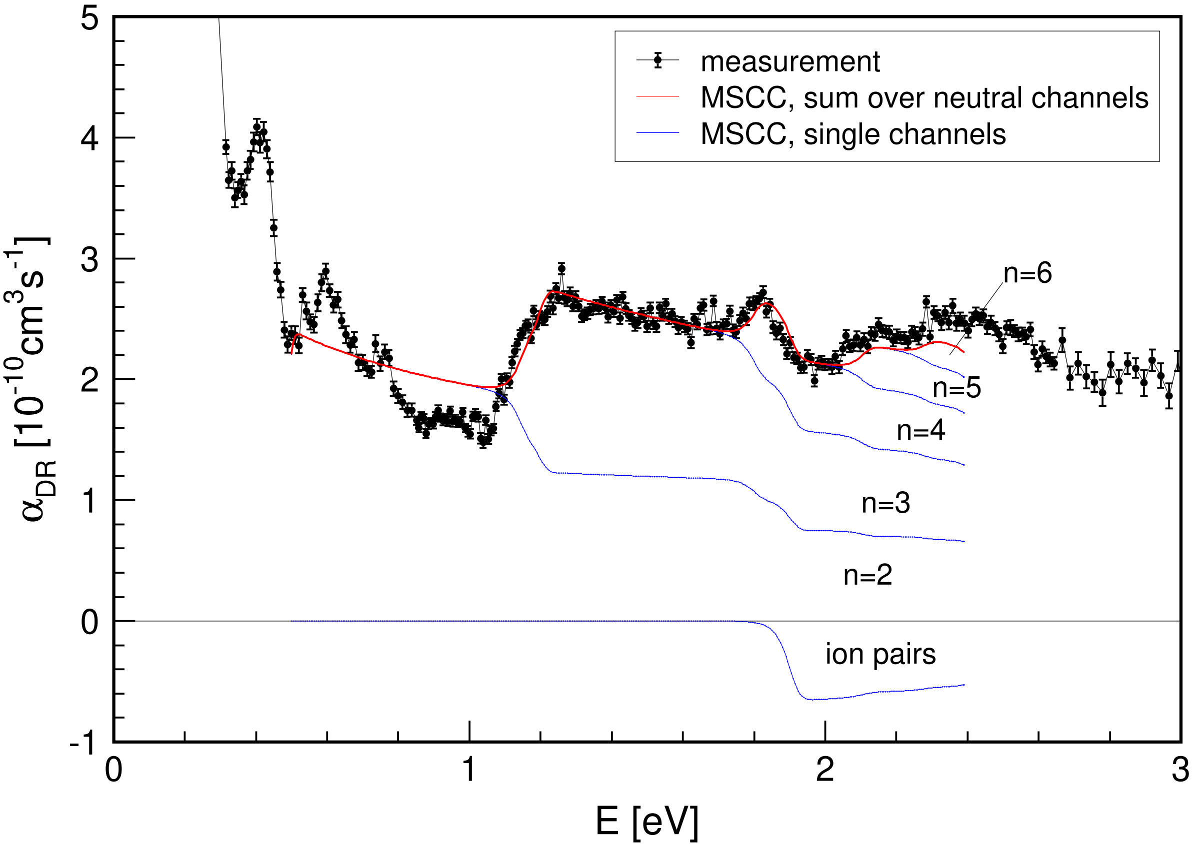

Fig. 4.10: *Comparison between measurement (black) and the multistate-curve crossing model, which explains the structure in α_{DR} by autoionization processes during dissociation. Red: total MSCC rate coefficient, folded with experimental resolution; Blue: contribution from single reaction channels to the MSCC result.*

This proves that indeed a previously unknown competition between autoionization and dissociation has been observed in DR, which mediates an influence of the final state distribution on the total rate coefficient or cross section. Still, the two-step model of DR can be kept up, but the calculation of the survival factor in the separated cross section (2.18) becomes more complicated, since the simple model of integrating the autoionization probability between the capture point R_c to the stabilization point R_s has to be replaced at least with a semiclassical treatment allowing the reflection of flux by closed channels. In principle it should be possible to include this effect in MQDT calculations, by allowing higher-order interaction between the neutral states themselves and also with the ionic states (which would also yield branching ratios in addition to the cross section). But since the above MSCC model showed a slow convergence (needing about 30 iterations), it might be more effective to treat the branching ratios as additional input to the calculations, or to use different models such as time-dependent wave packet calculations.

5. Inelastic Collisions of HD^+ with Electrons

The following sections describe the measurement of the rate coefficient for vibrational excitation of HD^+ by collisions with slow electrons, which was the first time that this process has been ovserved in a storage ring.

Because the experiment was not designed to measure the vibrational excitation of HD^+ by electrons, but to observe interference in the branching ratios for the $2s$ and $2p$ fragments states of dissociative recombination, the original idea will first be outlined, allowing to explain the experimental setup in this context before presenting the analysis of the measured data. Thus, the interpretation of the experiment and the comparison with theory is left to Chapter 5.4.

5.1 Design of the Laser Dissociation Experiment

At relative energies between 0 and 1.15 eV, only the fragment states $\mathrm{H}(1s)+\mathrm{D}(2l)$ and $\mathrm{H}(2l)+\mathrm{D}(1s)$ are populated in the DR of HD^+, because of energy conservation. Only above 1.15 eV, fragments with $n \geq 3$ may be produced. The $2p$ substate decays to the ground state within $\tau_{2p}=1.6$ ns [67], while the transition from $2s$ is forbidden by dipole selection rules. This state decays mainly by emission of two photons at a lifetime of $\tau_{2s}=0.12$ s [67], which is treated as being infinite.

To estimate the relative population of $2s$ and $2p$ states in the fragment beam for given branching ratios b_{2s} and b_{2p} along the electron cooler, it is assumed that ions enter the collinear section at a constant rate R_{ion} and with the velocity v_{ion}. At any position z (measured from the beginning of the collinear section, in the direction of the ion movement), the respective particle rates are assumed to be $R_{2s}(z)$ and $R_{2p}(z)$ (both $\ll R_{ion}$). At $z+dz=z+v_{ion}dt$, a fraction pdt of the ions will additionally have undergone DR, increasing the fragment rates by $R_{ion}b_{2s}pdt$ and $R_{ion}b_{2p}pdt$ respectively (p being the DR probability of a single ion per unit time), while a fraction dt/τ_{2p} of the $2p$-fragments will have decayed to the ground state.

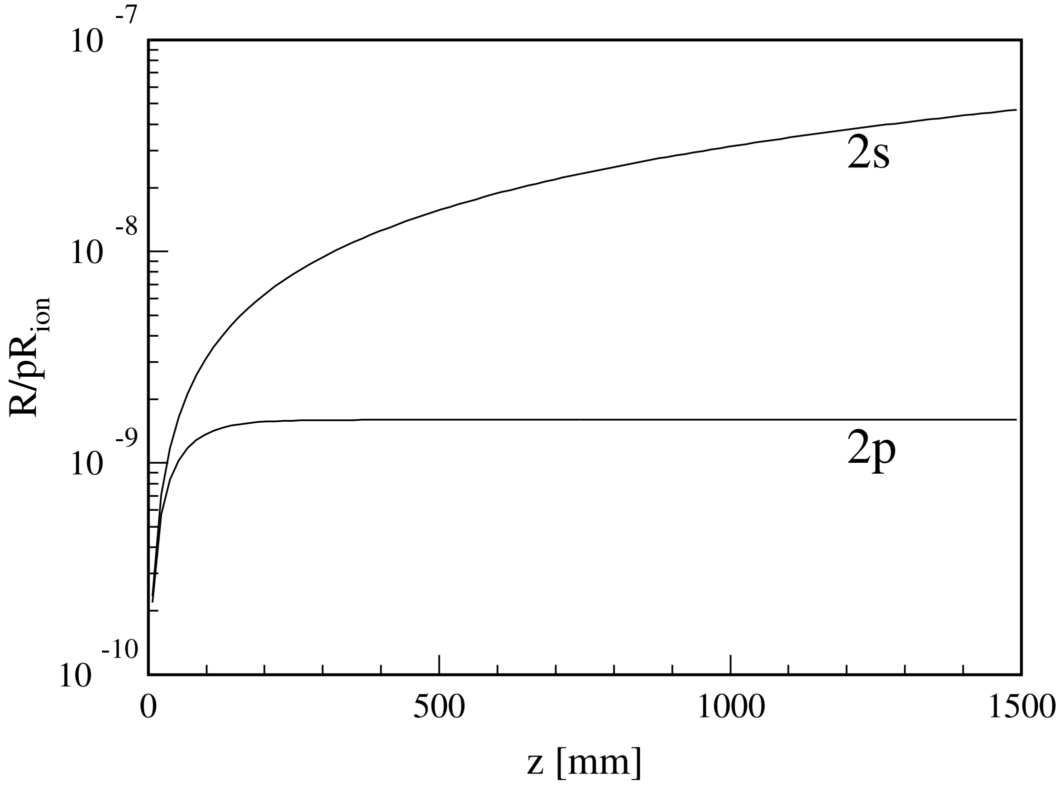

Fig. 5.1: *Normalized fragment rates* $R_{2s,2p}/pR_{ion}$, *as a function of position along the colinear section of the electron cooler. Calculated from (5.1) for the experimental conditions* ($E_{ion} = 15.876$ *MeV*, $v_{ion}/c = 0.1063$), *and assuming that* $b_{2s} = b_{2p}$.

The net increase in the fragment rates for each state is given by the rate equations

$$\begin{aligned} dR_{2s} &= pR_{ion}b_{2s}dz/v_{ion} \\ dR_{2p} &= pR_{ion}b_{2p}dz/v_{ion} - R_{2p}dz/v_{ion}\tau_{2p} \end{aligned} \tag{5.1}$$

which are satisfied by

$$\begin{aligned} R_{2s}(z) &= pR_{ion}b_{2s}z/v_{ion} \\ R_{2p}(z) &= pR_{ion}b_{2p}\tau_{2p}\left(1 - e^{-z/v_{ion}\tau_{2p}}\right) \end{aligned} \tag{5.2}$$

For the case of equal branching ratios $b_{2s} = b_{2p}$, the normalized fragment rates $R_{2s,2p}/(pR_{ion})$ are plotted in Fig. 5.1 as a function of z.

As the fragments exit the collinear section they have to pass the bending region, where electrons and ions are de-merged, and the magnetic guidance field B_2 for the electrons is no longer parallel to the ion velocity (see Chapter 3.3). In the comoving frame of reference, the ions therefore experience a transverse electrical field

$$E_\perp = \frac{1}{\sqrt{1-\frac{v_{ion}^2}{c^2}}}\, v_{ion} B_2 \sin\alpha \tag{5.3}$$

where α is the angle between the ion velocity and the magnetic guidance field, which is equal to the angle (3.5) with the electron trajectories. With $B_2 = 0.02$ T and $v_{ion}/c \approx 0.1$, $E_\perp$ reached ≈ 100 kV/m at the end of the bending region, by far exceeding the field strength of 47.5 kV/m [68] necessary for Stark mixing of the metastable $2s$ with the rapidly decaying $2p$ state. The $2s$ state is effectively quenched and all fragments leave the electron cooler as ground state atoms, making it impossible to detect the $2s$ or $2p$ fragment state populations outside the electron cooler[1].

Therefore it was planned to measure the neutral fragment rate with the MSP detector, and to photoionize the $2s$ fragments inside the electron cooler with a pulsed UV laser beam. The beam of the dye laser (Chapter 3.5) was directed through the slit in the MSP towards the electron cooler, allowing an overlap with the fragment beam (and also the ions) along the whole interaction region (Fig. 5.2). Because usually the ion orbit inside the electron cooler is slightly shifted and also tilted against the TSR axis, the fragment beam and the laser do not overlap with the ions outside the electron cooler, making it easier to adjust scraper 1 without losing the stored ions.

Since the MSP does not provide multihit-resolution below several 10 ns, it cannot distinguish between both DR fragments hitting or only one; so it was also necessary to prevent either the H or the D fragment from reaching the detector, while letting the other one pass with sufficient velocity for detection. That was achieved by putting a thin quartz plate (Infrasil, diameter 25 mm, thickness 0.27 mm) into the fragment beam. The plate is transparent for the laser light and by its thickness lets the D fragments pass, but blocks all H atoms. Since the diameter of the fragment beam (≈ 3 mm at the detector, caused by the kinetic energy release in the DR) was smaller than the size of the MSP-slit, the quartz plate was mounted 150 mm in front of the detector, instead of the shutter in the detector chamber (Fig. 3.1 and 5.2). That allowed one to profit from the scattering of the D fragments in the plate, by inflating the beam diameter to $15-20$ mm at the detector, so that only 30 % of the fragments were lost by passing through the slit in the MSP.

Without laser light, the detector would show a constant rate R_0 of fragments coming from DR (the background from collisions between molecular ions and residual gas could be measured and subtracted). At every laser shot, D fragments in the $2s$ state would be photoionized and

---

[1] The difference between the kinetic energy release by DR into these states is several oders of magnitude smaller than the resolution of the TSR imaging detector.

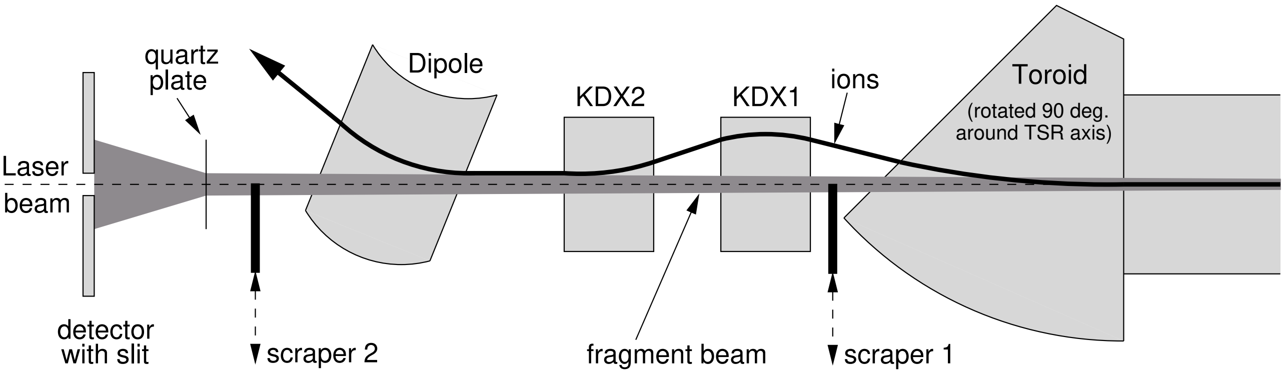

Fig. 5.2: *Overlap of laser (dashed line), ions (thick line) and fragment beam (grey cone) inside and after the electron cooler (not drawn to scale). The magnets KDX1 and KDX2 (which usually compensate the deflection by the toroid magnets) were adjusted such that outside the electron cooler, the ion beam was quickly removed from the laser. The detector and the quartz plate are also shown, as well as the scapers.*

deflected by a TSR dipole, decreasing the intensity of the fragment beam for a short time. The shape $R(t)$ of this "dip" reflects the time-of-flight distribution of the missing fragments, which is given by the convolution of the $2s$-curve in Fig. 5.1 (as a function of $t = x/v_{ion}$) with the length τ_{laser} of the laser pulses and the time resolution of the MSP. However, under the assumption that all $2s$ fragments are photoionized by the laser, and that the small number of particles remaining in the $2p$ state can be neglected, the normalized integral over the dip shape is directly equal to the branching ratio b_{2s}:

$$b_{2s} = 2 \frac{\frac{\tau_{sig}}{\tau_{bgr}} \int_{\tau_{bgr}} R_0 dt - \int_{\tau_{sig}} R(t) dt}{\frac{\tau_{sig}}{\tau_{bgr}} \int_{\tau_{bgr}} R_0 dt} \tag{5.4}$$

where τ_{sig} is the length of a time interval containing the whole dip, and τ_{bgr} of an interval over which the background rate is integrated; $R_0 = \lim_{t \to \pm\infty} R(t)$ is the fragment rate outside the dip. The factor of 2 in the equation reflects the fact that even for $b_{2s} = 1$, only half of the deuterium fragments will be in the $2s$ state, because the other half originates from DR events where $\mathrm{D}(1s) + \mathrm{H}(2s)$ was produced instead.

Under the conditions of the experiment, the dip was expected to be distributed over ≈ 50 ns (the time-of-flight in the electron cooler), so that it is broadened by a factor of five compared to the 10 ns interaction time with the laser, and flattened by the same ratio. In consequence, $R(t)$ would deviate from R_0 by only 10%, so that the measured value of b_{2s} would be affected strongly by statistical fluctuations of the DR rate. An additional systematic error could be induced by the selection of the integration limits in (5.4) and the subtraction of background from residual gas collisions. In a measurement of the $2s$ branching ratio as a function of relative energy, this would show up as a global shift and scaling in the measured branching ratio, but its energy-dependence and especially the positions of maxima and minima are not affected. Therefore, comparison to the interference pattern predicted by theory (Fig. 2.4) would still be possible on a relative scale.

To observe significant structure in $b_{2s}(E)$, at least the region $E = 0 - 0.1$ eV was to be covered, where also the DR cross section (and thus the fragment rate) is high enough to measure with statistical errors below 20 %. If possible, the measurement should have extended up to 1 eV to cover a full period of the interference effect, but at these energies the DR cross section is only $\approx 10^{-2}$ of its value at $E = 0$ eV, which seriously prolongs the time needed for accumulation of sufficient data.

5.2 Setup and Data Acquisition

At the given thickness of the quartz-plate (dictated by mechanical stability), the requirement to stop all H but no D fragments imposed both a lower and an upper limit on the ion energy. A value around 16 MeV was found to be optimal; 15.876 MeV were determined from the measured cathode voltage and collector current in the electron cooling mode ($E = 0$), using eq. (3.4). Since the DR fragments travel at the same velocity as the stored ions (0.1063 c), the fragment energies are ≈ 5.3 MeV for H, and ≈ 10.6 MeV for D. At these energies, the H fragments would be stopped after 211 μm of SiO_2, which is well inside the plate, while the D have twice the range and could pass through the plate to the detector, with still 1.7 MeV/u left [69].

The ionization threshold of the hydrogen $2s$ state is 3.400 eV or 364.6 nm (disregarding hyperfine structure), which because of the relativistic Doppler shift from the ion velocity transforms to a threshold wavelength of 405.7 nm in the laboratory frame. In the experiment, the wavelength was set to 380 nm (341.5 nm in the ion frame), where the dye “Polyphenyl 1” has its maximum quantum efficiency of 11% [70]. Although this dye turned out to be out of production, the dielectric mirrors for the light transfer to the TSR had already been bought at that time, so that the replacement dye (QUI, see Chapter 3.5) had to be operated also at 380 nm, despite having only $7 - 8\%$ quantum efficiency.

With the electronics setup, which is shown in Fig. 5.3, many scans of E over the range of $0 - 30$ eV have been done, distributed over several measurement runs of typically $1 - 4$ hours duration, with new injections into the TSR every 25 s.

The most important electronic component is the Multihit-TDC (time-to-digital-converter), a CAMAC module which measures the time difference between a start and up to 16 stop signals

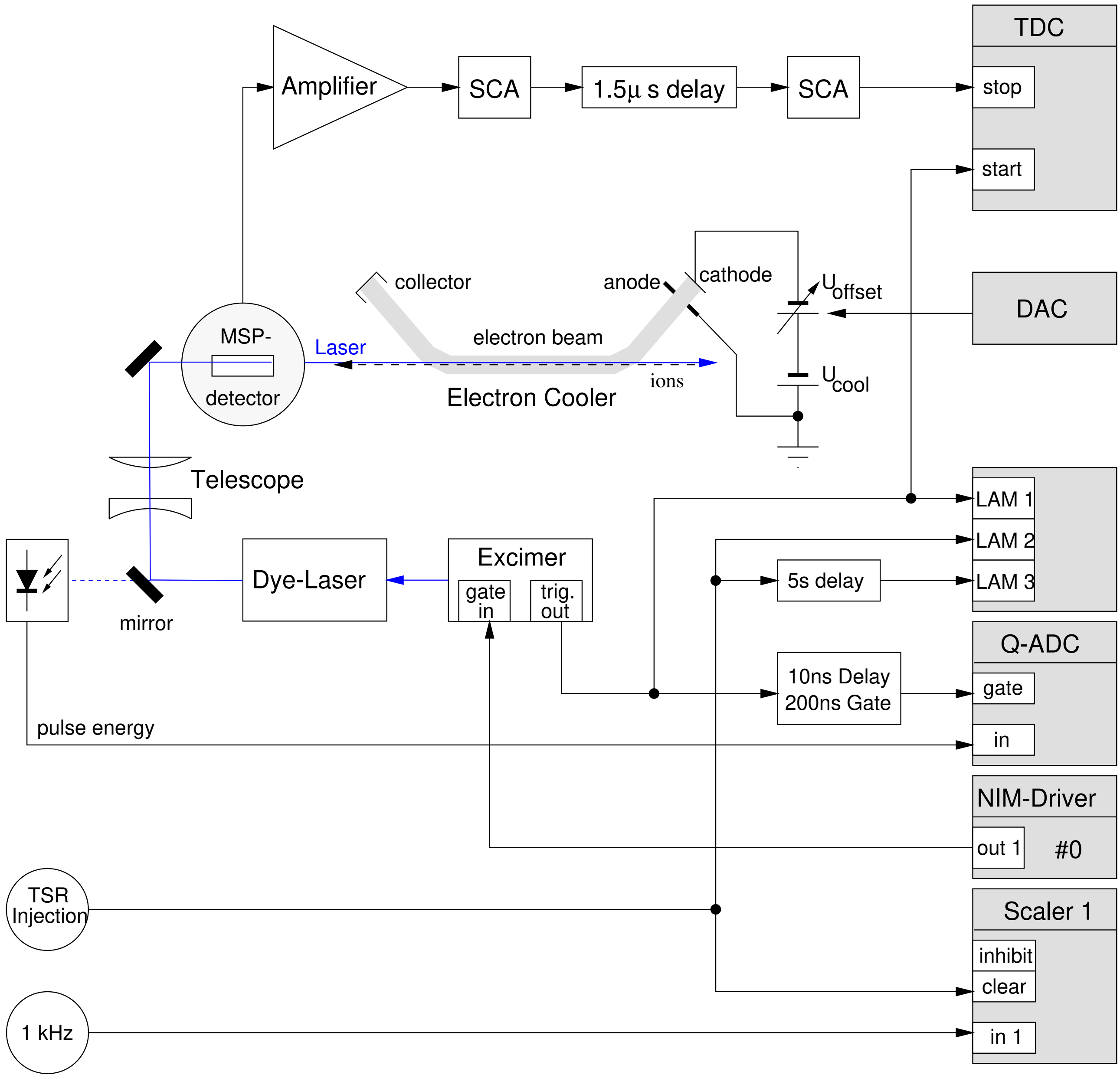

Fig. 5.3: *Electronics setup used in the measurement of the cross section of vibrationally inelastic collisions of HD$^+$ with electrons. Grey boxes: CAMAC modules; white boxes: NIM or standalone modules; white circles: input signals.*

with an accuracy of 1 ns, within a time window of 16 μs after the start. It was used to measure the fragment rate on the MSP as a function of the time elapsed since the laser shot, thus providing the time-dependence of the fragment rate during the photoionization-dip: The start signal was taken from the trigger output of the pulsed excimer laser, while the output of a single-channel-analyzer (SCA) working on the anode signal of the MSP detector served as the stop. The trigger-output of the excimer laser was also used to notify the TSR data acquisition system (Chapter 3.6) of each laser shot by generating a CAMAC LAM signal (LAM 1), which caused the software to read out the TDC as well as the Q-ADC and the scaler, which are both described further down.

To make sure that the stop signals always arrived after the start, the time needed for the light to reach the electron cooler, as well as for the fragments to arrive at the detector and for the detector signals to reach the TDC was compensated by delaying the SCA-output by 1.5 μs, using a long cable. After this delay, the signal had significantly lost in amplitude; it was refreshed by a second SCA before being fed into the TDC. Therefore, the time-spectrum produced by the TDC contained fragments arriving from 1 μs in advance of each laser shot, until 15 μs after it.

At each injection into the ring, the software was notified by a LAM signal (LAM 2), which started the transfer of previously measured data from the VME computer to the PC. In the meantime, the newly injected ion beam was phase-space cooled by the electron cooler (called precooling). The excimer laser was switched off during this time, by an anti-gate signal produced with a programmable output register (the NIM-driver). Five seconds after injection another LAM (3) was generated, indicating the end of the precooling mode. At this point, the software would switch on the excimer laser, which would then run freely at 200 Hz repetition rate until the next injection 20 s later. At every 10th laser shot, the adjustable HV power supply at the electron cooler (3.3) was switched either back or forth between cooling mode ($E = 0$ eV) and a measurement energy $E > 0$ eV, which was changed with each injection in order to obtain the TDC spectra as a function of E and of the storage time t_{inj}. To measure t_{inj}, a 1 kHz TTL-signal from a clock was fed into a scaler, which was read out with every laser shot and cleared only by the TSR injection signal; this way, the storage time at each laser shot is known with a precision of several ms (some unavoidable jitter was caused in the module readout by the software).

In addition, the energy contained in every laser pulse was measured with a fast photodiode, which operated on the strongly attenuated light transmitted by the first folding mirror after the dye laser. Additional opaque glass filters were used to attenuate the light further, so that the diode would generate a charge signal depending linearly on the energy of the shots. This charge was accumulated by a Q-ADC, which was read out after every laser shot. The ADC needed an additional gate signal to control its active time window, which was generated by a sequence of two timers, coupled to a trigger output of the excimer laser, and which were adjusted to 10 ns delay and 200 ns gate.

5.3 Results of the Laser Dissociation Experiment

At the beginning of the experiment, it was checked that the electronics setup was working and that all conditions necessary for the experiment were met: The energy of the laser shots, and also the profile of the laser beam inside the electron cooler was sufficient for photoionizing a significant fraction of the D(2s) fragments; the focus of the laser beam was checked to be some meters behind the beam dump on the far side of the used TSR section, thus ensuring almost constant beam diameter inside the electron cooler. In a test measurement done some months in advance of the actual experiment, also the thickness of the employed quartz plate was proven to be appropriate for stopping the light hydrogen fragments, but letting the deuterium pass with sufficient energy for detection by the MSP. From other experiments, it is known that after 400 ms, the vibrational degree of freedom of the ions is in thermal equilibrium with the surroundings at 300 K. Therefore, after the precooling phase of 5 s, only the vibrational ground state of the ions was expected to be populated, so that from the calculated cross sections (Fig. 2.26) photodissociation of the stored ions was ruled out as a possible background process.
Surprisingly, a strong peak was found on top of the constant background rate from DR in the TDC spectrum (Fig. 5.4), which prevented the observation of the $2s/2p$ interference by monitoring the dip in R_D, indicating that the experiment was sensitive to a different effect. Sensitivity of the MSP detector to the laser light was ruled out as a possible source of this peak by comparison with a measurement run without ions, as was electronic cross-talk between the discharge in the excimer and the MSP/TDC combination. Actually, optical cross-talk by laser light falling onto the MSP can be seen in the spectrum of some (but not all) runs as a second, smaller peak before the strong one.

The time difference of 160 ns between the cross-talk and the fragment peak is smaller than the expected time of 21 ns for the light to travel from the MSP to the center of the electron cooler (6.5 m distance), plus the 216 ns needed by the illuminated fragments to make the way back to the MSP. This shows that the cross-talk does not originate from the first passage of light through the MSP slit, but is caused by light which is reflected back at the MSP by the exit window of the TSR. In this case, the light has to travel a total of $\approx$25 m (equalling 83 ns) before being detected by the MSP, thus preceding the fragments by only 154 ns, which is in good agreement with observation. In addition, its width of 90 ns (FWHM) indicates that not

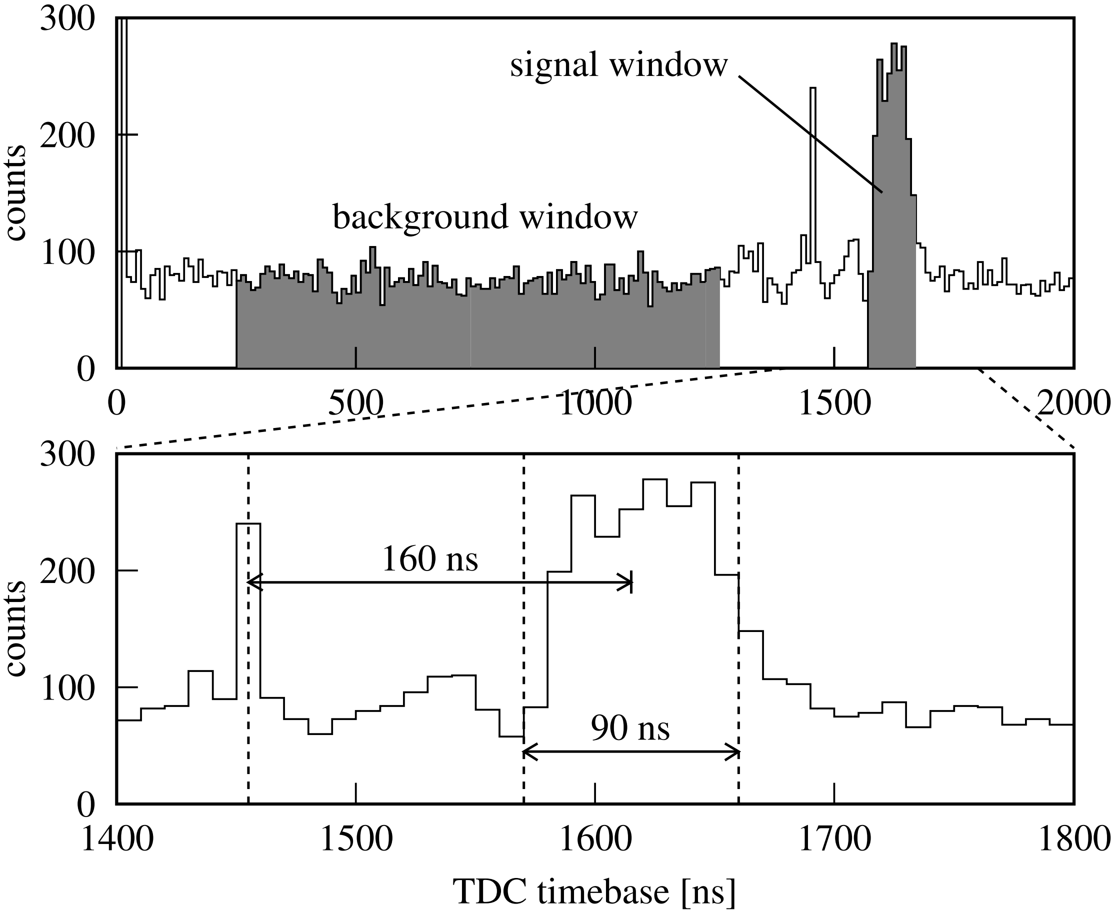

Fig. 5.4: *Increase in fragment rate in coincidence with the laser shots. Upper plot: selected windows for integration over the fragment rate in the peak (signal) and the flat part (background) of the spectrum. Lower plot: magnification of the fragment peak, showing the narrow preceding peak caused by optical cross-talk between the laser and the MSP detector. The spectrum was integrated over a whole measurement run to obtain reasonable statistical errors (not shown).*

all fragments in the peak are originating from the collinear region of the elctron cooler (then the width should only be $\approx$50 ns), but also from some length before and after it. This broadening cannot be attributed to the time resolution of the system, because the width of the cross-talk shows that this is in fact better than 10 ns (the count numbers do not allow finer binning of the data). Both the existence and the width of the fragment peak show that there must be an unexpected interaction at work between the laser light and the ions themselves, instead of the DR fragments.

The only candidate process which could possibly produce an enlarged fragment rate in coincidence with the laser shots is photodissociation of HD^+. But because of poor Franck-Condon overlap, the cross section is very small for HD^+ in its ground state, which indicates that the peak actually arises from the photodissociation of *vibrationally excited* ions. Since these are known to decay within ≈400 ms, and the ions have been stored for more than 5 s before measuring, there had to be a mechanism for vibrational excitation of the stored ground state ions. An important clue is that (as will be shown further down) the ratio between the area below the peak and the DR background shows a clear dependence on the relative energy of the electron cooler beam. This strongly suggests that the stored ground-state ions are vibrationally excited in collisions with electrons.

In this case, the increase (per unit time) of the probability of an ion to be excited to a vibrational state v, by electrons of relative energy E, is given by the respective two-body rate coefficient for vibrationally inelastic collisions (IC):

$$\frac{dp_v}{dt} = \frac{L_{EC}}{L_{TSR}} \alpha_{IC,v}(E) n_e \tag{5.5}$$

with the number density of the electron beam n_e (which slightly depends on the measurement energy), and the relative velocity $v_{rel} = \sqrt{2E/m_e}$. The length ratio between the electron cooler and the TSR circumference ($L_{EC}/L_{TSR} = 0.0269$) has to be introduced to take into account that electrons are only present in the interaction region. Accordingly, the production rate of ions in the vibrational state v from a given number N_{ion} of ground state ions is

$$\dot{N}_v(E) = N_{ion}\frac{dp_v}{dt} = N_{ion}\frac{L_{EC}}{L_{TSR}} \alpha_{IC,v}(E) n_e \tag{5.6}$$

assuming that the number of ground state ions stays significantly higher than the one of excitd ions, and that further interaction of vibrationally excited ions with the electrons can be neglected. Introducing a mean lifetime τ_v for each vibrational state (with respect to decay or feeding by radiative cooling, and to ion depletion by photodissociation), the equilibrium number of ions in each vibrational state and at a relative energy E is approximately given by $N_v(E) = \dot{N}_v(E)\tau_v$. The fragment rate from vibrational excitation followed by photodissociation, integrated over all possible v, is then

$$\dot{N}(E) = \left(\frac{L_{EC}}{L_{TSR}}\right)^2 \left[\sum_v \alpha_{IC,v}(E)\tau_v\sigma_{PD,v}c\right] N_{ion}n_\gamma n_e = \left(\frac{L_{EC}}{L_{TSR}}\right)^2 \alpha_{IC+PD}(E) N_{ion} n_\gamma n_e \tag{5.7}$$

where the expression in brackets was replaced by the three-body rate coefficient $\alpha_{IC+PD}(E)$ (units cm^{6}s^{-1}) to allow for a simpler description of the combined reaction. In contrast to the DR/DE case, the length ratio L_{EC}/L_{TSR} enters into the rate equation twice, because also the laser beam overlaps with the ions only inside the electron cooler.

To obtain an energy spectrum of this rate coefficient, $\dot{N}(E)$ has to be determined from the experimental data. First, the counts (per laser shot) in the peak and the background are obtained by integration over the intervals of length τ_{sig} and τ_{bgr} shown in Fig. 5.4. These counts are summed up over all injections done at a particular measurement energy, which yields the total signal and background count numbers $N_{sig}^{meas}(E)$, $N_{bgr}^{meas}(E)$, so that the background subtracted photodissociation rate is given by $\dot{N}(E)=N_{sig}^{meas}(E)/\tau_{sig}-N_{bgr}^{meas}(E)/\tau_{bgr}$. The measurement energy is derived from the settings of the DAC controlling the offset to the cathode voltage, as described in Chapter 3.3. Because in some measurement runs the count numbers were still very small, the energy scale of the experiment was rebinned to intervals of a width of 20 DAC-settings, so that E now denotes the energy at the center of each bin.

The absolute rate coefficient for vibrational excitation followed by photodissociation is thus

$$\alpha_{IC+PD}(E) = \left(\frac{L_{TSR}}{L_{EC}}\right)^2 \frac{\frac{1}{\tau_{sig}} N_{sig}^{meas}(E) - \frac{1}{\tau_{bgr}} N_{bgr}^{meas}(E)}{N_{shots}(E) \left\langle N_{ion} \right\rangle_E \left\langle n_\gamma \right\rangle_E n_e(E)} \tag{5.8}$$

where N_{ion} is the number of HD$^+$ ions stored in the TSR at the time of a laser shot, n_γ the number density of photons in the shot and $N_{shots}(E)$ the number of laser shots done at each energy, while $\langle \quad \rangle_E$ indicates the averaging over all laser shots done in all injections with a particular measurement energy.

Because the absolute number of ions stored in the ring was not measured, it is derived from $N_{bgr}^{cool}(E)$, which is the number of fragments in the background window in electron cooling mode, *as a function of the measurement energy in the respective injections.* In electron cooling mode, the particles hitting the detector originate mainly from *DR* at $E=0$ eV, where $\alpha_{DR} \approx 2 \cdot 10^{-8}$ cm^{3}s^{-1}, so that (4.1) can be used with $n_e = 5.2 \cdot 10^7$ cm^{-3} to estimate the average number of ions stored in the TSR:

$$\left\langle N_{ion} \right\rangle_E = \frac{L_{TSR}}{L_{EC}} \cdot \frac{N_{bgr}^{cool}(E)}{\tau_{bgr} N_{shots}(E)} \cdot \left. \frac{1}{\alpha_{DR} n_e} \right|_{E=0} \tag{5.9}$$

with $\alpha_{DR} n_e \approx 1$ s^{-1} at $E=0$ eV.

As explained in more detail in Appendix B, problems were encountered with the measurement of the laser pulse energy using the photodiode, so that this data could not be used to normalize the runs. This required the introduction of an average photon density $\bar{n}_\gamma = 1.9 \cdot 10^{14}$ cm^{-3} derived from the average energy (3 mJ) and duration of the laser pulses, and a scaling factor k_i for each measurement run, which was applied to the data before merging all runs, yielding the measured rate coefficent

$$\alpha_{IC+PD}(E) = \frac{L_{TSR}}{L_{EC}} \cdot \frac{\left\langle k_i \left[\frac{\tau_{bgr}}{\tau_{sig}} N_{sig}^{meas}(E) - N_{bgr}^{meas}(E) \right] \right\rangle_i}{\left\langle N_{bgr}^{cool}(E) \right\rangle_i \bar{n}_\gamma n_e} \cdot \left. \alpha_{DR} n_e \right|_{E=0} \tag{5.10}$$

where $\langle \quad \rangle_i$ denotes the average over all measurement runs. This rate coefficient, which is shown as black dots in Fig. 5.5, still contains two types of background, which have to be eliminated:

First, there may be vibrational excitation of stored ions by collisions with residual gas molecules. At a given ion velocity, the fragment rate due to this process depends only on the number of stored ions and on the number density of residual gas molecules. Since pressure in the TSR remained almost constant at $\approx 10^{-10}$ mbar throughout the experiment, the fragment rate from this process is only proportional to the number of stored ions. However, because $\alpha_{IC+PD}(E)$ is normalized to the electron density $n_e(E)$, the same has to be applied to the contribution from residual gas collisions, leading to a background rate coefficient

$$\alpha_{bgr}^{res.gas}(E) = \frac{const.}{n_e(E)} \tag{5.11}$$

which can directly be subtracted from $\alpha_{IC+PD}(E)$ as soon as the constant is known.

In addition, the rate coefficient for excitation by electron scattering is convoluted with the energy shift in the bending regions, inside the toroid magnets of the electron cooler. In order to eliminate the toroid contribution by the algorithm described in Chapter 3.3 and [56], the background from residual gas collisions has to be already subtracted from the raw data; otherwise, the toroid background will be estimated too high. But because the strength of the residual gas background cannot be deduced independently from the experimental data, both backgrounds are determined simultaneously in a manual χ^2-fit procedure: For electron energies below 1.1 eV, only the vibrational states $v = 1-4$ can be excited, which show no significant photodissociation because of the small cross section (Fig. 2.5). In consequence, the measured rate coefficient below 1.1 eV is a superposition of both background effects only; the background subtracted rate coefficent must be consistent with zero within the statistical errors. Therefore the subtraction of the residual gas background is done for several values of the constant in (5.11); each time the toroid background is estimated in the usual way and subtracted. Then a χ^2 between the background subtracted rate coefficient and zero is calculated for $E \leq 1.1$ eV, and minimized as a function of the magnitude of the residual gas background, to obtain its value ($0.55 \cdot 10^{-20}$ cm^{6}s^{-1}). The resulting, background subtracted rate coefficient is shown as the red curve in Fig. 5.5, while the residual gas background is plotted in green and the toroid background in blue.

Finally, the dependence of the measured rate coefficient on the storage time was examined, to detect possible influences of the drag-force exerted by the electrons (described in Chapter 4.2). The measured data was divided into two sets depending on the time after injection: one set continuing the data from $5-10$ s, and the other from $10-15$ s. Both sets were then compared by calculating the ratio between the corresponding rate coefficients, but within the statistical erros no difference from unity was found, proving that the measured rate coefficient does not depend on storage time at least on a scale of seconds.

5.4 Measured Rate Coefficient

Figure 5.5 shows the measured rate coefficient for vibrational excitation followed by photodissociation (black dots, with statistical errors only), together with the background contributions from residual gas scattering (green) and energy shift in the toroid sections (blue). The overall scale of the y-axis is accurate to approximately one order of magnitude, due to the systematic errors from the determination of the stored ion current and the average photon density, which is not included in the error bars. The red curve shows the measured rate coefficient after subtraction of both backgrounds; systematic errors from the background estimation have been neglected, therefore error bars are identical to the ones plotted along the black curve.

As was discussed already in the last chapter, the vibrational states which are excited by electrons at low energy do not lead to a perceivable photodissociation signal. The onset of the photodissociation signal at 1.2 eV approximately coincides with the thresholds of 1.07 eV and 1.25 eV [47] for the production of the vibrational level $v=5$ or 6, which are the lowest vibrational levels of HD^+ with a significant photodissociation cross section (Fig. 2.5). At higher energies, the strong dependence of α_{IC+PD} on E shows that indeed the collisions between ions and free electrons are responsible for the majority of vibrationally excited HD^+ ions, while excitation by collisions with residual gas yields only a small contribution, which is important only at very small or very high electron energies and which (together with the toroidal background) actually caused the problems in observing the $2s/2p$ interference.

Above $v=6$, all vibrational states have similar radiative lifetimes ($10-15$ ms [71]). Since these are short compared to the storage time, many vibrational states with lower v will also be populated in the radiative decay process, even if only one specific state would be excited at a given electron energy. Hence, although $\sigma_{PD,v}$ depends on v (Fig. 2.5), the *mean* photodissociation cross section (averaged over all vibrational levels populated in the ion beam) varies only slowly with E, so that the features in $\alpha_{IC+PD}(E)$ are mostly due to the excitation step.

Because of the poor Franck-Condon overlap between initial and final wave function for direct excitation of vibrational states, the measured rate coefficient is attributed to the indirect IC mechanism presented in Chapter 2.2.2: In analogy to the DE case, the onset of α_{IC+PD} at low energies is explained by electron capture into the $(2p\sigma_u)^2$ state, with subsequent autoionization to a vibrationally excited HD^+ ion, while the maxima at 7 eV and 13 eV are attributed to indirect excitation involving states from the Q1 or Q2 manifold of HD, respectively.

$$\mathrm{HD}^+_{v=0} + e^- \longrightarrow \mathrm{HD}^* \longrightarrow \mathrm{HD}^+_{v'} + e^- \tag{5.12}$$

To obtain an estimation of the rate coefficient for the inelastic collision process alone, it is assumed that all states excited in the process have approximately the same average lifetime of

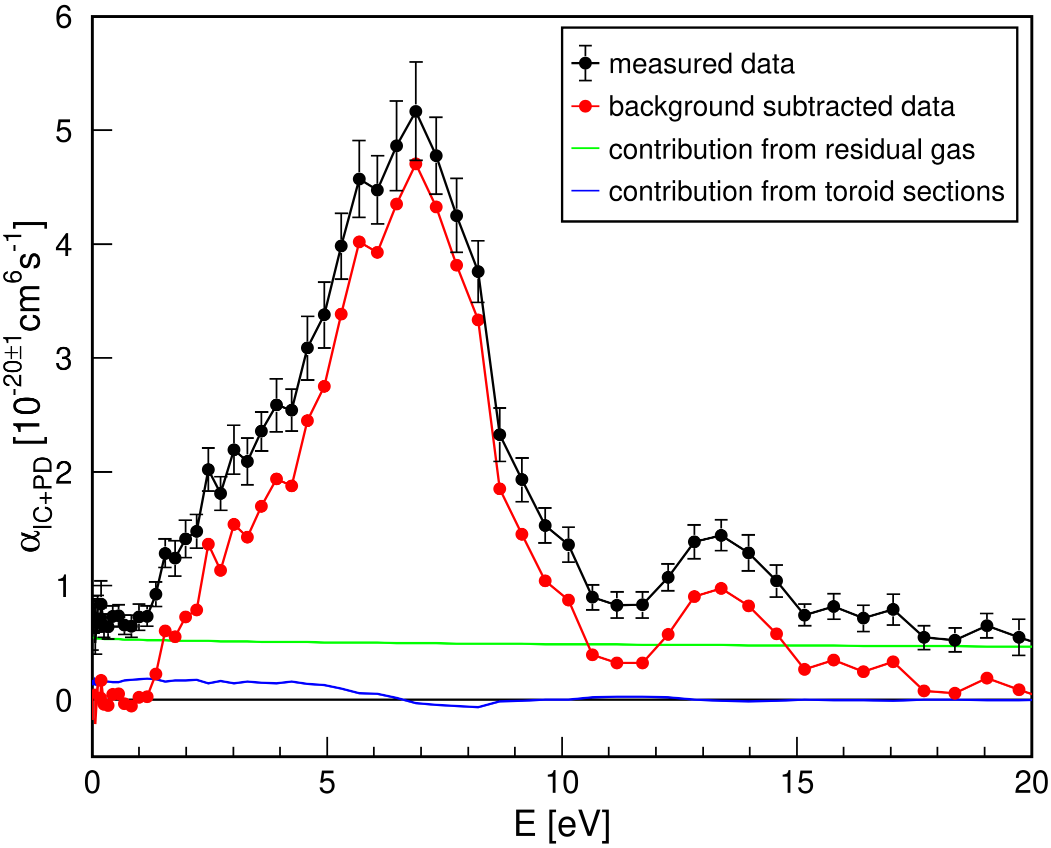

Fig. 5.5: *Measured three-body rate coefficient $\alpha_{IC+PD}(E)$ for vibrational excitation of HD$^+$ followed by photodissociation, together with the backgrounds from residual gas scattering and from energy shifts in the toroid sections.*

$\bar{\tau} = 50$ ms, which was measured for $v = 5, 6, 7$ in [51] and is different from the radiative lifetime because lower v levels are fed by the decay of higher ones. Also, the photodissociation cross section is averaged over all vibrational levels above $v = 4$ ($\bar{\sigma}_{PD} = 10^{-18}$cm^2), so that with (5.7), the rate coefficient $\alpha_{IC}(E)$ for vibrational excitation in inelastic collisions is

$$\alpha_{IC}(E) \approx \frac{\alpha_{IC+PD}(E)}{\bar{\tau} \cdot \bar{\sigma}_{PD} c} = \frac{\alpha_{IC+PD}(E)}{1.5 \cdot 10^{-9}\ \mathrm{cm}^3} \tag{5.13}$$

The resulting rate coefficient, which is still integrated over all available vibrational states with significant photodissociation probability, is shown in Fig. 5.6. No error bars are plotted because the statistical fluctuations are probably exceeded by the systematical errors inferred from the elimination of the photodissociation step in (5.13). These do not only cause a global error in the scale of α_{IC} (which is estimated to be ±1.5 orders of magnitude), but also affect its energy-dependence. Within these large errors, the order of magnitude of the deduced rate coefficient is still in agreement with a present calculation [72] of vibrational excitation of H_2^+ by slow

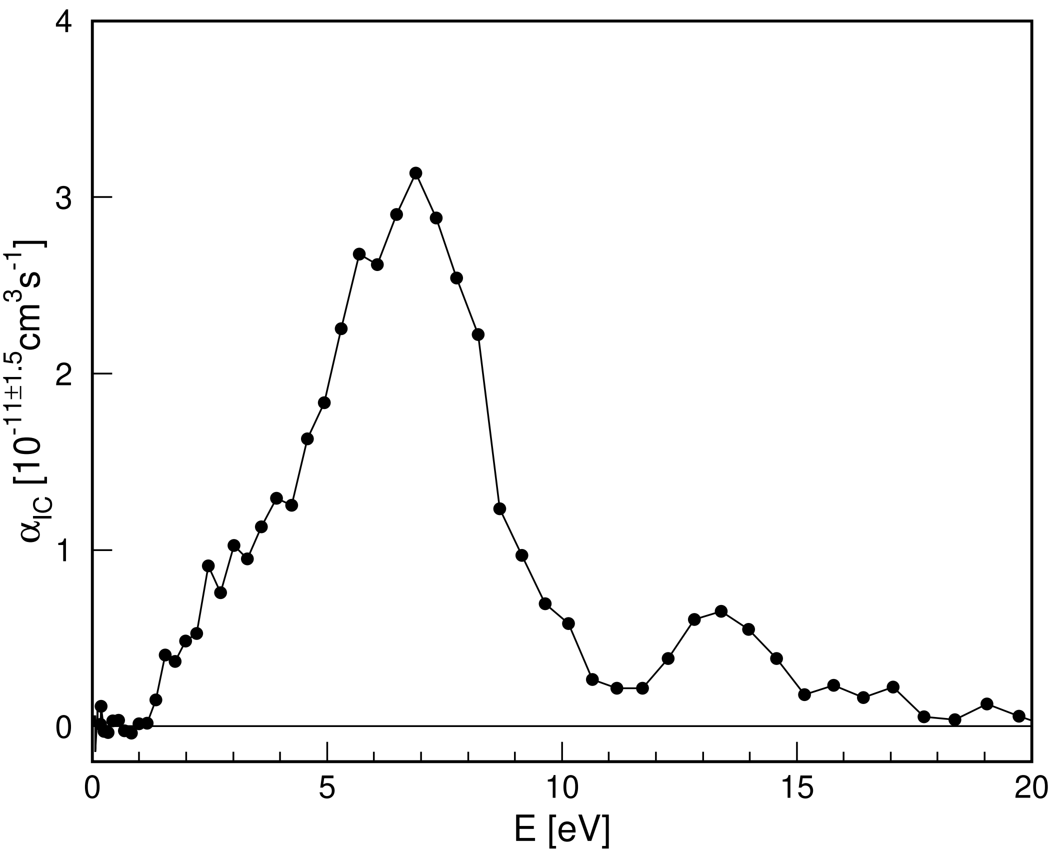

Fig. 5.6: *Estimated rate coefficient for the vibrational excitation step alone, integrated over all energetically open vibrational levels of* HD^+.

electrons ($8.7 \cdot 10^{-10}$ cm^{3}s^{-1}), although it considered excitations $v = 0 \rightarrow 2$ by electrons with a thermal velocity distributions corresponding to 10^4 K.

Because the electron capture step in this mechanism is the same as in dissociative recombination or excitation, the autoionization into vibrationally excited ions acts an additional loss channel to both reactions. This has not been taken into account in theory up to now, but may be of importance e.g. to the total DR cross section if the probability for dissociation is already small because of strong autoionization into the ionic continuum. It must be noted, however, that the absolute rate coeficient for IC is smaller than the one for DR or DE by two orders of magnitude. This is fortunate, from an experimental point of view, because the small values of α_{IC} mean that the relative number of vibrationally excited ions in the beam is still at most 10^{-4}, even at the maximum of α_{IC}. Thus, contributions from higher vibrational levels in a supposed measurement of the ground state DR rate coeffficient (such as in Chapter 4.2) are not expected even from $v = 6$, which is known to have a DR rate coefficient exceeding that of the ground state by a factor of 100 at $E = 0$ [51].

6. Conclusions and Outlook

Within this work, two experiments have been presented which were carried out at the TSR storage ring at the Max-Planck-Institut für Kernphysik in Heidelberg. Both experiments examined the interaction of free electrons with stored HD^+ molecular ions in their vibrational ground state, focusing on the competition between various reactions involving charge-transfer reactions to the $(2p\sigma_u)^2$ state of neutral HD. The most important results from these measurements are summarized in the following list:

- The rate coefficient of dissociative recombination of ion and electron into neutral atomic fragments was measured on an absolute scale, with a high resolution of electron energy, and with high statistics. A special calibration scheme was used to monitor the stored ion current during the measurement, which cannot be measured directly at the same time as the fragment rates from DR. The results were compared to a recent MQDT calculation, which took into account the contribution from both the direct and the indirect DR mechanism to the rate coefficient, with good agreement below 1 eV and at high electron energies, but significant difference at $1-4$ eV.

- In a second measurement of this type, the parameters of the electron beam, namely its adiabatic expansion factor, were optimized for the first dedicated measurement in the almost uninvestigated mimimum of the DR rate coefficient, at electron energies of $1-4$ eV. This method improved the DR rate by roughly one order of magnitude, and strongly suppressed the background from energy shift in the bending regions of the electron beam, at only a small expense of energy resolution. It was possible thereby to observe previously unknown step structures in the DR rate coefficient of HD^+, which occured in coincidence with the opening of additional dissociation channels with increasing electron energy. These steps were explained by an enlarged autoionization probability of the intermediate neutral molecule, because of the reflection of probability flux by energetically forbidden dissociation channels.

- The other experiment aimed at the observation of interference patterns in the relative population of the DR fragment states with $2s$ and $2p$ electronic configuration. Although this goal could not be achieved, it was possible to detect vibrational excitation of the stored molecular ions by collisions using the photodissociation with a UV laser beam as a sensitive probe. The results showed contributions from two different sources for vibrational excitation, either by electrons from the TSR electron cooler or in collisions with residual gas. This was the first time that any mechanism counteracting the radiative cooling of infrared active ions in a storage ring has been observed, although there have been dedicated experiments [73].

- Using an estimation of the average radiative lifetime of the excited states and an average photodissociation cross section, an approximate rate coefficient for the vibrational excitation of HD^+ in collisions with electrons was obtained.

In both experiments, the competition between several possible reaction channels *after* the capturing of the electron has been of special importance. For example, in the DR at intermediate energies, it is the competition between dissociation into neutral fragments and autoionization into one neutral and one charged fragment, which leads to the observed steps in the rate coefficient. Because of the low DR rate coefficient, also the autoionization into vibrationally excited ions may be of importance in this region. Although, up to now, no theory is available which includes DR, DE, SEC and IC in a unified way, it is strongly suggested by the presented measurements that the interaction of molecular ions with electrons be treated within a network

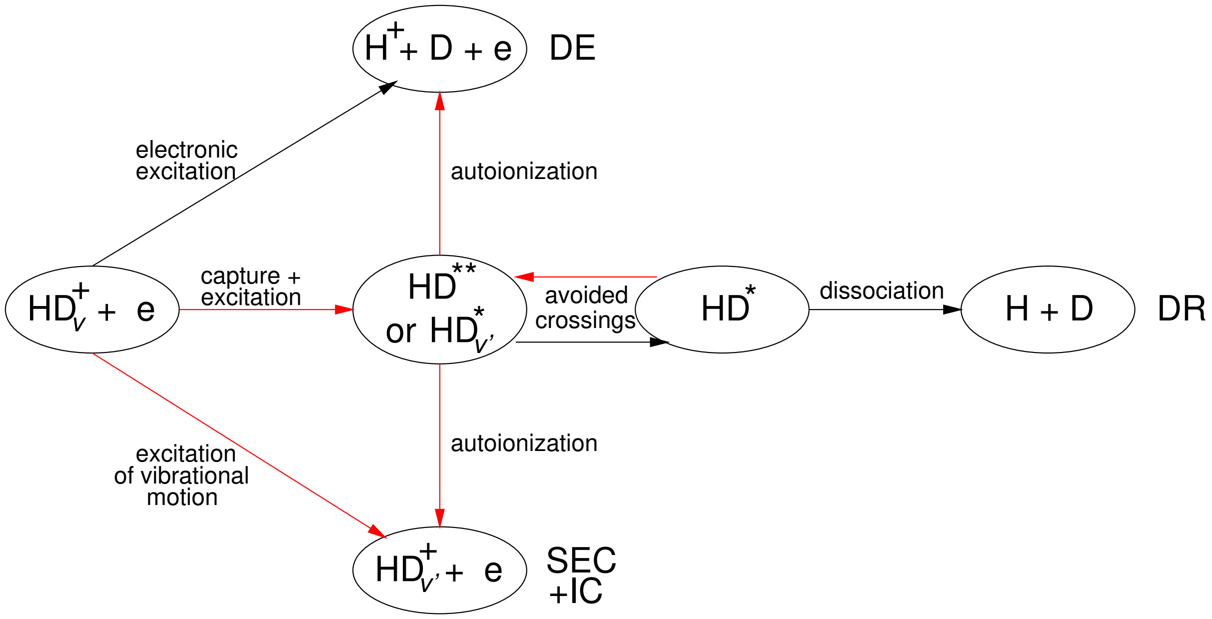

Fig. 6.1: *Network of competing mechanisms in the reactive scattering of electrons by molecular ions. The red lines mark reaction paths which have been of special importance to this work.*

of reactions like in Fig. 6.1, instead of looking only at one reaction at a time. Especially the theory of branching ratios in DR as well as in DE demands a more precise theoretical investigation. Similarly, this is needed for the SEC/IC process, but is much more difficult because vibrational-state selective measurements yet remain to be done.

Also the DR into charged fragments ($H^+ + D^-$ or $H^- + D^+$) still needs investigation. Experimentally, this channel can only be observed by also detecting the charged particles originating from the electron cooler. This is one of the reasons why there is a new detector setup under construction at the MPI, where movable detectors are planned especially for detecting charged H or D fragments already inside the field of the TSR dipole magnet. The detector will be working in conjunction with a dedicated electron target, so that the existing electron cooler can be kept in cooling mode throughout the whole measurement. This not only provides a constant profile and velocity distribution of the ion beam during experiments, but also gains time for data acquisition, by allowing to omit the electron cooling step in the wobbling scheme. Moreover, it will also be possible to install a detector system for three-dimensional imaging of DR fragments, which presently is complicated by the smallness of the available space in and behind the detector chamber.

But also the existing detectors still provide excellent opportunities for further experiments. For example, the measurement of the $2s/2p$ interference might still be possible, despite the background vibrational excitation: At low energies, only the vibrational levels $v = 1 - 4$ can be excited in collisions with electrons, which have an almost vanishing cross section for photodissociation. Higher vibrational states can only be accessed in collisions of ions with residual gas, but since this reaction contributes a very smooth background, the $2s/2p$ population ratio might still be measured on top of it with the proposed setup, if enough events are accumulated in coincidence with the laser.

Finally, the measurement of cross sections and branching ratios of ions other than HD^+ will also yield interesting results. Especially the combination with the technique of foil-induced coulomb explosion imaging (CEI) [74], which allows to determine the vibrational population of the stored beam as a function of storage time, by measuring the nuclear wave function of the ions, has proven to be very fruitful [51].

Appendix

A Pileup Correction in the DR and DE Measurements

In chapter 4.3 it was discovered that the amplitude histogram of the signals from the solid-state detector contained a background, from random coincidences of fragment atoms produced in uncorrelated DR or DE events ("pileup"). For the H+D peak, a pileup event occurs whenever an H and a D fragment from dissociative excitation arrive at the detector with a time difference smaller than τ_{coin}, the effective coincidence window of the detector-amplifier-ADC chain. For a sufficiently short coincidence window, and neglecting coincidences between three or more particles, the pileup rate is given by

$$R_{H+D,pileup} = 2\tau_{coin} R_H R_D \tag{A.1}$$

where the factor of 2 reflects the sum over the two possible orders in which the particles can arrive at the detector (H or D leading). Since R_H and R_D are almost equal, the H+D pileup is estimated by

$$R_{H+D,pileup} = 2\tau_{coin} \left(R_D\right)^2 \tag{A.2}$$

The subtraction of this pileup is of particular importance for the measurement of the DR rate coefficient at energies above 10 eV, where $R_D \gg R_{H+D}$. Therefore, the coincidence window is determined from the data taken at reference energy[1]: Without pileup, the measured rates R^{ref}_{H+D} and R^{ref}_D would both be proportional to the stored ion current, or

$$R^{ref}_{H+D} = const. \cdot R^{ref}_D \tag{A.3}$$

However, at reference energy the ratio α_{DR}/α_{DE} is very small, so that pileup becomes prominent and the relation between R_D and R_{H+D} is a superposition of the above equation and (A.2). Thus, τ_{coin} is determined from a fit of

$$R_{H+D} = 2\tau_{coin} \left(R_D\right)^2 + const. \cdot R_D \tag{A.4}$$

---

[1] The first few hours of measurement with the narrow electron beam still employed a reference energy in the wobbling scheme, which was later replaced by a second cooling step

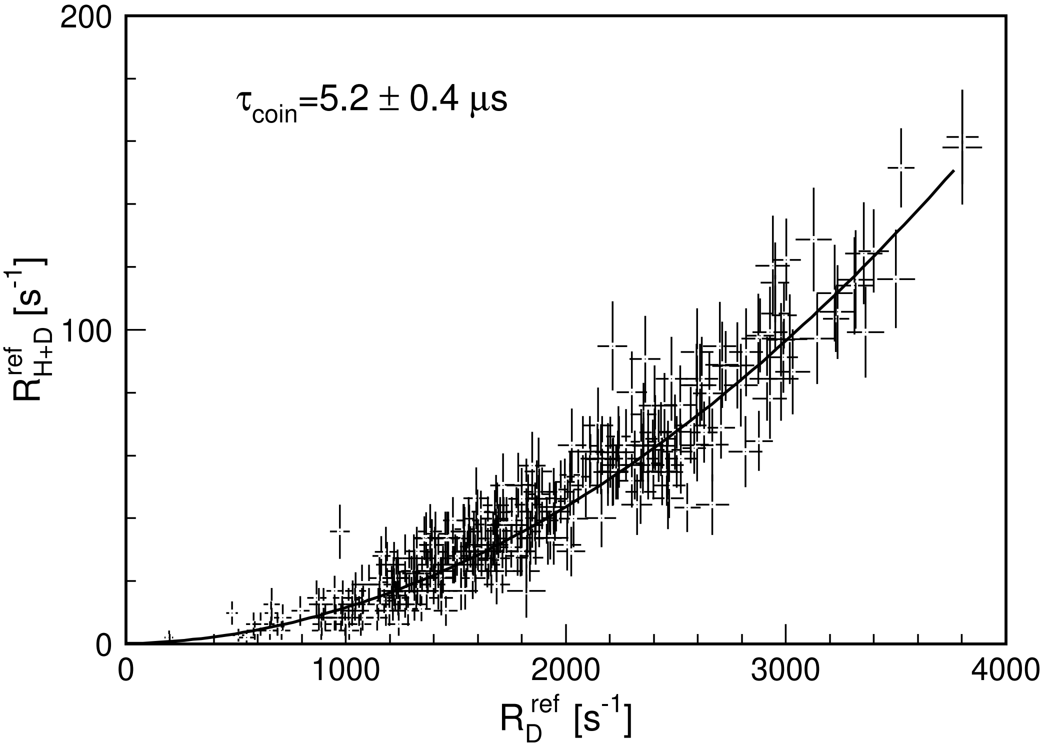

Fig. A.1: *Example fit of the coincidence time window.*

to the particle rates measured directly after the precooling phase. As an example, this procedure is shown for one measurement run in Figure A.1. After averaging over many measurement runs the following values are obtained, which are different for the two measurements of α_{DR} because different time constants were used for the signal shaping in the amplifiers:

$$\tau_{coin} = \begin{cases} 2.3 \pm 0.5\ \mu\text{s} & \text{with the wide electron beam} \\ 5.0 \pm 0.5\ \mu\text{s} & \text{with the narrow electron beam} \end{cases} \tag{A.5}$$

At all energies, the contribution of pileup to R_{H+D} is estimated with (A.2) and subtacted before further processing of the measured data.

B Matching of Measured Rate Coefficients for Inelastic Collisions

The failure of the measurement of the laser pulse energy with the photodiode was adressed only briefly in chapter 5.3 and remained open for a more detailed discussion:

The readout of the diode was found to depend on the laser beam profile, which changes slightly with increasing age of the dye solution. This was confirmed in a separate measurement, where the ratio of the diode readout to a powermeter changed by a factor of 2 after replacing the used dye solution with a fresh one. Thus, the photon density could not be measured for each laser pulse. But since the dye lifetime of $\approx$48 hours was very long compared to the typical duration of $1-3$ hours for a run, the photon density $\langle n_\gamma \rangle_E$ (averaged over the several thousand shots done at each electron energy) is constant over each run, and certainly has no correlation with E. Therefore, data from all measurement runs were evaluated independently, and the resulting rate coefficient spectra were scaled by a dimensionless factor k_i to match the spectrum of a reference run (run 78, being the one with largest statistical sample). The results listed in table B.1 therefore reflect both the varying laser power and possible changes in the overlap with the stored ion beam.

For obtaining the absolute rate coefficient, an average photon density of $\bar{n}_\gamma = 1.9 \cdot 10^{14}$ cm^{-3} was roughly estimated from the pulse energy of 3 mJ inside the TSR, the pulse length of 10 ns and the laser beam cross section of 0.1 cm^2.

run number i	25	26	27	28	29	30	31	65	66	78
scaling factor k_i	0.49	0.53	0.50	0.49	0.56	0.48	0.48	0.64	0.98	1.00

Tab. B.1: *Scaling factors for all measurement runs, obtained by matching to the reference run (78). Gaps in the numbering of runs reflect breaks in the data taking, for optimization of ion sources, accelerators, beam overlap or electronics.*

References

[1] E. Roueff, J. Le Bourlot and G. Pineau des Forets, in *Dissociative Recombination: Theory, Experiment and Applications III*, ed. D. Zajfman, J. B. A. Mitchell, D. Schwalm and B. R. Rowe, World Scientific, Singapore 1996, p. 11.

[2] J. E. Dyson and D. A. Williams, *The Physics of the Interstellar Medium 2nd ed.*, Institute of Physics Publishing, London 1997.

[3] M. Lange, J. Levin, G. Gwinner, U. Hechtfischer, L. Knoll, D. Schwalm, R. Wester, A. Wolf, X. Urbain and D. Zajfman, Phys. Rev. Lett. **83**, 4979 (1999).

[4] M. Lange, J. Levin, L. Knoll, H. Kreckel, M. Scheffel, D. Schwalm, X. Urbain, R. Wester, A. Wolf and D. Zajfman, in *Dissociative Recombination: Theory, Experiment and Applications IV*, ed. M. Larsson, J. B. A. Mitchell and I. F. Schneider, World Scientific, Singapore 2000, p. 265.

[5] T. Tanabe, H. Takagi, I. Katayama, K. Chida, T. Watanabe, Y. Arakaki, Y. Haruyama, M. Saito, I. Nomura, T. Honma, K. Noda, and K. Hosono, Phys. Rev. Lett. **83**, 2136 (1999).

[6] M. Saito, Y. Haruyama, T. Tanabe, I. Katayama, K. Chida, T. Watanabe, Y. Arakaki, I. Nomura and T. Honma, Phys. Rev. A **61**, 062707 (2000).

[7] S. Krohn, Z. Amitay, A. Baer, D. Zajfman, M. Lange, L. Knoll, J. Levin, D. Schwalm, R. Wester and A. Wolf, Phys. Rev. A **62**, 032713 (2000).

[8] M. Born and J. R. Oppenheimer, Ann. Phys. **84**, 457 (1927).

[9] H. Lefebvre-Brion and R. W. Field, *Perturbations in the Spectra of Diatomic Molecules*, Academic Press, Orlando 1986, p. 28 ff.

[10] B. H. Bransden and C. J. Joachain, *Physics of Atoms and Molecules*, Addison Wesley Longman, Essex 1983.

[11] L. D. Landau, Phys. Z. Sowjetunion **2**, 46 (1932).

[12] C. Zener, Proc. R. Soc. London Ser. A **B7**, 696 (1932).

[13] E. C. G. Stueckelberg, Helv. Phys. Acta **5**, 369 (1932).

[14] C. Zhu and H. Nakamura, J. Chem. Phys. **106**, 2599 (1997).

[15] C. Zhu and H. Nakamura, J. Chem. Phys. **107**, 7839 (1997).

[16] C. Zhu and H. Nakamura, J. Chem. Phys. **101**, 10630 (1994).

[17] C. Zhu and H. Nakamura, J. Chem. Phys. **102**, 7448 (1995).

[18] B. D. Esry and H. R. Sadeghpour, Phys. Rev. A **60**, 3604 (1999).

[19] M. Madsen and J. M. Peek, Atomic Data **2**, 171 (1971).

[20] L. Wolniewicz and K. Dressler, J. Chem. Phys. **82**, 3292 (1985).

[21] S. L. Guberman, J. Chem. Phys. **78**, 1404 (1983).

[22] D. Zajfman, Z. Amitay, M. Lange, U. Hechtfischer, L. Knoll, D. Schwalm, R. Wester A. Wolf and X. Urbain, Phys. Rev. Lett. **79**, 1829 (1997).

[23] P. Forck, PhD Thesis, Max Planck-Institut für Kernphysik, MPI H-V 29-1994, Heidelberg 1994.

[24] J. M. Peek, Phys. Rev. A **10**, 539 (1974).

[25] D. Zajfman and Z. Amitay, in *Proceedings of the 1995 Workshop on Dissociative Recombination: Theory, Experiment and Applications III*, ed. D. Zajfman, J. B. A. Mitchell, D. Schwalm, B. R. Rowe, World Scientific, Singapore 1996, p. 114.

[26] L. H. Andersen, P. J. Johnson, D. Kella, H. B. Pedersen and L. Vejby-Christensen, Phys. Rev. A **55**, 2799 (1997).

[27] K. P. Huber and G. Herzberg, *Molecular Spectra and Molecular Structure, IV. Constants of Diatomic Molecules*, Van Nostrand Reinhold, New York 1979.

[28] J. N. Bardsley, J. Phys. B (Proc. Phys. Soc.) **1**, 349 (1968).

[29] J. N. Bardsley, J. Phys. B (Proc. Phys. Soc.) **1**, 365 (1968).

[30] J. N. Bardsley and M. A. Biondi, Adv. At. Mol. Phys. **6**, 57 (1970).

[31] H. Takagi, in *Proceedings of the 1995 Workshop on Dissociative Recombination: Theory, Experiment and Application III*, ed. D. Zajfman, J. B. A. Mitchell, D. Schwalm, B. R. Rowe, World Scientific, Singapore 1996, p. 174.

[32] J. M. Peek, Phys. Rev. **154**, 52 (1967).

[33] J. M. Peek and Th. A. Green, Phys. Rev. **183**, 202 (1969).

[34] I. Borges, G. Jalbert and C. E. Bielschowsky, Phys. Rev. A **57**, 1025 (1998).

[35] B. K. Sarpal and J. Tennyson, Mon. Not. R. Astron. Soc. **263**, 909 (1993).

[36] S. L. Guberman, AIP Conference Proceedings **347**, 88 (1995).

[37] T. Tanabe, I. Katayama, S. Ono, K. Chida, T. Watanabe, Y. Arakaki, Y. Haruyama, M. Saito, T. Odagiri, K. Hosono, K. Noda, T. Honma and H. Takagi, J. Phys. B: Atomic Molecular & Optical Physics **31**, L297 (1998).

[38] S. Krohn, M. Lange, L. Knoll, H. Kreckel, J. Levin, D. Schwalm, R. Wester, P. Witte, A. Wolf and D. Zajfman, accepted for publication by Phys. Rev. Lett.

[39] D. R. Bates, Phys. Rev. **78**, 492 (1950).

[40] A. Giusti-Suzor, I. F. Schneider and O. Dulieu, in *Dissociative Recombination: Theory, Experiment and Applications*, ed. B. R. Rowe, J. B. A. Mitchell and A. Canosa, Plenum Press, New York 1993, p. 11.

[41] Z. Amitay and D. Zajfman, Rev. Sci. Instrum. **68**, 1387 (1997).

[42] X. Urbain, private communication.

[43] J. S. Cohen, Phys. Rev. A **13**, 99 (1976).

[44] D. Zajfman, private communication.

[45] H. Takagi, J. Phys. B: Atomic Molecular & Optical Physics **26**, 4815 (1993).

[46] J. Tellinghuisen in *Advances in Chemical Physics, LX. Photodissociation and Photoionization*, ed. K. P. Lawley, John Wiley & Sons, Chichester 1985.

[47] R. J. Le Roy, LEVEL 7.0, *A Computer Program Solving the Radial Schrödinger Equation for Bound and Quasibound Levels*, Chemical Physics Research Report CP-642, University of Waterloo, Canada 2000.

[48] M. Madert, PhD-thesis, MPI für Kernphysik, Heidelberg 1998.

[49] M. Madert, R. Cee, M. Grieser, R. von Hahn, S. Papureanu, H. Podlech, R. Repnow, D. Schwalm, Nucl. Instrum. Methods B **139**, 437 (1998).

[50] R. von Hahn, R. Cee, M. Grieser, V. Koessler, M. Madert, S. Papureanu, H. Podlech, R. Repnow, D. Schwalm, C.-M. Kleffner, D. Habs, A. Schemp, *The High Current Injector at the MPI für Kernphysik in Heidelberg*, Proc. EPAC 98, Stockholm.

[51] Z. Amitay, A. Baer, M. Dahan, L. Knoll, M. Lange, J. Levin, I. F. Schneider, D. Schwalm, A. Suzor-Weiner, Z. Vager, R. Wester, A. Wolf, D. Zajfman, Science **281**, 75 (1998).

[52] G. Barking, Diploma thesis, MPI H-V41-1996, Max-Planck-Institut für Kernphysik, Heidelberg 1996.

[53] M. Schmitt, Diploma thesis, MPI H-V13-1996, Max-Planck-Institut für Kernphysik, Heidelberg 1996.

[54] S. Pastuszka, U. Schramm, M. Grieser, C. Broude, R. Grimm, D. Habs, J. Kenntner, H. J. Miesner, T. Schuessler, D. Schwalm and A. Wolf, Nucl. Instrum. Methods A **369**, 11 (1996).

[55] U. Hechtfischer, PhD-thesis, MPI H-V5-2000, MPI für Kernphysik, Heidelberg 2000.

[56] A. Lampert, A. Wolf, D. Habs, J. Kenntner, G. Kilgus, D. Schwalm, M. S. Pindzola, N. R. Badnell, Phys. Rev. A **53**, 1413 (1996).

[57] FORTRAN77 program *entfalt.f*, J. Kenntner and A. Wolf, private communicaton.

[58] J. Kenntner, PhD-thesis, MPI für Kernphysik and Universität Heidelberg 1995.

[59] J. Linkemann, PhD-thesis, Universität Stuttgart 1995.

[60] M. Jung, Diploma thesis, MPI H-1989-V34, Max-Planck-Institut für Kernphysik, Heidelberg 1989.

[61] M. Lange, *The CyrilNG manual*, MPI für Kernphysik, Heidelberg 2000.
URL: http://www.mpi-hd.mpg.de/ato/homes/mlange/sci/cyril/

[62] U. Eisenbarth, *User's guide to cyrildesktop*, MPI für Kernphysik, Heidelberg 2000.
URL: http://www.mpi-hd.mpg.de/ato/homes/eisenb/cyrildoc/cyrildesktop.html

[63] FORTRAN77 program *sigfold.f*, A. Wolf, private communication.

[64] I. F. Schneider, C. Strömholm, L. Carata, X. Urbain, M. Larsson and A. Suzor-Weiner, J. Phys. B: Atomic Molecular & Optical Physics **30**, 2687 (1997).

[65] T. Tanabe, I. Katayama, H. Kamegaya, K. Chida, Y. Arakaki, T. Watanabe, M. Yoshizawa, M. Saito, Y. Haruyama, K. Hosono, K. Hatanaka, T. Honma, K. Noda, S. Ohtani, and H. Takagi, Phys. Rev. Lett. **75**, 1066 (1995).

[66] W. Zong, G. H. Dunn, N. Djuric, M. Larsson, C. H. Greene, A. Al-Khalili, A. Neau, A. M. Derkatch, L. Vikor, W. Shi, A. Le Padellec, S. Rosen, H. Danared, M. af Ugglas, Phys. Rev. Lett. **83**, 951 (1999).

[67] Bergmann-Schaefer, *Lehrbuch der Experimentalphysik, Band 4: Teilchen*, pp. 83 and 242, de Gruyter, Berlin 1992.

[68] Bethe-Salpeter, *Quantum Mechanics of one- and two-Electron Atoms*, Plenum Press 1957.

[69] J. F. Ziegler and J. P. Biersack, *The Stopping and Range of Ions in Solids*, Pergamon Press, New York 1985.

[70] Ulrich Brackmann, *Lambdachrome Laser Dyes*, 3rd edition, Lambda Physik AG, Göttingen 2000.

[71] Z. Amitay, D. Zajfman and P. Forck, Phys. Rev. A **50**, 2304 (1994).

[72] B. K. Sarpal and J. Tennyson, Mon. Not. R. Astron. Soc. **263**, 909-912 (1993).

[73] U. Hechtfischer, Z. Amitay, P. Forck, M. Lange, J. Linkemann, M. Schmitt, D. Schwalm, R. Wester, D. Zajfman and A. Wolf, Phys. Rev. Lett. **80**, 2809 (1998).

[74] R. Wester, F. Albrecht, M. Grieser, L. Knoll, R. Repnow, D. Schwalm, A. Wolf, A. Baer, J. Levin, Z. Vager and D. Zajfman, Nucl. Instrum. Methods A **413**, 379 (1998).

Acknowledgements

Finally, i would like to express my thanks to all the people who have contributed to this work:

I thank Andreas Wolf for giving me the the opportunity to carry out this work in his atomic and molecular physics group, as well as for his continuing interest in the progression and results of the experiments. His sharing of experience on electron cooling and recombination was vital to designing and interpreting new measurements. I also wish to thank Frank Arnold for being my second referee.

Another person to thank is Daniel Zajfman, who always inspired me with new ideas. Dirk Schwalm has also shown continuous interest in my works, for which i want to thank him. Then there is Xavier Urbain, whose expertise and calculations on avoided crossings and other molecular transitions have been very important.

Of course, a huge thanks goes to my colleagues from the atomic and molecular physics group of both the MPI and the Weizmann Institute, who have not only helped me in carrying out the experiments, but have also made all this a great time. In particular, this refers to Roland Wester and Lars Knoll, whom i have been working with at the beginning of my time at the MPI, but also Holger Kreckel, Zohar Amitay, Gerald Gwinner, Sven Krohn, Jacob Levin, Lutz Lammich, Ulrich Hechtfischer, Guido Saathoff and Daniel Strasser have given me a lot of support.

Further thanks are adressed to Manfred Grieser, Kurt Horn and Robert von Hahn; without their support and advice concerning the TSR and the accelerators, this work would not have been possible. In this context, i also wish to thank the technicians under the lead of Roland Repnow for the operation of the accelerators. Also, i thank Udo Eisenbarth, Frank Köck and Thomas Kihm for their help on programming the new TSR data acquisition system.

Finally, i wish to thank all my friends and family, especially my girl-friend Sandra Hoppe, who always had great interest in my work and has helped me a lot with her continuing care and understanding.

Publishing Notes

In the time since submission of this work to the University of Heidelberg, some minor spelling and syntax errors have been found and corrected in the text. In addition, at a few occasions where misunderstandings were possible, the text was rearranged. No alterations or omissions have been applied to graphs and plots, nor to the scientific contents of this work.